

In-operando hard X-ray photoelectron
spectroscopy study on the resistive switching
physics of HfO₂-based RRAM

Von der Fakultät für Mathematik, Naturwissenschaften und Informatik der
Brandenburgischen Technischen Universität Cottbus

zur Erlangung des akademischen Grades

Doktors der Naturwissenschaften
(Dr. rer. nat.)

genehmigte Dissertation

vorgelegt von

Master of Science Engineer

Małgorzata Sowińska

geboren am 02. Juni 1986 in Gostyń (Polen)

Gutachter: Prof. Dr. Thomas Schröder

Gutachter: Dr. Sc. Karol Fröhlich

Gutachter: Prof. Dr. Lambert Alff

Tag der mündlichen Prüfung: 20. Mai 2014

To my Grandparents

Moim Dziadkom

Maria & Marian Pernak

Zofia & †Jan Sowińscy

ACKNOWLEDGEMENTS

After the time of intense work, the moment has come to finalize this chapter of life. Moreover, it is the time to recognize the support from many people I have received.

At the beginning, I would like to sincerely thank my supervisor Prof. Dr. Thomas Schröder for the opportunity to undertake research in the RRAM group at IHP. For his valuable time, support and for sharing with me his experience and knowledge I sincerely thank him.

I would like to thank my tutor Dr. Thomas Bertaud for supervising me during writing this PhD Thesis, his valuable comments and suggestions.

Then, I would like to thank Dipl.-Ing. (FH) Damian Walczyk and Dr. Christian Walczyk for fruitful scientific discussions, their support and the assistance in the realization of the *in-operando* HAXPES setup.

I would like to acknowledge the Deutsche Forschungsgemeinschaft (DFG) under project number SCHR1123/7-1 for financial support.

My deepest gratitude goes to Dr. Dawid Kot, Dr. Pauline Calka, Heike Silz, Frank Popiela, Dr. Ioan Costina, Dr. Mindaugas Lukosius, Dr. Grzegorz Łupina, Mohamed Elkhoully and Denys Martynenko for the help during preparation of the *in-operando* HAXPES samples and setup, and to Dr. Sebastian Thiess, Dr. Andrei Gloskovskii, Heiko Schulz-Ritter and Frank Okrent from DESY for the help offered during beamtimes at P09 in Hamburg.

I am also very indebted to Dr. Markus Andreas Schubert for STEM - EDX measurements; Dr. Peter Zaumseil and Dr. Lidia Łupina (Tarnawska) for the XRD and XRR results; Dr. Ioan Costina for ToF-SIMS measurements; Dr. Jordi

Sune and Dr. Xavier Cartoixa for first-principle calculations; Dr. Jarosław Dąbowski for the simulation of the Ti on HfO₂ growth model; and to Hans-Jürgen Thieme and Dr. Marvin Zöllner for the assistance and support during the experiments carried out at the MBE laboratory.

I would like to thank Kamil Kędzierski, Dr. Maciej Bazarnik and Dr. Slavo Nemšák for the scientific support.

Many thanks also to Dr. Adam Szyszka, Dr. Wojciech Koczorowski, Dr. Christian Reich, Tomasz Grzela, Dr. Oliver Skibitzki, Dr. Gunther Lippert, Dr. Christian Wenger, Dr. Canan Baristiran Kaynak, Udo Kaletta, Dr. Olaf Seifert, Dr. Gang Niu, Karol Furman and Yvonne Heier for their personal and scientific support, friendly atmosphere, and for being always open to listen and to help.

Especially thanks to Maria, Marcin, Kinga and Natalia Brzozowscy for creating a family atmosphere away from home; Many thanks to Katarzyna and Krzysztof Siut, Tatiana and Raiko Pevgonen, Lidia, Philipp and Tadeusz Zessin-Jurek, Lidia and Grzegorz Łupina, Justyna and Dawid Kot, Grzegorz Kozłowski, Adam Szyszka, Damian and Christian Walczyk and Ursula Pischel for making that time also fruitful in social events.

W tym miejscu pragnę także szczerze podziękować mojej Rodzinie, a w szczególności Moim Drogim Dziadkom, Rodzicom oraz Bratu, którzy byli dla mnie wsparciem w tym ważnym, a zarazem trudnym dla mnie czasie.

Dziękuję również Patrykowi za to, że zawsze trwał przy mnie w tych lepszych i w tych gorszych chwilach, oraz że wierzył we mnie, kiedy ja przestawałam już wierzyć i motywował mnie do dalszej walki, kiedy już brakowało mi sił.

ABSTRACT

Current memory technologies, such as DRAM, SRAM, and NAND Flash, which are approaching very difficult issues related to the continuous scaling to and beyond the 16 nm generation, has led research over the past two decades to the discovery of several new memory technologies. In recent years, new emerging nonvolatile memories (NVMs), such as phase-change random access memory (PCRAM), ferroelectric random access memory (FRAM), magnetic random access memory (MRAM), and resistive random access memory (RRAM), have been intensively studied. Among these candidates, RRAM is a very promising and worldwide studied candidate for alternative NVM and a high potential successor for Flash in terms of energy consumption (write current in the μA range compared to mA) and simplicity of process integration.

A fully CMOS compatible TiN/Ti/HfO₂/TiN RRAM module was successfully integrated with a select transistor (1T1R memory) in IHP's technology. Nonetheless, reliability and insufficient understanding of the resistive switching mechanism are the two main issues limiting this memory technology development for e.g. wireless sensor network (WSN) applications. The still unclear atomic-scale mechanism of HfO₂-based resistive switches and the identification of the material changes within the insulator must be addressed to suggest a knowledge-based improvement of device performance. In this frame, the Ti/HfO₂ interface is thoroughly investigated in this Thesis by complementary materials science techniques.

First, the investigation of the as-deposited Ti/HfO₂/TiN cells revealed that: (1) the Ti layer scavenges oxygen atoms stronger from amorphous (a-HfO₂) than from monoclinic (m-HfO₂) HfO₂ films; (2) not only oxygen vacancies but also other impurities in the atomic vapor deposited (AVD) a-HfO₂ film, such like nitrogen

and carbon (probably resulting from the used AVD precursor chemistry) are present in the HfO₂ insulator.

Next, the electrical characterization of Ti/AVD a-HfO₂/TiN cells (with voltage applied to the Ti top electrode while TiN bottom electrode was grounded) revealed a clockwise bipolar resistive switching behavior after an electroforming process at positive voltage polarity. Besides, the chemical and electronic changes observed by hard X-ray photoelectron spectroscopy (HAXPES), indicate the creation of *n*-type dopants in the a-HfO₂ film during the electroforming process, probably related to the formation of positively charged oxygen vacancies in a-HfO₂ by the electrochemically induced Ti/a-HfO₂ interface oxidation.

In order to directly compare electrical with electronic and chemical changes of one and the same RRAM cell, an *in-operando* HAXPES technique was developed. These unique studies have revealed the following characteristics of the Ti/AVD a-HfO₂/TiN cells: (1) the as-deposited cells are able to switch at low electrical power; (2) However, this resistive switching is not stable and an electroforming process with a slightly increased power is required to stabilize the switching event; (3) Electrical changes correlated with HAXPES results and literature indicate that (i) the forming/set electrical power defines the oxygen vacancies concentration in the a-HfO₂ and thus the stability of the resistive switching properties and (ii) the stable resistive switching can be described by a push-pull model of oxygen vacancies migration under the influence of an electrical field; (4) Besides, carbon segregation at the Ti/a-HfO₂ interface – while increasing the electrical power or cycling the device – shows that the defects physics is not limited only to oxygen vacancies; other defects may thus contribute under electrical stress to the resistive switching phenomenon and need to be included in theoretical models to correctly describe the switching characteristics.

Finally, according to the presented HAXPES results, the Ti/AVD a-HfO₂/TiN RRAM cells are classified to the valence change mechanism. The resistive switching mechanism is attributed to the creation and rupture of oxygen vacancies-based conducting filaments and the Ti/HfO₂ interface oxidation is of

central importance for the defect balance of the RRAM cell. Most importantly, a reduction of carbon content in the AVD-deposited HfO₂ improved the reliability of these memory cells.

ZUSAMMENFASSUNG

Aktuelle Speichertechnologien, wie z. B. DRAM, SRAM und NAND-Flash, die aufgrund der Skalierung jenseits der 16 nm Generation an Grenzen stossen, haben in den letzten zwei Jahrzehnten zur Forschung und Entwicklung neuer Speichertechnologien geführt. In den letzten Jahren wurden nicht-flüchtige Speicher (sogenannte „nonvolatile memories“, NVM), wie Phasenänderungs- (PCRAM), ferroelektrische (FRAM), magnetische (MRAM) und resistiv-schaltende Direktzugriffsspeicher (RRAM), intensiv studiert. Unter diesen Kandidaten ist RRAM ein sehr vielversprechendes und weltweit studiertes Konzept für alternative NVM und eine bessere potenzielle Option als der NAND-Flash hinsichtlich der Energiedissipation (Schreib- und Lesestrom im μA Bereich im Vergleich zu mA) und der Prozessintegration.

Am IHP wurde erfolgreich ein CMOS-kompatibles TiN/Ti/HfO₂/TiN RRAM Modul mit einem Auswahltransistor (1T1R-Speicher) integriert.

Dennoch sind die Zuverlässigkeit und das noch nicht vollständige Verständnis des Widerstandsschaltmechanismus Hauptgründe für die limitierte RRAM Speichertechnologie-entwicklungen für zum Beispiel drahtlose Sensorknoten (sogenannte „wireless sensor nodes“ (WSN)). Die noch unklaren atomaren Mechanismen der HfO₂-basierten Widerstandsspeicher und die physikalisch/chemischen Änderungen im Isolator müssen identifiziert werden, um eine wesentliche Verbesserung der Leistungsparameter zu erzielen. In dieser Arbeit wurde deshalb die Ti/HfO₂ Grenzfläche durch komplementäre, materialwissenschaftliche Techniken untersucht.

Zunächst zeigte die Untersuchung an abgeschiedenen Ti/HfO₂/TiN Zellen, dass: (1) die Ti-Schicht Sauerstoffatome aus amorphem HfO₂ ($\alpha\text{-HfO}_2$) stärker bindet als aus monoklinen HfO₂ Filmen. (2) nicht nur Sauerstoff-Fehlstellen, sondern auch Verunreinigungen wie Stickstoff und Kohlenstoff, die aus der chemischen

Atomdampfabscheidung (atomic vapor deposition, AVD) resultieren, wurden mittels EDX in den HfO₂- Filmen detektiert.

Als nächstes ergab die elektrische Charakterisierung von Ti/AVD a-HfO₂/TiN Zellen (Spannung wurden an die obere Ti Elektrode appliziert, während die untere TiN Elektrode geerdet wurde) bipolares Widerstandsschalten nach einer Elektroformierung mit positiver Polarität. Außerdem deuten die in den Spektren mittels harter Röntgenphotoelektronenspektroskopie (HAXPES) beobachteten chemischen und elektronischen Änderungen, im Vergleich mit der Literatur, die Bildung einer n-Typ Dotierung im HfO₂ Film nach der Elektroformierung an, höchst wahrscheinlich aufgrund der Bildung von positiv geladenen Sauerstoff-Fehlstellen an der electrochemisch oxidierten Ti/a-HfO₂ Grenzfläche.

Um direkt die elektrischen mit den elektronischen und chemischen Veränderungen von ein und derselben RRAM Zelle zu vergleichen, wurde eine in-operando HAXPES Technik entwickelt. Diese einzigartigen Studien haben die folgenden Charakteristika der Ti/AVD a-HfO₂/TiN Zellen ergeben: (1) die so abgeschiedenen Zellen können bei relativ niedrigen elektrischen Strömen geschaltet werden. (2) Jedoch ist dieses Widerstandsschalten nicht stabil und eine Elektroformierung mit einer erhöhten Leistung ist erforderlich. (3) Die Korrelation der elektrischen Daten mit den HAXPES Spektren zeigt, dass (i) die elektrische Leistung die Sauerstoff-Fehlstellen Konzentration im a-HfO₂ Film definiert und damit die Stabilität des Widerstandsschaltens bestimmt, dass (ii) das stabile Widerstandsschalten durch ein Push-Pull-Modell beschrieben werden kann, in dem Sauerstoff-Fehlstellen unter dem Einfluss eines elektrischen Feldes migrieren. (4) Die Kohlenstoffsegregation an der Ti/a-HfO₂ Grenzfläche mit erhöhter elektrischer Leistung bei der Elektroformierung oder durch mehrfaches Schalten zeigt, dass die Defektphysik nicht nur auf Sauerstoff-Fehlstellen limitiert ist, sondern auch weitere Defekte zum resistiven Schalten beitragen können und somit die Schaltcharakteristika beeinflussen können.

Schließlich können die Ti/AVD a-HfO₂/TiN Zellen im Rahmen eines Valenzwechselmechanismus klassifiziert werden. Das Widerstandsschalten kann

hierbei als Bildung und Unterbrechen von Sauerstoff-Fehlstellen-Filamenten verstanden werden und die Ti/HfO₂ Grenzfläche spielt eine zentrale Rolle für die Defektphysik der HfO₂ Filme. Ferner wurde gefunden, dass die Verringerung der Kohlenstoffkonzentration in den HfO₂ Filmen die Zuverlässigkeit der Speicherzellen wesentlich verbessern kann.

TABLE OF CONTENTS

ACKNOWLEDGEMENTS	i
ABSTRACT	iii
ZUSAMMENFASSUNG	vii
TABLE OF CONTENTS	xi
1. INTRODUCTION	1
1.1 More Moore versus More than Moore approach.....	1
1.2 Wireless sensor networks	2
1.3 RRAM at IHP	5
1.4 Aim of the Thesis	6
1.5 Organization of the Thesis	7
2. RESISTIVE RANDOM ACCESS MEMORIES	9
2.1 Basic definitions	9
2.2 Unipolar vs. bipolar resistive switching	10
2.4 Interface vs. filamentary type resistive switching	12
2.5 Physical phenomena of resistive switching	13
2.6 Redox-related resistive switching	16
3. EXPERIMENTAL BACKGROUND	23
3.1 Photoelectron spectroscopy	23
3.1.1 Historical background	23
3.1.2 Instrumentation	24
3.1.3 Binding energy	25
3.1.4 Measurement sensitivity.....	29

3.1.5	Depth profiling methods	32
3.1.6	Data interpretation	35
3.2	Preparation of samples	43
3.2.1	Molecular beam epitaxy system	43
3.2.2	Atomic vapor deposition facility	46
3.3	Sample characterization	47
3.3.1	General information	47
3.3.2	Photoelectron spectroscopy set-ups	49
4.	RESULTS AND DISCUSSION.....	55
4.1	As-deposited Ti/HfO ₂ interface characterization	55
4.1.1	<i>In-situ</i> study	55
4.1.2	<i>Ex-situ</i> study	58
4.1.3	Oxygen vacancy formation energy in HfO ₂	63
4.1.4	<i>Off-line</i> characterization	66
4.1.5	Summary and conclusions	67
4.2	<i>Ex-situ</i> electroforming study of Ti/HfO ₂ /TiN cells	70
4.2.1	Electrical characterization	70
4.2.2	HAXPES characterization	71
4.2.3	Proposed electroforming model.....	75
4.2.4	Summary and conclusions	77
4.3	<i>In-operando</i> electroforming of Ti/HfO ₂ /TiN.....	79
4.3.1	Electroforming at low electrical power	79
4.3.2	Electroforming with increasing electrical power.....	81
4.3.3	Discussion.....	87

4.3.4	Summary and conclusions	88
4.4	<i>In-operando</i> switching of Ti/HfO ₂ /TiN cells	90
4.4.1	Electrical characterization	90
4.4.2	HAXPES characterization.....	91
4.4.3	Proposed resistive switching model	95
4.4.4	Carbon behavior during cycling.....	96
4.4.5	Summary and conclusions	98
5.	SUMMARY AND OUTLOOK.....	101
5.1	Summary	101
5.1.1	As-deposited Ti/HfO ₂ interface.....	103
5.1.2	<i>Ex-situ</i> study of electroformed Ti/a-HfO ₂ /TiN cells.....	104
5.1.3	Impact of electrical power on changes in Ti/a-HfO ₂ /TiN cells.....	105
5.1.4	Stable resistive switching in Ti/a-HfO ₂ /TiN cells.....	105
5.2	Conclusions	107
5.2.1	Resistive switching origin in Ti/a-HfO ₂ /TiN ReRAM cells	107
5.2.2	Improved Ti/a-HfO ₂ /TiN RRAM cells performance	107
5.2.3	Limitations of HAXPES	109
5.3	Outlook.....	114
6.	SCIENTIFIC VISIBILITY	117
6.1.	Publications in peer-reviewed journals	117
6.2.	Own presentations at conferences	119
	APPENDIX A Photoemission in quantum mechanical formalism.....	123
A.1	Hamilton operator.....	123
A.2	Fermi's golden rule	124

A.3	Photoemission process	125
APPENDIX B Other characterization techniques		129
B.1	Time of flight secondary ion mass spectrometry	129
B.2	Scanning transmission electron microscopy	130
B.3	Grazing incidence X-ray diffraction	131
B.4	X-ray reflectivity.....	132
APPENDIX C Thin film growth mode		135
APPENDIX D List of symbols.....		137
APPENDIX E List of abbreviations.....		143
REFERENCES		147

Chapter 1

INTRODUCTION

1.1 More Moore versus More than Moore approach

In 1965, Gordon E. Moore predicted that the number of transistors on a chip will double every 18 months.⁽¹⁾ This historical trend has become known as **Moore's Law**. In order to increase the performance of integrated circuits and control the main technological requirements and needs the International Technology Roadmap for Semiconductors (ITRS) was created.⁽²⁾ The nowadays microelectronic industry following ITRS requirements combines both digital and

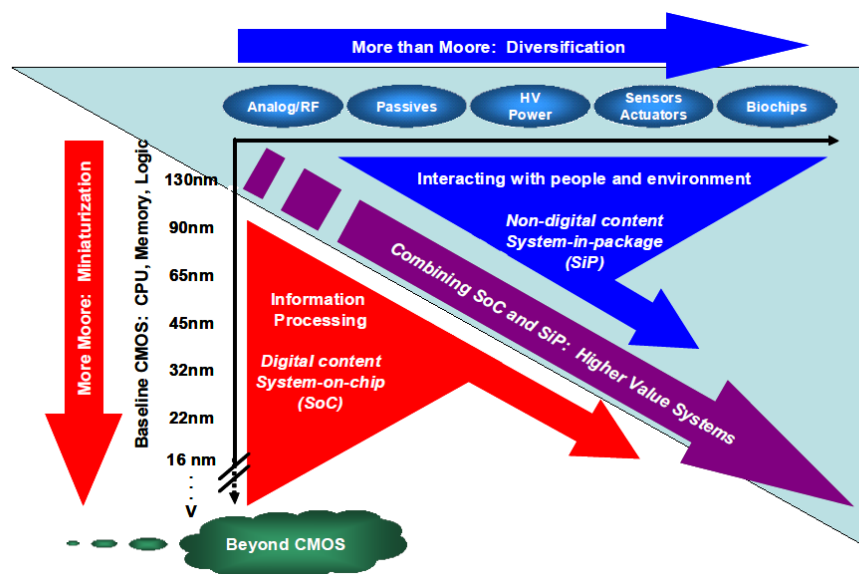


Figure 1.1: The combined need for digital and non-digital functionalities in an integrated system is translated as a dual trend in the ITRS: miniaturization of the digital functions ("More Moore") and functional diversification ("More than Moore").⁽²⁾

non-digital functionalities in one product by **miniaturization of the digital functions** (More Moore approach) and **functional diversification** (More than Moore approach). As shown in Figure 1.1, from the physical point of view, the More Moore approach will have to finally reach the miniaturization limits at the atomic scale. The migration of non-digital functionalities into the More than Moore approach from the system on board level into the system on chip (SoC) or into the system in package (SiP) gives the opportunity for the emergence of new technologies and applications for either daily life or niche markets, i.e. consumer electronics, high-end or mobile computing, sensor and medical devices.⁽³⁾ For example, RF CMOS applications are used in Bluetooth, GPS and Wi-Fi. LED lights are powered by high voltage drivers. CMOS image sensors are found in most digital cameras. MEMS applications are used in actuators, ink jet printers or sensors. Wireless sensor networks (WSNs) are used in telemedicine, security technology, etc. All these applications add value to the memory and computing devices that are made by the traditional Moore's Law technology.

1.2 Wireless sensor networks

An increase in ageing population and a decline in physical activities make the health care cost rising. Therefore, to control these costs while still providing the quality health service expected by patients, a paradigm shift in the health care landscape is needed. It is anticipated that in future the health care system will replace the doctor-/hospital-centric treatment by continuous patient-centric health monitoring performed at home. This is envisioned to be done by implantable or wearable wireless sensor devices which monitor patients' vital signs, e.g. brain activities, heart beats and communicates them to a hospital to be viewed by the doctor or nurses. For this purpose are invented inconspicuous, possibly robust and easy to use bracelets that will continuously measure and transmit vital data to a telemedicine service center (Figure 1.2(a) and Figure 1.2(b)). It is prognosis that the number of WSN for health and lifestyle monitoring will exceed 160 Million in

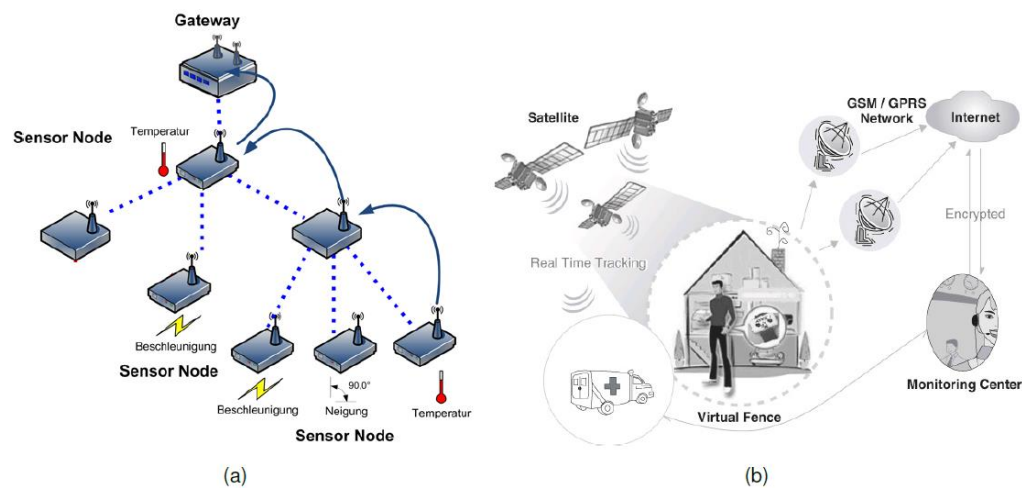


Figure 1.2: (a) A typical wireless sensor network. ⁽⁴⁾ (b) Example of wireless sensor networks for telemedicine for the electronic transmission of diagnostic images and medical, patient-related documents. ⁽⁵⁾

2017. ⁽⁶⁾ Therefore, it can be deduced that in the nearest future, the wireless monitoring of the results with the help of WSNs will play a central role in the technological world.

Under WSN is understood a technology with a defined number of sensor nodes that communicate with each other. In general, WSN can include thousands of autonomous and self-organized sensor nodes that combine sensing, data processing and wireless networking. By constantly growing needs, not only in the field of telemedicine, but also in the industrial automation (industrial 4.0), automotive industry, security and environmental technology, grows also the challenge of designing always **smaller, more powerful** and particularly **energy efficient sensor nodes**. The existing industrial solutions for wireless sensor nodes suffer from limited battery lifetime and functionality. ^{(7) - (9)} To guarantee low **power dissipation**, new software modules as well as innovative and energy-efficient hardware components such as microcontroller, radio modules and non-volatile memory must be integrated. Since sensor nodes are to be self-sufficient because of its purpose, especially a solution for **minimizing the use of energy** must be found. A large amount of energy is dissipated by the receiver, which must

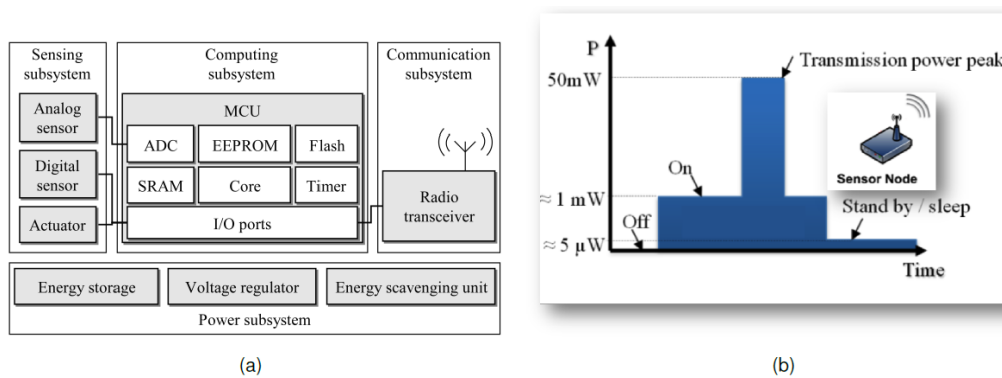


Figure 1.3: (a) Hardware architecture of a sensor node. ⁽⁵⁾ (b) Power dissipation as a function of time for typical sensor nodes.

be powered all the time (Figure 1.3(a) and Figure 1.3(b)). Approaches such as duty-cycling, which activates the receiver only at intervals, do not provide a required latency and asynchrony, which requires an event-driven system. Therefore, to reduce the energy dissipation and increase the lifetime of wireless sensor nodes, the development of the nanoelectronic memory for the computing subsystem (microcontroller unit (MCU) - Figure 1.3(a)) that will be as close as possible to the **universal memory concept** is needed. With this concept, it would be possible to dramatically reduce the power dissipation as a function of time, especially in the inactive mode (stand by) of the sensor node (see Figure 1.3(b)). Furthermore, the computing subsystem of a MCU integrates a processor core with program and data memory. The program uses Flash memories, while data are stored at the SRAM and EEPROM memories. With the universal memory concept, the advantages of the established memories could be combined: the non-volatility of Flash, the speed of SRAM and the cost benefits and density of DRAM.

There are several potential candidates which could be used as a universal memory. The new technology is based on a phase-change random access memory (PCRAM), magnetoresistive random access memory (MRAM), ferroelectric random access memory (FRAM) and resistive random access memory (RRAM).

Table 1.1: RRAM vs. Flash technology. Adapted from Ref. (10).

Property	Flash		RRAM	
	2009	2024	2010	Best projected
Year/status	90	18	90	5-10
Feature size F (nm)	$5F^2$	$5F^2$	$8F^2$	$8/5F^2$
Cell area	90	18	90	5-10
Read time (ns)	50	8	< 50	< 8
Write/erase time	1/0.1 ms	1/0.1 ms	40/40 ns	< 20 ns
Retention time (years)	> 10	> 10	> 10	> 10
Write cycles	> 10^5	> 10^5	> 10^{10}	> 10^{16}
Write operating voltage (V)	15	15	1.4/ - 1.4	< 0.5
Read operating voltage (V)	2	1	0.1	< 0.2
Write energy (J/bit)	> 10^{-6}	> 10^{-6}	10^{-11}	10^{-15}

In particular, main advantages of these technologies are the **low operating voltages, fast read/write times, good scalability and low production costs**. Another feature of these emerging concepts is the integration into the back-end-of-line (BEOL) part of the CMOS process without the need of high-temperature processes, as classical cell concepts used in today's front-end-of-line (FEOL) integration. Of all these new memory concepts, the RRAM technology in comparison to Flash (Table 1.1) represents a very promising approach in terms of energy dissipation, scalability, write/read and use of CMOS-compatible materials. In addition, an access time < 40 ns, a number of cycles > 10^{10} with write energy per cell of < 10^{-11} J/bit make RRAM technology a competitive candidate in the universal memory concept for the energy efficient WSNs.

1.3 RRAM at IHP

Among many different materials showing the resistive switching phenomenon, IHP has selected the TiN/Ti/HfO₂/TiN layers composition for RRAM applications.^{(11) - (14)} This RRAM system was pioneered by researches from the ITRI group from Taiwan.⁽¹⁵⁾ From the view point of material choice, HfO₂ is compatible with the standard BEOL (Bi)CMOS processing of IHP and different tool suppliers offer CVD-based equipment, contrarily to many other material systems, such as perovskite-type oxides.^{(16), (17)} Besides, it shows also high scalability and good memory performance.^{(14), (18), (19)} Even if the exact role of the

Ti layer is not yet fully understood,⁽¹¹⁾ its insertion between the TiN top electrode and the HfO₂ film^{(15), (20)} improves the memory performance in comparison to the TiN/HfO₂/TiN stacks.^{(13), (14), (21), (22)} This stack composition together with a select transistor (so-called 1T1R memory) were already integrated at IHP into 4 kbit RRAM test modules.⁽¹⁴⁾ Such architecture is characterized by much less demanding requirements for the lithographic steps employed in the cell fabrication.

Although the integration into a complex (Bi)CMOS clean room environment has been demonstrated, there are still many challenges remaining for these devices. Both the reliability and insufficient understanding of the resistive switching mechanism are the main issues limiting the RRAM technology development, as pointed out by ITRS.⁽²⁰⁾ The still unclear atomic-scale mechanism of HfO₂-based resistive switches and the identification of the material changes within the insulator must be addressed to suggest a knowledge-based improvement of device performance. In this frame, the Ti/HfO₂ interface is thoroughly investigated in this PhD Thesis.

1.4 Aim of the Thesis

The goal of this Thesis is to develop an *in-operando* hard X-ray photoelectron spectroscopy (HAXPES) technique as a key diagnostic for transfer basic materials research insights to redox-based resistive switching memory (ReRAM) prototyping development in the field of WSN applications. It is in the special focus to identify and understand the material changes within the HfO₂ film and/or at the Ti/HfO₂ interface to improve the performance of the TiN/Ti/HfO₂/TiN ReRAMs.

1.5 Organization of the Thesis

In **Chapter 2** is given an introduction to the RRAM topic. Then in **Chapter 3**, firstly the photoelectron spectroscopy, as the main technique used during these studies, is briefly reviewed. Next, the preparation of the samples, realization of the *in-operando* HAXPES setup and finally the conducted studies are presented. **Chapter 4** consists of the main part of this Thesis. In Section 4.1 are presented the results of the as-deposited Ti/HfO₂ interface investigation. Section 4.2 contains the *ex-situ* HAXPES characterization of the as-deposited versus electroformed Ti/HfO₂/TiN cells. *In-operando* HAXPES results of the applied electrical power impact on the electronic and chemical changes in the Ti/HfO₂/TiN cells during the DC sweep voltage cycling are presented in Section 4.3. The proposed resistive switching model in the Ti/HfO₂/TiN ReRAM cells and the role of the HfO₂ impurities on the resistive switching properties are given in Section 4.4. **Chapter 5** closes this Thesis with the summary, conclusions and the outlook.

Chapter 2

RESISTIVE RANDOM ACCESS MEMORIES

2.1 Basic definitions

The resistive random access memory, also called resistance change random access memory, is typically built as a sandwich structure: the insulating layer I is placed between two metal electrodes M. Many dielectrics have been found to show the resistive switching phenomenon while sandwiched between metal electrodes. The most prominent are: Al_2O_3 ,^{(8), (23)} Cu_2O ,^{(24), (25)} HfO_2 ,^{(21), (26) - (30)} NiO ,^{(31) - (39)} SiO_2 ,^{(40), (41)} TiO_2 ,^{(42), (43)} and Ta_2O_5 .^{(44), (45)} In some instances the same metal is used for both contacts and in other cases two metals are different with one being an active participant and the other being an ohmic contact. The application of current or voltage to the as-deposited MIM device produces a significant change of its electronic conductivity.⁽⁴⁶⁾

An initial and irreversible process called **forming/electroforming** is often required before the as-deposited MIM cell can be electrically switched between at least two different resistance states. An electroforming process typically requires somewhat larger voltages and/or currents and longer times than the subsequent resistive switching. This process is attributed to the non-destructive soft breakdown of the dielectric.^{(47) - (51)} Often, it turns an initially insulating state of the MIM cell into the state of a much lower resistance. The electroformed MIM cell can be set either to a low resistance (ON) state – logic 1, or reset back into the high resistance (OFF) state – logic 0, depending on the forming conditions. It may also happen that in some cases the electroforming process turns an initially

conducting MIM cell into a higher resistance state which allows for subsequent resistive switching.⁽⁵²⁾ In a first approximation, the forming voltage is proportional to the thickness of the insulating layer.^{(53), (54)} Thus, it indicates that the electric field in the insulating layer controls the rate limiting step of the electroforming.⁽⁵²⁾ The reset process is sometimes called an erase operation. In some devices more than two stable resistive states have been found, which could be used for multiplying the number of bits per cell.⁽¹⁰⁾ The modification of the metal/insulator interface resistance⁽⁵⁵⁾ or the alteration of the bulk insulator resistance⁽⁵⁶⁾ by defects or trapped carriers, or the formation of extended defects that bridge the electrode materials under an electric field^{(57) - (61)} were considered as possible mechanisms responsible for the origin of the resistive switching behavior in MIM structures. It was shown that these mechanisms sensitively depend on the conducting electrode materials.^{(11), (55)} However, the resistive switching mechanisms are often classified into a broader class. Depending on the current-voltage (I - V) characteristics, the resistive switching can be classified into the **unipolar** and **bipolar** modes (Figure 2.1).⁽⁶²⁾ Another classification is proposed depending on the conducting path, the **interface** or **filamentary** type resistive switching (Figure 2.2). In particular, the same insulator may show a completely different resistive switching behavior depending on the metal electrodes and the electrical power used during resistive switching. Both resistive switching classifications are explained in detail in the next paragraph.

2.2 Unipolar vs. bipolar resistive switching

In the **unipolar** mode (Figure 2.1(a)) the resistive switching procedure does not depend on the voltage polarity. After an electroforming process, a MIM cell being in an ON-state is reset to an OFF-state by applying a reset/erase voltage. During the set process to an ON-state, the current is limited by the current compliance and the set/write voltage is higher than the reset voltage.⁽⁶³⁾ The reset current is typically higher than the compliance limit set during the set operation.

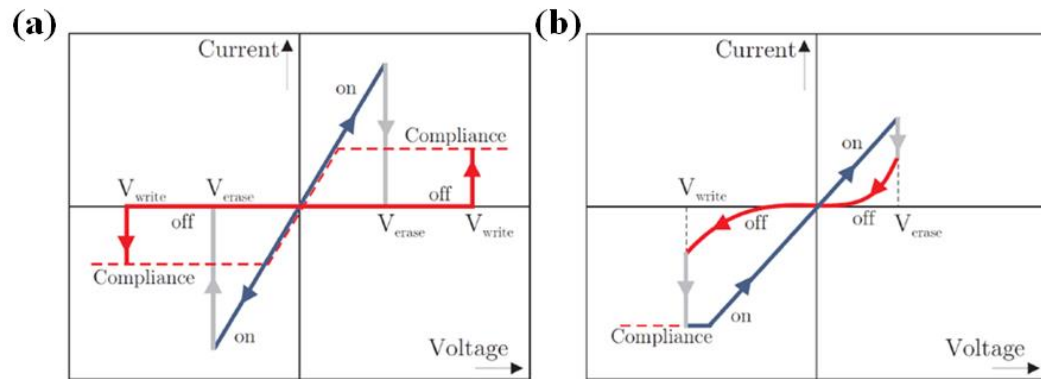


Figure 2.1: Schematic of the basic operation schemes of resistive switching memory cells. In unipolar switching, a single voltage polarity for set/write and reset/erase is applied (a). Bipolar resistive switching shows resistive switching depending on the polarity of the applied voltage (b). Adapted from Ref. (63) and Ref. (64).

In the **bipolar** mode (Figure 2.1(b)) the set to an ON-state occurs at one voltage polarity and the reset to an OFF-state on the reversed voltage polarity.^{(62), (63)} In order to show bipolar switching behavior the MIM system needs to have some asymmetry. It can be for example a dedicated voltage polarity used during the forming process or different materials used for top and bottom electrodes. The bipolar mode has often a gradual character. In most cases, the resistance change of a device proceeds rather continuously while in the unipolar mode an abrupt jump between two resistive states is observed. Such a gradual bipolar switching operation is promising for multilevel resistive switching memory applications in which a single memory cell can store several bits of information.⁽¹⁰⁾ Additionally, the bipolar resistive switching is divided into **clockwise** and **counter clockwise** types. In the clockwise switching the set operation occurs at a negative voltage polarity and reset at positive voltage polarity. In the counter clockwise it is opposite ($V_{\text{set}} > 0$, $V_{\text{reset}} < 0$).

2.4 Interface vs. filamentary type resistive switching

Depending on the location of the switching event, the resistive switching can be classified into the interface or filamentary type. Typically, in case of an **interface type** (Figure 2.2(a)), the resistive switching takes place at the interface between the metal electrode and the oxide⁽⁵⁵⁾, and the ON-state resistance is proportional to the electrode size.^{(55), (65)} For this type of devices, the resistance change is attributed to the field-induced change of the tunnel barrier or a Schottky barrier at the metal/insulator interface homogeneously over the entire electrode.⁽⁵²⁾ In the **filamentary type** (Figure 2.2(b)), the resistive switching is based on the creation and rupture of locally distributed conducting filaments. Their creation is determined by the electric field, while the subsequent switching takes place at a local spot along this filament, either at the metal/insulator interface or in the interior of the insulator. Thus, in the first approximation the switching voltage is independent on the insulator film thickness. Results obtained from calculations or simulations of the I - V characteristics indicates that the current compliance set

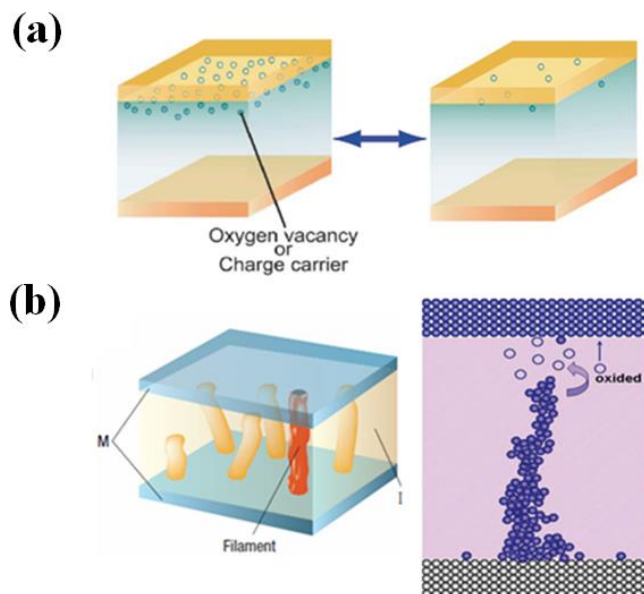


Figure 2.2: Interface (a) and filamentary (b) type resistive switching model adapted from Ref. (55) and Ref. (63).

during the forming/set process controls the size (thus the resistance) of the conductive filament(s).

In some instances, both the interface and filamentary type resistive switching have been observed in the same sample.⁽⁶⁶⁾ Indeed, the single filament type switching and the homogeneous interface type switching may be seen as two extremes of the same mechanisms. A spotty nature, showing limited areas of the interface type switching, or the multifilament type switching are in between of these two types.

2.5 Physical phenomena of resistive switching

RRAM is a very broad classification of memory technologies that includes five specific memory mechanisms (Figure 2.3). Each is defined by the specific physical mechanism responsible for their ability to switch resistance states between a high resistance and a low resistance. They are classified by their dominant physical operating mechanism. In general, the resistive switching can be driven by thermal, chemical or electronic mechanisms. The five RRAM

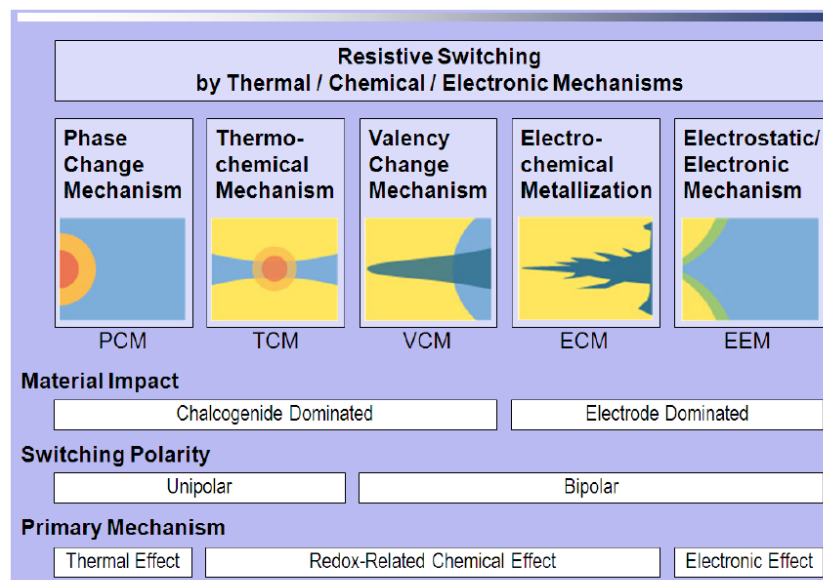


Figure 2.3: Classification of the RRAMs. Adapted from Ref. (67).

technologies are: phase change memories (PCM), electrostatic/electronic effect memories (EEM), thermal chemical memories (TCM), electrochemical metallization (ECM) and valence change memories (VCM).^{(58), (63)}

PCM exploit the unique behavior of chalcogenide glass (e.g. $\text{Ge}_2\text{Sb}_2\text{Te}_5$ (GST)). The phase change memory mechanism in chalcogenide glass involves electric-field-induced crystalline filament growth.⁽⁶⁸⁾ The crystalline and amorphous states of chalcogenide glass have dramatically different electrical resistivity. The amorphous high resistance state represents a binary 0, while the crystalline low resistance state represents a binary 1. When GST is heated to a high temperature (over 600 °C) its chalcogenide crystallinity is lost. Once cooled, it is frozen into an amorphous glass-like state and its electrical resistance is high. By heating the chalcogenide to a temperature above its crystallization point, but below the melting point, it will transform into a crystalline state with a much lower resistance. A careful material state control allows it to be thus transformed into one of four distinct states: an amorphous, a crystalline and two intermediate. Each of them has different electrical properties that allow a single cell to represent two bits, and thus doubling the memory density.⁽⁶⁹⁾ **EEM** is another broad category of RRAMs, involving three different electronic effects causing resistance switching mechanisms: (1) charge injection and trapping, (2) Mott insulator-metal transition, and (3) ferroelectric polarization reversal. A **charge-trapping switching** model is often suggested based on two observations: (1) I - V characteristics dominated by trap-controlled space charge-limited-conduction (SCLC) and (2) hysteresis in rectifying I - V characteristics of a Schottky-like junction. There are two mechanisms related to the basic concepts of charge trapping. First, as charge is injected into the insulator the device remains in the high resistance state until all traps in the insulator layer are filled – so called trap filled limit. At this point, the current increases exponentially and the device enters the low resistance state. Charge carriers injected and trapped in a MIM cell can either modify interface properties between the metal electrodes and the insulator or they can modify the band structure in the bulk insulator. Both mechanisms can alter the carrier

transport property and cause resistance change. Second, by the release of the trapped charges may recover the material to the initial states. Retention of charge trapped in these states, either at the interfaces or in the bulk insulator, depends on the release time of the trapped charge. The reversible bipolar resistive switching in rectifying I - V hysteresis can be explained by the change of the width and/or height of a Schottky-like barrier induced by trapped charge carriers in the interface states. Before a sample shows a stable switching a forming process is required, which may be related to the generation of oxygen-defect-induced states at the metal/oxide interface. In the **Mott insulator-metal** or Mott-Hubbard transition a charge injection into some transition metal compounds induces a transition from a strongly electron correlated insulator into a weakly electron correlated metal. The band gap in a Mott insulator exists between bands of like character while the band gap in charge transfer insulators exists between anion and cation states. The last electronic effect causing resistive switching in EEM is based on **ferroelectric polarization reversal**. The polarization of the ferroelectric insulator layer can modify its energy band structure. The changed band structure will impact the charge carrier transport properties and thereby cause bi-stable resistance. If the polarization vector of the ferroelectric insulator is parallel (antiparallel) to the electric field the depletion layer of an injecting contact will become thinner (thicker) and the Schottky emission from the injecting contact may become field assisted, both of which will lower (increase) the resistance of a MIM structure.

TCM, ECM and VCM are often combined into the term **redox-induced resistive RAM - ReRAM**.^{(67), (70)} These three types of memories are loosely connected by the fact that they share reduction/oxidation (redox) electrochemistry as an important component of their physical mechanism of the resistance switching. The redox electrochemical mechanisms can occur either at the metal/insulator contact interfaces, in the bulk insulator layer and/or along the conducting filaments in the insulator layer. The distinction between the TCM and the nanoionic ECM and VCM lies in whether the ion drift/diffusion and the redox electrochemistry mechanisms in the oxide layer are caused by (1) a thermal

gradient diffusion mechanism (TCM) or by (2) an electrostatic drift field (ECM and VCM). In many cases both mechanisms are present and it is just a matter of which is dominant. If the thermal gradient mechanism is dominant, the resistance switching is unipolar (TCM). Conversely, the resistance switching is bipolar, if the applied electric field drives the charged species (ECM and VCM). A more detailed description of the ReRAM mechanism is given in the next subsection.

2.6 Redox-related resistive switching

Common processes in ReRAMs

The operation conditions and the type of a ReRAM cell determine the relative current distribution and the specific electrochemical reactions at the interface. Metal electrodes in the ReRAM may carry only electronic current while the insulator layer may carry electronic and ionic currents. The ionic current may consist of anions and cations moving in an insulator layer in a direction determined by the applied electric field, and in addition can be, at least partially, blocked at the metal/insulator interface. The electrochemical reactions, oxidation at the anode and the reduction at the cathode are induced by the ionic partial current in the insulator layer. Additionally, the cations may stem from the anode metal. In the interior of the insulator layer and/or close to the metal electrode contact typically a Joule heating will occur. Moreover, at the interface may take place also ad-atom diffusion. An accumulation of mobile ions at one electrode and their depletion near the other, leads to so-called concentration polarization, which can be compensated (except in the space charge regions) by local redox reactions. In a consequence of concentration polarization, space charges and phase transformations may occur. Furthermore, Joule heating and the electrochemical interface reaction may also induce a phase transformation.

Due to the ReRAM nature, only one of the states (OFF, ON, or any intermediate state), can be thermodynamically stable and the other state(s) must be metastable.

The reason for that is due to the fact that there may be only one arrangement of atoms and ions which has the lowest free energy under the given external parameters. Moreover, in the ReRAM both states may be metastable. ⁽⁵²⁾

Thermochemical memory

TCM show unipolar resistive switching behavior because the thermochemical process dominates over the electrochemical process. To the TCM belong all metal oxides which show a high resistance in the most oxidized state and much lower resistance in reduced oxidation states (e.g. Al_2O_3 , CoO , CuO , NiO , SiO_2 , TiO_x , ZrO_x). The proposed resistive switching mechanism is shown in Figure 2.4. The initial electroforming process creates a conducting filament in the cell. During this process due to a thermoelectric breakdown a sudden current increase in the I - V characteristic is observed. Typically, a current compliance is used during the forming/set procedure to control the resistance of the filament in the ON-state,

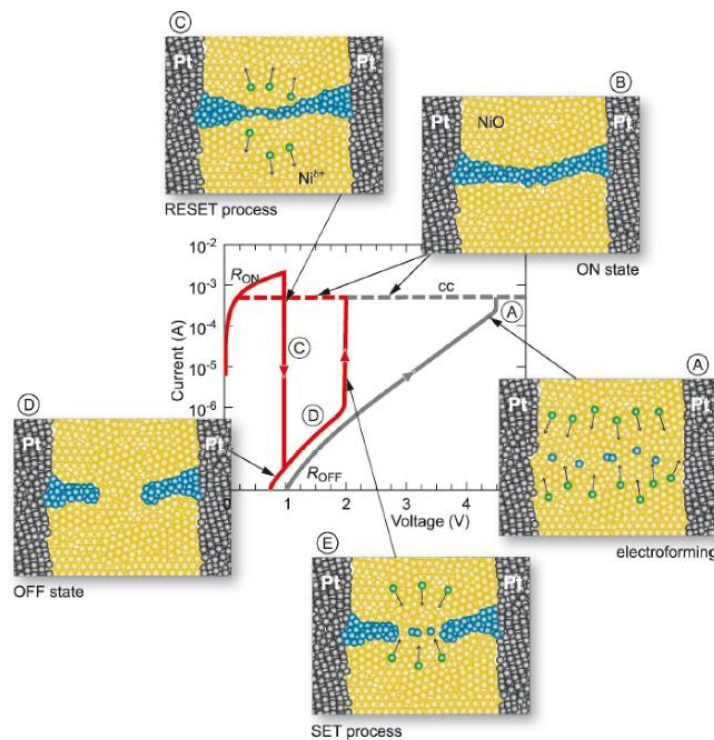


Figure 2.4: Proposed TCM resistive switching mechanism. ⁽⁵²⁾

and is released in the subsequent reset cycle and the current overshoot ruptures and partially dissolves the conducting filament. The set voltage is lower than the electroforming voltage because conducting filament is not completely dissolved but only interrupted during the reset process. The applied voltage and the corresponding high current during the reset operation result in Joule heating and a significant temperature increase. This leads to dissolution of the conducting filament by thermally-activated processes. Because current compliance is not used during the reset process, the reset current level is higher than the set. There are two processes conceivable for the rupture of the conducting filament: (1) the reduction of the free surface energy and (2) a thermally-activated re-oxidation of the conducting filament. The linear (ohmic) I - V relationship in the ON-state is consistent with the conduction of the metal-rich conducting filament created during the forming/set procedure. An exponential or superlinear I - V characteristic in the OFF-state can be explained by the semiconductive behavior attributed either to a thermally assisted Pool-Frenkel conduction or to a Schottky emission at the metal/oxide interface due to a high density of defect states deep in the band.

Electrochemical Metallization Memory

ECM are also called conductive bridge random access memories (CBRAM) or programmable metallization cells (PMC). The ECM cell consist of an ion conducting insulator layer (either solid electrolyte containing host cations, e.g. Ag_2S , Cu_2S , or an insulator, e.g. GeS , SiO_2 or WO_3 , typically doped with cations) sandwiched between an electrochemically active metal electrode (Ag, Cu) and electrochemically inert counter electrode (Au, Ir, Pt, W).⁽⁶⁴⁾ The basic principle of ECM operation is shown schematically in Figure 2.5. The as-deposited ECM cell is in the OFF-state. To set this cell into the ON-state a positive voltage is applied to the active electrode (here Ag). During the set process Ag is oxidized to Ag^+ ions which drift toward the counter Pt electrode. There, an electrochemical reduction and electro-crystallization of Ag^+ on the surface of the Pt electrode occurs. Due to this process an Ag filament grows from the Pt towards Ag

electrode until an electrical contact is established which defines the ON-state. Extended defects in the insulator layer are considered to facilitate the filament formation and be regarded as prerequisites for ECM operation. The growth of the conducting filament (its diameter) is controlled by the set current compliance for the operation. The ON-state resistance is determined by the physical nature of the filament and its contact at the active electrode. Both the filament thickness increase from few nanometers into relative thick components and a tunnel gap change into a galvanic contact at the active electrode will decrease the ON-state resistance. To reset the device back to the OFF-state an opposite voltage is applied which leads to a dissolution of the conducting filament. In principle, the reset mechanism will depend on the ON-state established during the set process before.

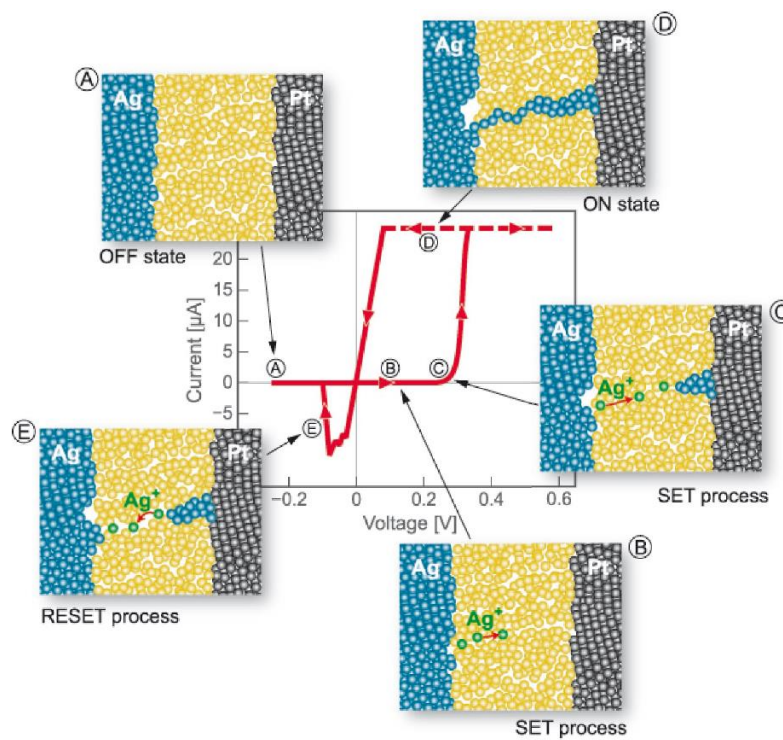


Figure 2.5: Proposed ECM resistive switching mechanism. ⁽⁵²⁾

Valence change memory

The valence change memory effect occurs in a wide range of metal oxides. The VCM cell consists of an active electrode (AE), a mixed ionic-electronic conducting layer (MIEC) and an ohmic counter electrode (OE). For VCM many variants are known. The resistive switching origin in VCM is typically based on the migration of anions. In Figure 2.6 is shown a proposed filamentary-type resistive switching mechanism for VCM composed with the n -type metal oxide. In the OFF-state there exists a filament composed of n -conducting oxygen vacancies (called plug) and a potential barrier in the front of the AE (called disc). By applying a negative voltage to the AE (left electrode on Figure 2.6), while the OE is grounded, positively charged oxygen vacancies are attracted from the plug into a disc region. As a result, a significant decrease of the barrier height and width due to the local reduction process occurs and the cell is set into the ON-state. To reset again the cell into the OFF-state, an application of a reversed voltage polarity to AE is required. During this process a local re-oxidation occurs and the oxygen vacancies are repelled out of this active interface. The Pt/ZrO_x/Zr

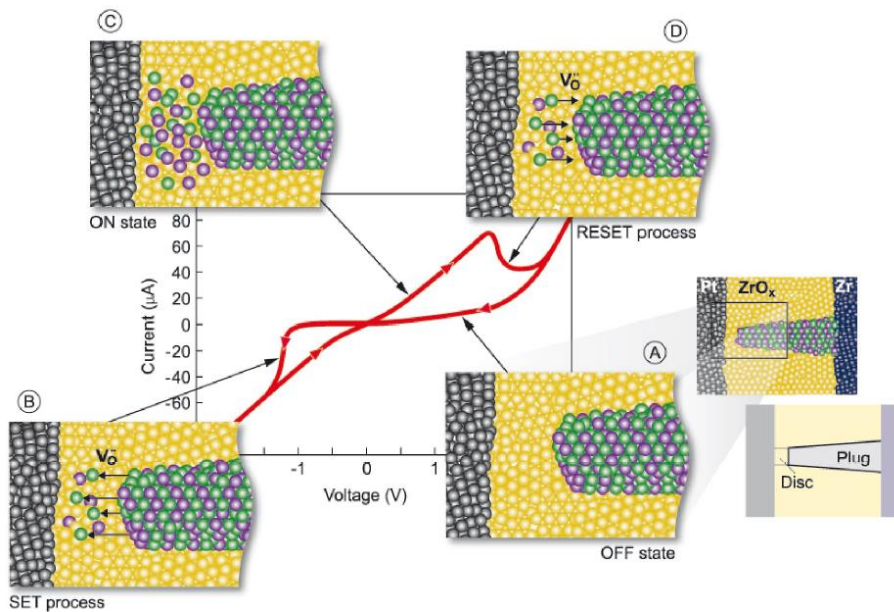


Figure 2.6: Proposed VCM resistive switching mechanism. ⁽⁵²⁾

VCM cell, presented in Figure 2.6, has shown a clockwise bipolar resistive switching. There are **three typical ways** proposed by Waser how **to arrive at VCM systems**.⁽⁵²⁾ (1) As AE, a metal with a low oxygen affinity (Ir, Pt, TiN) is used, and for OE, a metal with a low work function and a high oxygen affinity (Ti, Zr, Hf) is used. (2) In case, if for the OE a high work function/low oxygen affinity metal is used, then an electroforming is essential in order to introduce an ohmic behavior. (3) For the oxide, there are three different options: either (i) homogenous oxide film or (ii) homogeneous bilayer system consisting of an oxygen deficient *n*-type layer deposited on the OE and the same but fully oxidized few-nanometer thick oxide processed on the AE side, or (iii) heterogeneous bilayer system, where the second fully oxidized oxide layer is made from another oxide having a larger formation energy and/or a larger band gap than the nonstoichiometric first oxide. The location of the conductive path may vary as a function of the oxide morphology. In case of crystalline oxides, the local nanoionic redox process typically takes place at extended defects, while in case of amorphous and nanocrystalline oxides, the location of conducting filament may form anywhere in the cell. The filament's lateral size is determined by the electroforming process and influences the parameters of set and reset processes. Both processes show a strong nonlinear switching kinetics. The motion of the ions will be not strictly perpendicular to the electrode plain because of the (main) thermally assisted switching kinetics, but it will have lateral components as well. If the lateral effect dominates and takes place in the inner part of the cell, the VCM mode may be changed to the TCM mode controlled by the magnitude of the current compliance.

According to the results of this PhD Thesis and available literature, the Ti/a-HfO₂/TiN ReRAM cells are based on a VCM switching mechanism, as discussed in detail in the following, in the results part in Chapter 4.

Chapter 3

EXPERIMENTAL BACKGROUND

3.1 Photoelectron spectroscopy

In the following sections, basic knowledge about X-ray and hard X-ray photoelectron spectroscopy, as the two leading techniques used in this Thesis, will be briefly described. The quantum mechanical formalism of the photoemission process and the other used techniques are briefly summarized in Appendices A and B.

3.1.1 Historical background

X-ray photoelectron spectroscopy (XPS) has its origin in the **photoelectric effect** which was first explained by Einstein in 1905 (Nobel Prize in 1921). Throughout the 1950s and 1960s, Kai Siegbahn and his co-workers developed this effect into one of the most powerful tools for studying the composition and electronic structure of surfaces. In 1981, for one aspect of the XPS development, he received the Nobel Prize in physics.⁽⁷¹⁾

Photoelectric effect

When a surface is irradiated by a photon source, three events may occur (see Figure 3.1): (1) the photon can pass through with **no interaction**, (2) the photon can partially lose its energy by a scattering with an atomic orbital electron – so called inelastic scattering (e.g. **Compton effect** for high energy electrons), and (3) the photon can be absorbed and transfer its total energy to the atomic orbital electron leading to an electron emission from that atom – **photoelectric effect**.

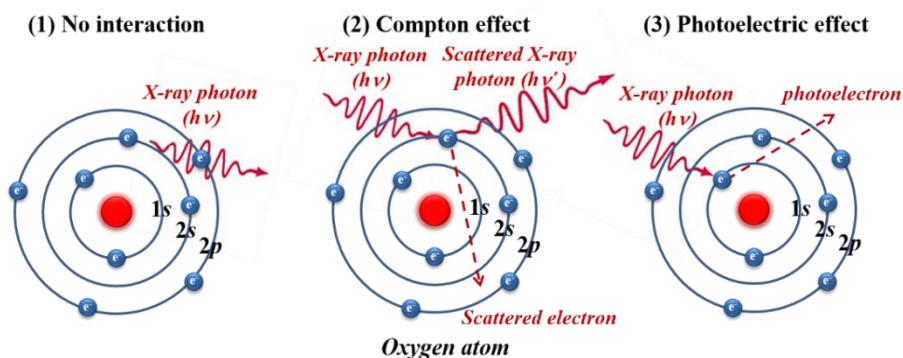


Figure 3.1: Photon interaction with an oxygen atom: (1) no interaction, (2) Compton effect, (3) photoelectric effect.

The photoemission process (10^{-16} s needed from excitation to emission) will only occur if the energy of the exciting photon ($h\nu$) is higher than the binding energy (BE) of the irradiated electron.

3.1.2 Instrumentation

The typical XPS instrumentation (Figure 3.2) consists of a **vacuum system**, an **X-ray source**, an **electron energy analyzer** and **data system**. The sample to measure is placed in the ultrahigh vacuum chamber via load-lock or preparation chamber and then irradiated with photons in the X-ray range. X-rays are created usually by impinging a high-energy (~ 10 keV) electron beam onto an anode (typically Mg or Al). During this time, core holes are created in the atoms of the anode material, by the emitted photoelectrons. Fluorescence X-rays are thus emitted and typically Mg or Al $K\alpha$ radiation with $h\nu = 1253.6$ eV or 1486.6 eV is used by XPS. During the measurement, anodes are usually cooled with water because most of the incident electron energy is converted into heat. The photoelectrons which have a sufficient energy to escape from the irradiated sample into the vacuum chamber are then separated and counted by the energy dispersive analyzer. When this X-ray flux is illuminating a sample, the spectrometer operation and data acquisition are controlled by the computer programs. The collected data are analyzed by software tools.

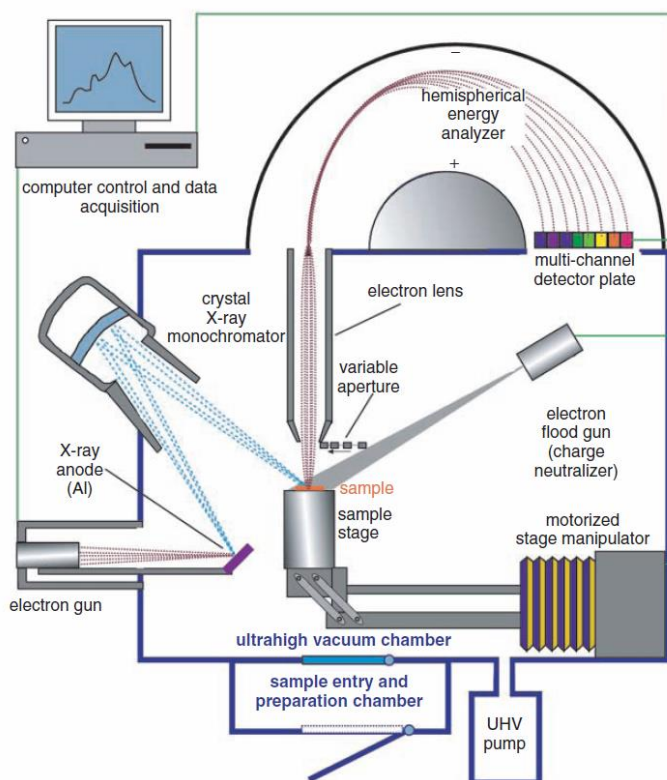


Figure 3.2: Schematic view of the XPS instrumentation.⁽⁷²⁾

3.1.3 Binding energy

The energy which is measured by the XPS analyzer is the kinetic energy (KE) of the ejected photoelectron. The binding energy (BE) of this photoelectron is calculated afterwards. In order to accurately calculate the binding energy of the photoelectron ejected from the conducting sample, one should place it in electrical contact with the XPS spectrometer. As shown in Figure 3.3, it puts the Fermi level (E_F) of the sample and the spectrometer at the same energy level. After that, the BE of the ejected photoelectron is referenced to E_F and equal to:

$$BE = h\nu - KE - \phi_s, \quad (3.1)$$

where $h\nu$ is the energy of the irradiating photons (called also the excitation energy), KE is the measured kinetic energy of the ejected photoelectron, and ϕ_s is the work function of the spectrometer.

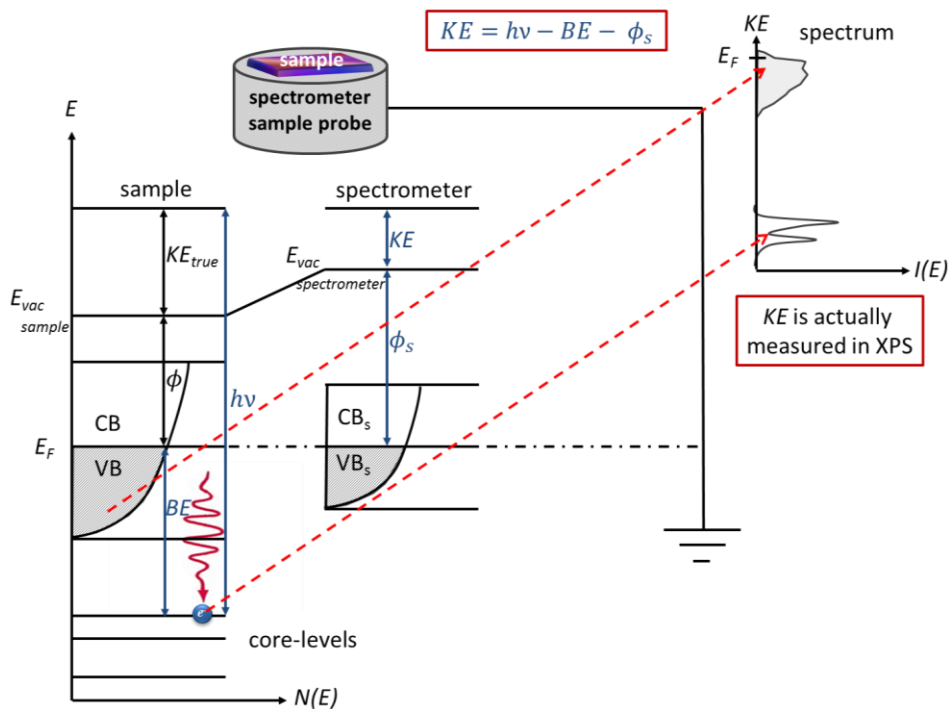


Figure 3.3: Energy level diagram with a schematic view of the photoemission process of the electrically conducting sample placed in electrical contact with the spectrometer. Adapted from Ref. (72) and Ref. (73).

ϕ_s can be calibrated by placing a clean Au standard in the spectrometer and adjusting the instrumental settings such that the known binding energy values for Au (e.g. $E_F = 0$ or $4f_{7/2} = 84$ eV) are obtained. Then, the linearity of the binding energy scale is calibrated by adjusting the energy difference between two widely spaced lines of the sample to their known values. Once the spectrometer energy scale has been calibrated, and the spectrometer is maintained in an ultrahigh vacuum (UHV) environment, it is assumed to remain constant. The instrument calibration procedure is given in ISO Standard 15472:2001, and more details can be found elsewhere. ^{(74) - (77)}

Binding energy shift

Because the binding energy in the photoelectron spectrum is usually measured with respect to the Fermi level, the binding energy value depends thus not only on

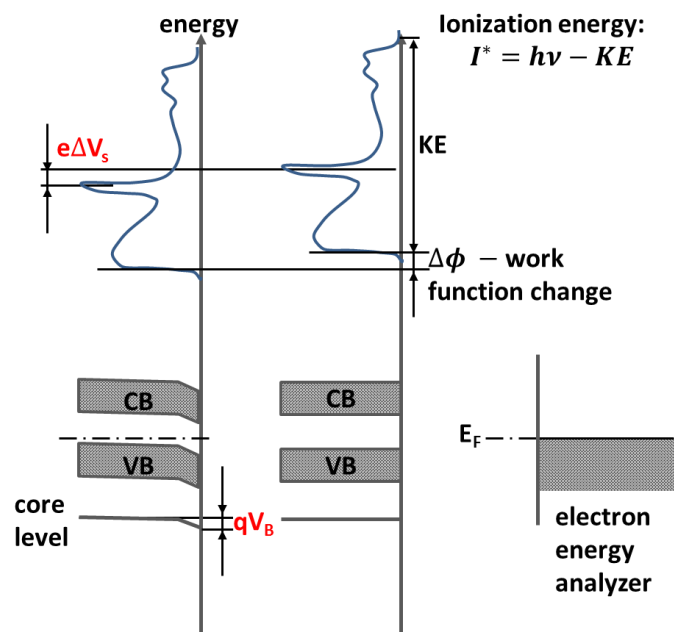


Figure 3.4: Schematic diagram of a photoelectron spectrum recorded from a semiconductor under conditions of band bending (left) and flat bands. ⁽⁷⁸⁾

the chemical state of the element in the compound (chemical shift) but also on the Fermi level position. Therefore, any change of the E_F position with respect to the band edges (so called **band bending**) will lead to a shift of the entire photoelectron spectrum relative to this reference level (see Figure 3.4). ⁽⁷⁸⁾ Band bending in a semiconductor or semiconducting oxide (whose depth depends on the doping and is usually on the order of several tens to some thousands of Å) may be caused by a variety of processes. For example, the existence of surface states in the band gap, adsorption of foreign material on the surface or change of a doping concentration at the interface will lead to the formation of a depletion or accumulation layer. Because the photoelectrons escape depth is very small (up to 3 nm), the photoelectron spectrum will thus represent only the electronic level binding energies in the outermost depletion region. For example, an effect of a doping type on the E_F position, and thus on the BE in the XPS spectrum, has been presented for silicon by Lebedinskii *et al.* ⁽⁷⁹⁾ Here, the binding energy of Si 2p core level electrons was taken for highly doped n^{++} - and p^{++} -Si samples. As can be

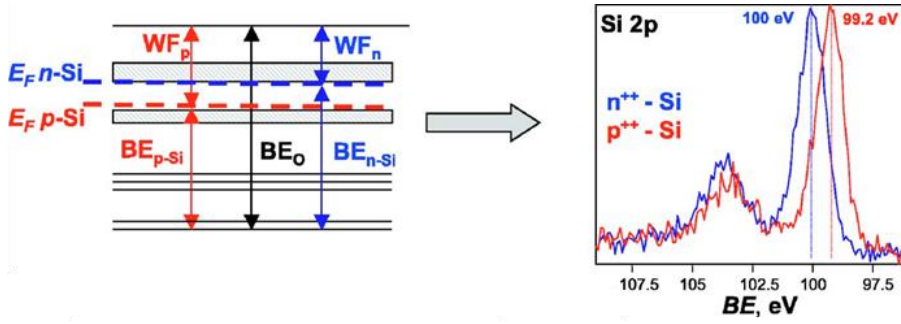


Figure 3.5: Effect of Si doping on the measured in XPS BE position: left - schematic energy diagram; right - Si 2p line recorded for n^{++} - and p^{++} -Si. ⁽⁷⁹⁾

seen in Figure 3.5, the Si 2p peaks appeared to have two distinct positions, separated by about the band gap of Silicon (~ 1 eV). Therefore, when n -type dopants are created inside the sample, XPS peaks shift towards larger binding energy, and when p -type dopants are created, a shift towards smaller binding energy is detected by XPS.

Koopmans' Theorem

The Hartree-Fock energy for N electrons in an atom is given by the equation:

$$E_N = \sum_{i=1}^N H_i + \frac{1}{2} \sum_{i=1}^N \sum_{j=1}^N (J_{ij} - K_{ij}) + V_{nn}, \quad (3.2)$$

where $\sum_{i=1}^N H_i$ is a core Hamiltonian, J_{ij} is a Coulomb energy, K_{ij} is an exchange integrals and V_{nn} is a potential.

After removing an electron from the k orbital, by the photoemission process, the Hartree-Fock energy for $N-1$ remained electrons in atom is now equal to:

$$E_{N-1}^k = \sum_{i=1}^{N-1} h_i + \frac{1}{2} \sum_{i=1}^{N-1} \sum_{j=1}^{N-1} (J_{ij} - K_{ij}) + V_{nn}. \quad (3.3)$$

The energy difference between Eq. 3.2 and Eq. 3.3 is the electron energy in orbital k , also called the orbital energy (ε_k):

$$E_N - E_{N-1}^k = h_k + \sum_{i=1}^N (J_{ki} - K_{ki}) = \varepsilon_k. \quad (3.4)$$

Koopmans' Theorem states that the BE of the emitted photoelectron from a k level is equal to the energy difference between the $(N-1)$ -electron **final state** and the N -electron **initial state**, so that the BE is the negative orbital energy $-\varepsilon_k$ of the ejected photoelectron:

$$BE = E_{N-1}^k - E_N = -\varepsilon_k. \quad (3.5)$$

This theory assumes thus that the other electrons remain “frozen” during the photoemission process.

Relaxation effects

In fact, other electrons in the sample, in the presence of a hole, relax to minimize the total electronic energy. The associated **relaxation energy** ($\delta\varepsilon_{relax} > 0$) decreases the measured binding energy of the ejected photoelectron. Relax can either be the electrons on the atom containing the core hole, so called **atomic relaxation**, or electrons on surrounding atoms, so called **extra-atomic relaxation**. Koopmans' Theorem neglects also the relativistic ($\delta\varepsilon_{rel}$) and correlation ($\delta\varepsilon_{corr}$) effects, which change the BE value. Thus, the measured BE value in the XPS in case relaxation occurs and Koopmans' Theorem is not valid, is given by:

$$BE = -\varepsilon_k - \delta\varepsilon_{relax} + \delta\varepsilon_{rel} + \delta\varepsilon_{corr}. \quad (3.6)$$

3.1.4 Measurement sensitivity

Sampling depth

Electrons excited with X-rays can travel only short distances through the solid due to their strong inelastic scattering with atoms. As shown in Figure 3.6, photoelectrons ejected from atoms very near the surface escape unscattered and contribute to the XPS peaks. Electrons originating from deeper regions partially lose their energy due to inelastic collisions with other electrons. Inelastically scattered electrons, which have still enough energy to escape from the sample, contribute only to the so called background (BG) signal (at lower KE than the

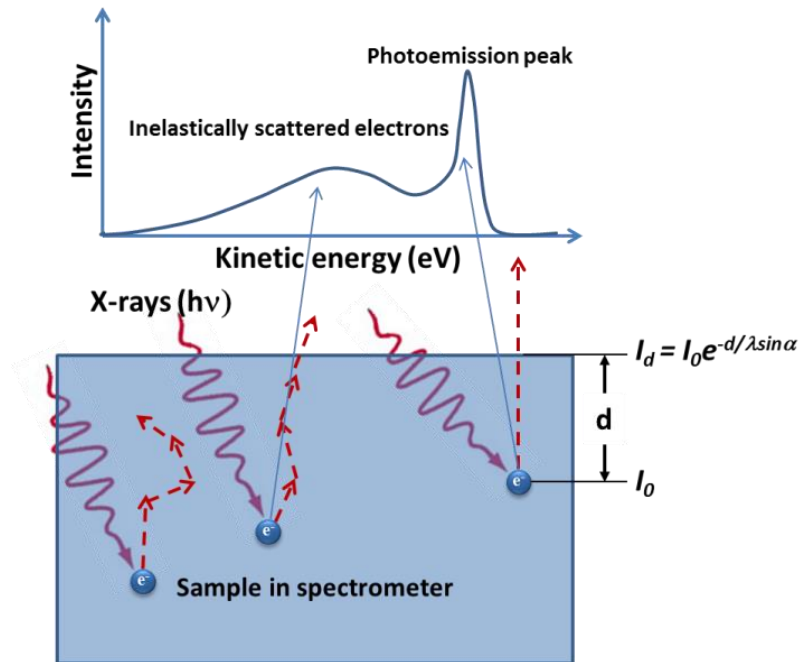


Figure 3.6: Kinetic energy distribution (i.e. electron spectrum) obtained due to the inelastic scattering process in the sample irradiated with X-rays.

XPS peak). The initial intensity (I_0) of the electrons flux emitted at a depth d below the surface is attenuated according to the Lambert-Beer law. As shown in Figure 3.7, the intensity (I_d) of the electron flux, as it reaches the surface without being scattered, exponentially decreases with depth accordingly to Eq. 3.7:

$$I_d = I_0 e^{-d/\lambda \sin \alpha}, \quad (3.7)$$

where α is the electron take-off angle related to the electron analyzer acceptance direction and the surface (see Figure 3.8) and $d/\sin \alpha$ is thus the effective distance travelled through the solid at that angle. The quantity λ is the average distance that an electron with a given energy can travel through this type of material without inelastic collisions and is called the inelastic mean free path (IMFP).

The electron probability to escape at $\alpha = 90^\circ$ from a depth d is shown in Figure 3.7. As can be seen, about 63% of the signal in the X-ray photoelectron spectrum will emanate from a depth of less than λ , 86% from a depth of less than 2λ , and

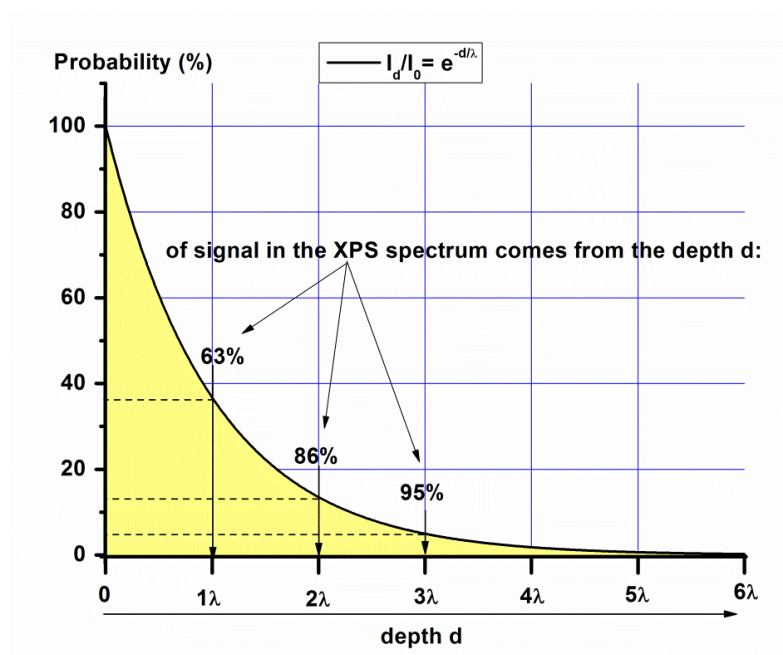


Figure 3.7: Photoelectron probability to escape from a depth d in normal emission geometry.

95% from a depth of less than 3λ . The depth from which 95% of all photoelectrons are emitted by the time they reach the surface is thus called the information depth (ID) of the XPS experiment:

$$d = 3\lambda = ID. \quad (3.8)$$

However, the vertical depth sampled decreases by a factor of $\sin\alpha$ if the take-off angle $\alpha < 90^\circ$:

$$ID_\alpha = 3\lambda \sin\alpha. \quad (3.9)$$

Inelastic mean free path

The IMFP determines quantitatively how surface sensitive the measurement is. The actual values of the IMFP of electrons in a matter are a function of their energy and the atomic density, composition and structure of the material being analyzed. The λ values (in \AA) can be calculated from the TPP-2M formula⁽⁸⁰⁾ for inorganic materials with a band gap E_g (in eV):

$$\lambda = \frac{KE}{E_p^2 [\beta \ln(\gamma KE) - (C/KE) + (D/KE^2)]}, \quad (3.10a)$$

$$\beta = -0.10 + 0.944(E_p^2 + E_g^2)^{-\frac{1}{2}} + 0.069\rho^{0.1}, \quad (3.10b)$$

$$\gamma = 0.191\rho^{-1/2}, \quad (3.10c)$$

$$C = 1.97 - 0.91U, \quad (3.10d)$$

$$D = 53.4 - 20.8U, \quad (3.10e)$$

$$U = (N_V \rho)/M = E_p^2/829.4, \quad (3.10f)$$

where KE is the photoelectron energy (in eV), E_p is the bulk plasmon energy (in eV), N_V is the number of valence electrons per atom (for elemental solid) or molecule (for compounds), ρ is the density of the material (in gcm^{-3}) and M is the material atomic or molecular weight.

Photoelectron spectroscopy can uniquely measure the electronic structure of a solid, but owing to the generally limiting electron mean free path, the technique is extremely surface sensitive, probing only the first few atomic layers of a structure. In conventional XPS, the λ values are typically between 1 and 3.5 nm. Thus, accordingly to Eq. 3.8, the maximum depth which can be investigated by the XPS technique is less than 10 nm.

3.1.5 Depth profiling methods

The XPS information depth dependence on the IMFP and the take of angle α gives an opportunity for a **non-destructive** investigation of the chemical composition of subsequent layers as a function of a depth.

- **α :** The principle of the ID dependence with α is used in angle-resolved XPS. In this method, the excitation energy is fixed and α is changed (Figure 3.8). The smaller the value of α is, the smaller ID becomes.
- **KE :** As shown in Figure 3.9, the IMFP of the photoelectron depends on its kinetic energy. The higher the photoelectron KE is, the bigger α is and consequently the ID value is increased.

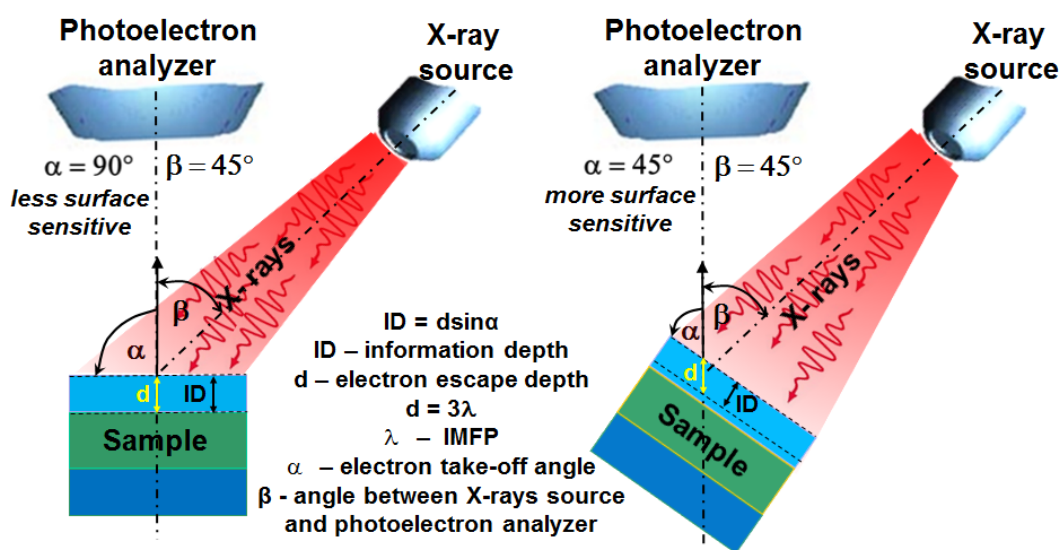


Figure 3.8: Principle of angle-resolved XPS.

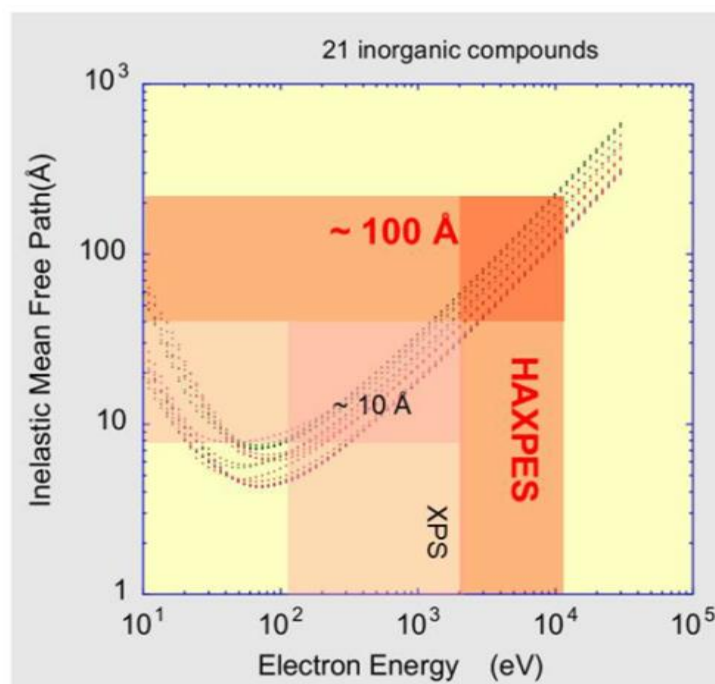


Figure 3.9: Inelastic mean free path values with respect to the kinetic energy of electron. Adapted from Ref. (81).

The sample depth composition can be also investigated by XPS in a **destructive** way. The destructive depth profiles are generated by an ion etching (typically accelerated monoatomic Ar^+ or Cs^+ ions to an energy between 0.5-5 keV) of the surface. At regular time intervals the bottom of the etching crater is analyzed by XPS. However, the monoatomic ion beams can reduce the accuracy of the analysis due to inducing an accumulation of atoms at the bottom of the crater. Although the measurement accuracy can be improved by means of rotating the sample during the sputtering time, the destructive approach always runs the risk to create artifacts. For example, preferential sputtering effects result in erroneous stoichiometry. It is thus clear that materials phenomena, being based on the defects physics, are in general not accessible by sputter XPS approaches.

Hard X-ray photoelectron spectroscopy

Resistive switching in oxides is closely related to the defect physics in the insulator and calls thus for the use of an innovative, non-destructive XPS technique called hard X-ray photoelectron spectroscopy (HAXPES). The HAXPES is a new variant of the well-established photoemission technique, which extends its range to much higher photoelectron energies up to 15 keV. According to the universal curve shown in Figure 3.9, excitation of the sample with hard X-rays increases the λ values by about 10 times in comparison to the excitation by standard X-ray sources in the laboratory with about 1.5 keV of energy. For this reason, not only the direct non-destructive access to the intrinsic bulk electronic structure of solids is facilitated, but also the extended non-destructive depth profiling of thin films and the study of buried interfaces (not possible by conventional photoemission) are accessible. Another advantage of the HAXPES technique is that due to its bulk-sensitivity the samples coming from the air can be in principle directly measured without any previous surface preparation (e.g. sputtering). In other words, surface contaminations have a smaller contribution to the total HAXPES signal. HAXPES is attracting increased scientific attention worldwide, mainly as a result of the availability of brilliant medium energy X-ray

beam lines at a number of synchrotrons. Currently, there exist six synchrotrons in the world offering HAXPES measurements, i.e. two in Asia: SPring8 (Hyōgo Prefecture, Japan) and Photon Factory PF (Tsukuba, Japan), three in Europe: DESY (Hamburg, Germany) BESSY (Berlin, Germany), and ESRF (Grenoble, France), and one in America: NSLS (Berkeley, USA). The intense activities at currently established synchrotrons push forward the technique and increase numerous examples of its power. In the view of increasing number of HAXPES applications from basic science to industrial research, new synchrotrons offering HAXPES end stations are under construction, e.g. Diamond (Oxfordshire, UK), CLS (Saskatoon, Canada) or Soleil (Saint-Aubin, France).

Furthermore, HAXPES needs to be based at synchrotrons, and is not a laboratory technique, because the ionization cross section of the photoelectric effect strongly decreases with increasing excitation energy ($\sigma \propto \frac{1}{(h\nu)^3}$) and thus the number of photoelectrons collected by the photoelectron energy analyzer. Therefore, in order to obtain high resolution and intensive signals in photoemission spectra, high flux and brilliance of photon beams is necessary. Both are currently only offered at modern 3rd generation synchrotrons.

3.1.6 Data interpretation

The most basic photoemission spectra analysis provides qualitative and quantitative information on all the elements (except H and He) whose concentration in the sample surface area is above 0.1 atomic %. Firstly, a wide scan or survey scan spectrum, often covering a range of several hundreds of eV, is taken. Next, the spectrum is calibrated (e.g. to the 84 eV of Au $4f_{7/2}$ or to the 285 eV of C $1s$ (C-C) peak position) for sample charging compensation. After calibration, the BG is subtracted and then the spectra can be analyzed. Much more details can be extracted from high-resolution spectra of each of the photoelectron features found in the wide scan spectrum. A typical XPS spectrum is shown in Figure 3.10.

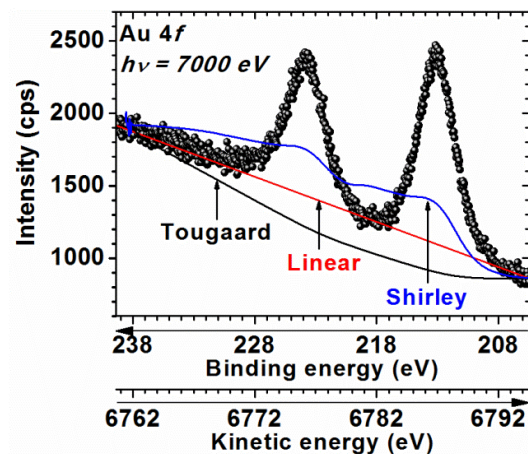


Figure 3.10: Three types of the often used background in the XPS: Linear, Shirley and Tougaard.

The x-axis is generally labeled **binding energy** given in eV; however it can also be plotted as a function of **kinetic energy**. According to Eq. 3.1, there is an inverse, linear relationship between BE and KE . The y-axis can either be given in **number of counts** or **counts per second (cps)**, both plotted in linear or logarithmic scale.

Background

To the XPS BG signal contribute these electrons which suffer energy losses, but still have sufficient energy to escape over the work function of the surface. The inelastically scattered BG intensity with increasing binding energy depends on the composition and structure of the sample as well as on the analyzed photoemission peak. The BG in photoemission spectra is non-trivial in nature. A variety of BG algorithms are used to model it. The most often used basic linear, Shirley and universal cross-section Tougaard BGs are shown in Figure 3.10. None of these BG algorithms are correct and therefore represent a source for uncertainty when computing the XPS peak area. Selection of one BG type over another is essentially chosen according to the least wrong rather than the most right. The **linear BG** is often used for fitting polymers and other materials with large band-gaps because they tend to have a relatively small step in the background over the

energy range covered by the peaks. Depending on the position of the chosen end points the peak area can significantly change. In the **Shirley BG** the BG intensity at any given binding energy position is proportional to the intensity of the total peak area above the BG in the lower binding energy peak range.⁽⁸²⁾ The general formulation of a **Tougaard BG** is based on the existence of an energy loss cross section $F(x)$ representing the probability that an electron at energy offset x undergoes a loss event and therefore appears as a contribution to the background.⁽⁸³⁾ Despite the fact that the Tougaard BG is the most accurate, if there are numerous peaks overlapping, it suffers from complications. Therefore, due to the easiest use of the Shirley BG, it is most widely used.

Signals in the photoemission spectra

In a typical XPS spectrum seven features can be distinguished. (1) **Sharp core-level peaks** - due to photoelectrons created within the first few atomic layers (elastically scattered), (2) **multiplet splitting** - occurs when unfilled shells contain unpaired electrons, (3) **background** - due to electrons emitted from deeper areas in the solid which are inelastically scattered (reduced KE), (4) **satellites** (shake-up and shake-off) - due to a change in Columbic potential as the photoejected electron passes through the valence band, (5) **plasmons** - created by collective excitations of the valence band electrons, (6) **Auger peaks** - produced by x-rays and (7) **valence bands**.

After a proper binding energy calibration and BG subtraction, the XPS peaks can be readily identified from their positions using tabulated binding energy values. In XPS, the core-levels use the nomenclature nl_j where n is the principal quantum number ($n \geq 1$), l is the orbital quantum number ($0 \leq l \leq n - 1$) and $j = l + s$ (where s is the spin angular momentum number and can be $\pm 1/2$). Except the s level ($l = 0$), all other orbital levels give thus rise to a doublet with the two possible states having different binding energies. This is known as spin-orbit (l - s) splitting.⁽⁸⁴⁾ The energy difference of l - s splitting can be found in a variety of

Table 3.1: Spin-orbit splitting j values and peak area ratios.

subshell	j	Area ratio
s	$1/2$	-
p	$1/2, 3/2$	1:2
d	$3/2, 5/2$	2:3
f	$5/2, 7/2$	3:4

databases, e.g. in Ref. (85) and in Ref. (86). These values will be needed when fitting the spectra. In general, the trend for separation is $p > d > f$. Besides, the energy difference for l - s splitting increases with atomic number of the element, i.e. it is easier to observe for heavy than for light elements. Moreover, based on the degeneracy (or multiplicity) of each spin state, $2j + 1$, the peaks will also have specific area ratios, as shown in Table 3.1 Next, when a core electron is removed by photoionization, satellite signals in the XPS spectrum may be observed. In case of shake-up satellite, the outgoing electron interacts with a valence electron and excites it (shakes it up) to a higher energy level. As a consequence the energy of a core electron is reduced and a satellite structure appears at a few eV higher binding energy than the original core level position. These shake-up peaks have discrete energies. The lost energy is equivalent to a specific quantized energy transition (i.e. $\pi \rightarrow \pi^*$ transition). If the valence electron is ejected from the ion completely (to the continuum), the shake-off satellites appear, seen as a broadening of the core level peak or contribution to the inelastic background in the XPS spectrum. The shake-off satellites can have a wide range of possible energies in the XPS spectrum, always with higher binding energy than the photoemission peak. In some photoemission spectra also the plasmon loss peaks (discrete energy losses) can appear when the photoelectron excites collective oscillations in the conduction band (free-electron gas). This feature is specific to clean metallic-like surfaces. Besides, when the excited ion relaxes Auger electrons

are emitted. In detail, electron from a higher lying energy level fill the inner shell vacancy with the simultaneous emission of an Auger electron. Auger peaks can be distinguished by changing the excitation energy. In detail, the kinetic energy of photoemission peaks shifts by the difference of the two excitation energies, while the kinetic energy of all Auger lines remains the same. The energy of an emitted Auger electron (KE^{Auger}) referenced to the vacuum level will be equal to the emitted photoelectron binding energy (BE) minus the binding energy of the electron that fills the vacancy in the core (BE^{L1}), minus the binding energy (in the presence of the core hole) of the level from where the Auger electron is emitted (BE^{L2}) minus the work function of spectrometer (ϕ_s): $KE^{Auger} = BE - BE^{L1} - BE^{L2} - \phi_s$. The last feature in the photoemission spectrum is a valence band region (VB) typically observed between 0 and 20 eV due to photoemission of valence (outer shell) electrons. An interpretation of this region is often complex, and was discussed for example in Ref. (87).

Further features that are only observed in the XPS spectra taken with non-monochromatized X-ray sources are called **X-ray satellites**. These sources excite the sample with more than one X-ray line. The low-intensity X-ray lines produce additional low-intensity photoemission peaks with higher KE than the primary photoemission peak. These features can be suppressed by using X-ray monochromators before illuminating the sample.

Chemical shifts

The observed binding energy variations in the XPS spectra are called the binding energy shifts or the chemical shifts. Binding energy can vary with the type of atom and the addition of other atoms bonded to this atom. The measured binding energy by photoemission spectroscopy is thus associated with covalent or ionic bonds between atoms. As presented in Eq. 3.6, both **initial** and **final state effects** have an impact on the observed binding energy value.

- **Initial state effects**

The binding energy of electrons in the initial state of an atom can be changed by the formation of chemical bonds with other atoms. To a first approximation, XPS peaks from orbitals involved in the binding energy process undergo the biggest chemical shift. As the formal oxidation state of an element increases, the binding energy of the emitted photoelectrons from that element increases. For example, since oxygen is more electronegative than carbon, it will draw electrons away from carbon. As the number of oxygen atoms bonded to carbon increases the carbon becomes more and more positively charged and the observed C 1s binding energy increases in a sequence of C-C < C-O < C=O < O-C=O < O-(C=O)-O. Because final state effects have a minor magnitude for different oxidation states, it is assumed that the initial state effects are responsible for the observed binding energy shifts:

$$\Delta BE = -\Delta \varepsilon_k. \quad (3.11)$$

In other words, according to Koopmans' Theorem, the measured change in binding energy reflects the change of the measured orbital energy, due to chemical oxidation. However, the relationship between the formal oxidation state and ΔBE may be altered by final state effects (see below). Furthermore, the changes in the density and the distribution of electrons of an atom resulting from changes in its chemical environment contribute to ΔBE . Thus, it is best to correlate ΔBE with the charge on the atom. The observed binding energy can be calculated using for example the charge potential model relating it to a reference energy BE^0 which is considered to be the BE for the neutral atom, the charge q_i on atom i , and the charge q_j on the surrounding atoms j at distances r_{ij} , as follows:

$$BE = BE^0 + zq_i + \sum_{j \neq i} \left(\frac{q_j}{r_{ij}} \right), \quad (3.12)$$

with the constant z . The last term of Eq. 3.12 due to its similarity to the lattice potential of a crystal, $V_i = \sum q_j/r_{ij}$ is often called the Madelung potential. It is

then apparent that the binding energy will increase if the positive charge on the atom will increase by formation of chemical bonds.

- **Final state effects**

In the photoemission process a photon of energy $h\nu$ ejects an electron from a sample surface. In contrast to the initial state, the final state can be viewed as one where one electron has been removed, or a positive potential has been added to the sample atom. However, in samples with many electrons the change can be complex, and therefore the photoemission process is a complicated many-body process. The interaction of the remaining photoionized system with the potential created by the core hole will for example affect the charge contained in the valence band. If one assumes that the valence band consist of discrete energy levels, these levels can be excited by the core-hole potential and be observed as satellites at higher binding energy in the core-level spectrum. Figure 3.11 shows the schematic spectra of both the system of no electron-electron interaction ($V = 0$) and for electron-electron interaction ($V \neq 0$). As can be seen, the center of gravity is the same in both cases, and is equal to Koopmans' binding energy (BE_K), which is the binding energy of the non-interacting electrons. In the spectrum of the interacting electrons, besides the main line, now additional lines (satellites) with higher binding energy (BE), appear. In a metal, the excitation possibilities in the valence electron sea are either electron-hole pairs, whose

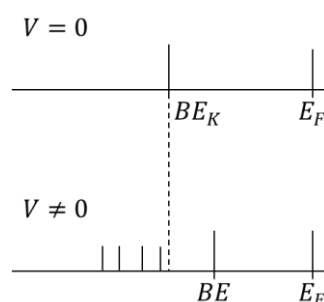


Figure 3.11: Schematic diagram of a photoemission spectrum with no electron-electron interaction ($V = 0$) and with electron-electron interaction ($V \neq 0$).⁽⁸⁸⁾

creation probability diverges towards infinity for electron-hole energy going to 0 ($\Delta E_{eh} \rightarrow 0$). Besides, electron-hole pair creation gives rise to an asymmetric photoelectron line shape. Even collective oscillations of the system of electrons relative to the system of positive lattice ions, so called plasmon peaks, can become excited after the photoemission process.

The final state effects, such as relaxation, multiplet splitting, multielectron excitations and core-level satellites give rise to energetic shifts, splitting of the peaks or the appearance of satellite peaks in the photoemission spectra. A quantum mechanical description of the complex photoemission process is given in Appendix A.

3.2 Preparation of samples

In this section, the preparation of samples by two different deposition techniques will be presented. It should be noted that the Ti/HfO₂ thin films were always deposited on the TiN/Si(001) substrates. A polycrystalline TiN bottom electrode was deposited on 8 inch hydrofluoric (HF)-treated single crystal *p*-Si(100) (15 Ωcm resistivity) wafer in the MSBA 580-TESW metallization chamber by a plasma assisted direct current magnetron sputtering of a titanium metal in the presence of a N₂/Ar gas mixture at RT.

3.2.1 Molecular beam epitaxy system

A part of the samples was prepared with the Ti/HfO₂ films grown by molecular beam epitaxy in the oxide chamber of the DCA 600 MBA system at IHP (Figure 3.12).

The molecular beam epitaxy (MBE) technique offers the growth of high quality epitaxial films with monolayer control. Any possible contaminations of such prepared films are avoided because the deposition is maintained under UHV conditions. The evaporation of the source material (purity better than 99.99%) can be carried out by means of either electron evaporation using electron beam (e-gun) or by thermal heating from a Knudsen cell (K-cell). The substrate material is protected against unwanted contamination thanks to a main cover shutter until the operating conditions of the material to be evaporated are reached. The homogeneity of the depositing film is increased by the rotation of the sample placed in the molecular beam of the evaporated material.

In the evaporation process by e-gun, a target anode material is held at a positive potential relative to the filament and bombarded with an electron beam emitted by a hot filament under high vacuum. To avoid chemical interactions between the hot filament and the target material, the filament is kept out of sight. A magnetic field directs the electron beam from the filament to the target and the electron beam is scanned over the target material to achieve a homogeneous heating. From the

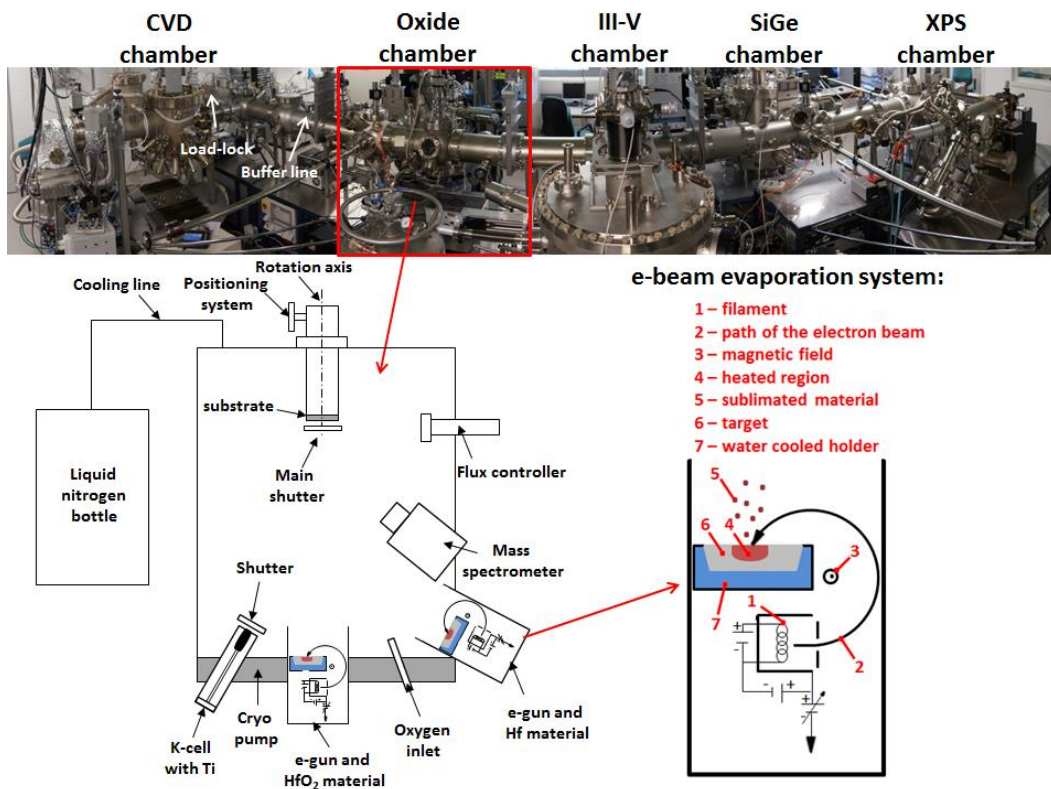


Figure 3.12: Photo of the molecular beam epitaxy DCA 600 MBE system at IHP and the scheme of the oxide chamber with detailed scheme of the e-beam evaporation system.

heated region of the target, the material is sublimated and thus transferred onto the substrate in form of a molecular or atomic flux.

An evaporation rate from K-cell is stabilized by heating of the source material for few minutes with a closed cover shutter. An abrupt start and deposition from a K-cell is possible by means of a cover shutter stop of the material. Thickness control in MBE is achieved by optical filters so that the evaporation power is set to stable flux conditions.

Substrate introduction into MBE system

First, the $2 \times 2 \text{ cm}^2$ in lateral size TiN/Si(001) substrates were introduced into the MBE load-lock chamber, which was subsequently pumped to high vacuum (HV) conditions (10^{-6} mbar). Once the HV was established, the absorbed contaminants

(water, carbon, etc.) on the sample surface were then degased at 200 °C for 20 minutes. Next, samples were transferred to the UHV oxide chamber with a base pressure of 3×10^{-10} mbar. The growth of HfO₂ on TiN/Si(001) substrates was carried out in two different ways, depending on the investigation purpose.

HfO₂ deposition from Hf oxide granulate

The HfO₂ film was deposited for 10 min on the TiN/Si(001) substrate at room temperature (RT), from an hafnium oxide granulate evaporated by an e-gun. During the deposition, the chamber pressure raised typically to 1×10^{-7} mbar, mainly due to oxygen outgassing from the source material. Then, the Ti growth, with different deposition times, was performed by thermal heating of Ti from a K-cell. The deposition and substrate temperatures were 1950 °C and 24 °C and the Ti beam equivalent pressure 3×10^{-8} mbar. During the Ti deposition, the oxide chamber was cooled by means of liquid nitrogen.

HfO₂ deposition from Hf metal and ¹⁸O isotope marked oxygen

For the deposition of ¹⁸O oxygen isotope-marked HfO₂ film, at the same time, a high purity Hf metal was evaporated by an e-gun and an O gas containing the ¹⁸O isotope was filling the MBE oxide chamber. The Hf deposition rate was fixed at 3 Å/s and the oxygen flow rate was controlled by maintaining the oxide chamber at a pressure of 1×10^{-5} mbar. The oxygen flow was also controlled by means of mass spectroscopy which monitored changes of the concentration of the ¹⁸O isotope. For 10 min the HfO₂ was deposited on the TiN/Si(001) substrate being either at RT or at 400 °C. It should be noted here that 400 °C is the temperature of the 4 inch sample holder and the effective temperature of the annealed 2×2 cm² substrate is lower (~320 °C). Next, the Ti layer was deposited on the HfO₂/TiN/Si(001) substrate at RT from a K-cell at 1695 °C for 7.5 h. The inner shroud of the oxide chamber was cooled during the Ti growth by means of liquid nitrogen.

3.2.2 Atomic vapor deposition facility

The second batch of samples investigated in this Thesis was prepared with the Ti/HfO₂ thin films deposited at the IHP's cleanroom facility. The HfO₂ films were grown by atomic vapor deposition technique (AVD) in the Aixtron Tricent AVD oxide module (Figure 3.13). In the AVD process the liquid precursors (MO Precursor) are delivered in the microliter range to the vaporizer (TriJet®) in discrete pulses. The vaporizer, the walls of the reactor and the showerhead are heated to the evaporation temperature. At the same time, the susceptor is heated to the precursor decomposition temperature. Subsequently, the carrier gas (Ar or N₂) transports an evaporated precursor to the reactor unit (AVD® Reactor). The precursor vapors are distributed through a showerhead to the heated wafer and decomposed, and the growth of the oxide film starts.^{(89) - (91)} The AVD HfO₂ films were grown onto the TiN/Si(001) substrates at 320 °C using the monomolecular liquid tetrakis(ethylmethylamino)hafnium (TEMAHf) Hf[N(MeEt)]₄ precursor and O₂ as oxidant.⁽⁹²⁾ In the following step, the Ti top electrode was deposited by plasma vapor deposition⁽⁹³⁾ onto the substrate being at RT.

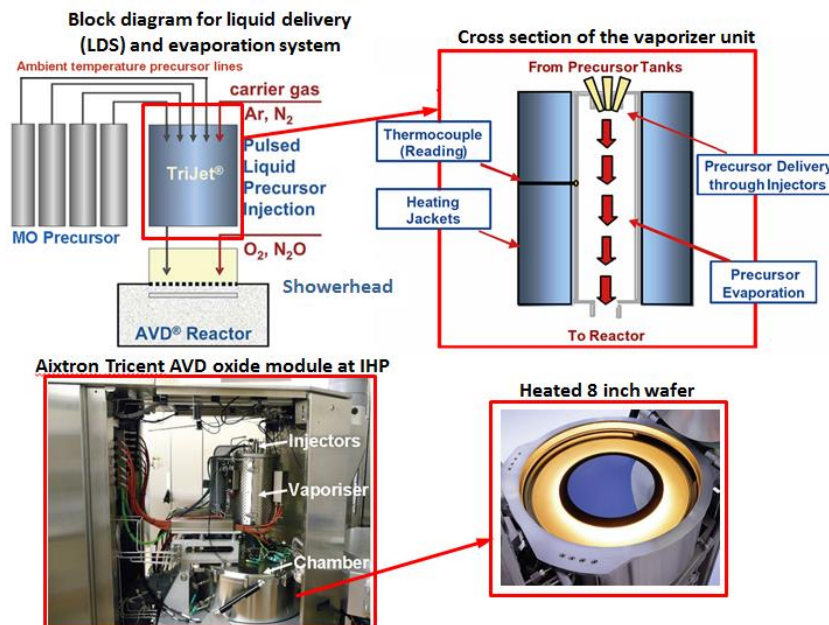


Figure 3.13: Schematic picture of the Aixtron Tricent AVD oxide tool at IHP.

3.3 Sample characterization

3.3.1 General information

XRR: The thicknesses of the Ti/HfO₂/TiN layers were determined by X-ray reflectivity (XRR) measurements. The XRR studies were performed with the Rigaku SmartLab diffractometer (Cu K α : $\lambda = 0.154$ nm) operating in parallel beam mode and then simulated with the RCRefSim program.⁽⁹⁴⁾

GIXRD: The crystallinity of the films was investigated by grazing incidence X-ray diffraction (GIXRD) measurements, with 1° angle of incidence using a Rigaku SmartLab diffractometer, equipped with a 9 kW rotating anode emitting Cu K α radiation ($\lambda = 0.154$ nm).

ToF-SIMS: The time of flight secondary ion mass spectrometry (ToF-SIMS) depth profiles were performed in order to open the TiN bottom contacts as well as to investigate the ¹⁸O profile across the RRAM stack. The ToF-SIMS measurements were done using the ION-TOF spectrometer.

STEM: The qualitative information about the as-deposited Ti/HfO₂/TiN layers, surface and interfaces were verified by high angle annular dark field scanning transmission microscopy with energy dispersive microscopy measurements. The TEM FEI Tecnai Osiris microscope with electron beam energy of 200 keV was used.

I-V: The electrical manipulation of the Ti/HfO₂/TiN RRAM cells was performed in a DC sweep voltage mode with a Keithley 4200 semiconductor characterization system. The signal was applied to the Ti top electrode whereas the TiN bottom electrode was grounded.

XPS + HAXPES: The experimental details about the XPS and HAXPES measurements are presented in Subsection 3.3.2.

In Table 3.2 are summarized the experimental information about the samples investigated during this Thesis: the sample name, the used HfO₂ deposition technique, the lateral dimension (L), the Ti/HfO₂/TiN thin films thicknesses (x)

and the characterization techniques performed (*CT*) of the different samples presented in each subsection of Chapter 4 are given.

Table 3.2: Experimental details.

Chapter	Sample	Deposited by	L (mm ²)	x (nm)	<i>CT</i>
4.1	A	MBE ⁱ⁾	20 × 20	(0-10)/10/73	XPS
	B	MBE ⁱⁱ⁾	20 × 20	12/21 [*] /73	XRR, XRD, ToF-SIMS,
	C	MBE ⁱⁱ⁾	20 × 20	11/15 ^{**} /73	HAXPES
	D	AVD	1 × 1	10/18/67	XRR, HAADF STEM-EDX
4.2	D				HAXPES
	E	AVD	1 × 1	10/18/67	Electrical, HAXPES
4.3	F	AVD	0.7 × 0.7	10/18/67	Electrical,
	G		0.7 × 0.7	10/14/112	HAXPES
4.4	G	AVD	0.7 × 0.7	10/14/112	Electrical,
	H		0.7 × 0.5		HAXPES

ⁱ⁾ HfO₂ was deposited from oxide granulate

ⁱⁱ⁾ HfO₂ was deposited from Hf metal and O gas containing ¹⁸O isotope

^{*} HfO₂ was deposited on the substrate being at room temperature

^{**} HfO₂ was deposited on the substrate being at temperature of 400°C

3.3.2 Photoelectron spectroscopy set-ups

XPS study

The XPS studies were performed at IHP's DCA 600 MBE system in order to *in-situ* monitor the Ti/HfO₂ interface reactions and the Ti growth mode on HfO₂ film. The X-ray radiation from Al K α line (1486.6 eV) was created by impinging an Al anode with an electron beam of 100 W. The emitted photoelectrons were collected by the Scienta Phoibos 100 hemispherical energy analyzer (Figure 3.14). The angle between the X-rays source and the photoelectron analyzer was fixed at 45°. The photoelectrons were collected at a take-off angle of 45°. The spectrometer operation and data acquisition were controlled by the SPECSLAB computer program.

HAXPES study

The HAXPES investigations were carried out at the P09 beamline of the Positron-Electron Tandem Ring Accelerator – PETRA III storage ring – at the Deutsches Elektronen-Synchrotron (DESY, Hamburg, Germany). Here, the Ti/HfO₂

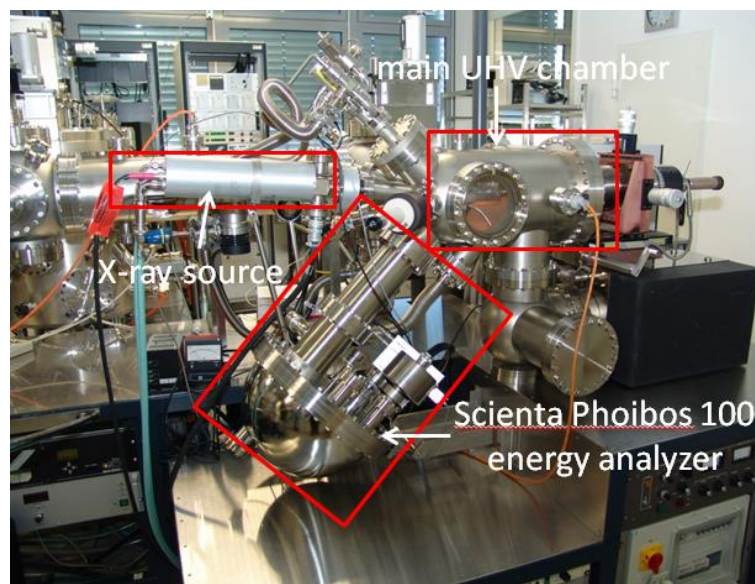


Figure 3.14: *In-situ* XPS instrument in the DCA 600 MBA system at IHP.

interface of the as-deposited and electrically manipulated Ti/HfO₂/TiN RRAM cells was investigated *ex-situ* and *in-operando*. The *ex-situ* term means that the samples were electrically manipulated outside and then investigated inside the HAXPES chamber. The *in-operando* term means that the samples were electrically modified and investigated inside the HAXPES chamber thanks to the specially developed setup presented hereafter.

- **P09 beamline**

P09 is one of the beamlines of the PETRA III facility at DESY in Hamburg (Germany). PETRA III is recently the biggest and most brilliant third generation synchrotron source in the hard X-ray regime in the world. It produces electrons with energy of 6 GeV with a beam current of 100 mA and an emittance of 1 nmrad. P09 beamline is designed for experiments requiring small beams, energy resolution, variable polarization and high photon flux operated in the hard X-rays regime with energies ranging from 2.7 to 50 keV. This beamline consists of three experimental hutches (EH). The EH3 hutch is designed for HAXPES experiments (Figure 3.15). The HAXPES UHV chamber is placed 94 m from the radiation source. The photoelectron energies up to 15 keV are measured using a SPECS Phoibos 225HV hemispheric electron analyzer equipped with 2D detection system (delay line detector (DLD), CCD camera, and a 4-channel micro-Mott spin detector) with designed energy resolution well below 100 meV. Typically, the experiments use X-rays directly from the high heat load Si(111) or (311) monochromator. Higher resolution can be obtained by using an additional channel-cut Si(333)/(555) monochromator. Focusing at the sample position is achieved with the same mirrors used for focusing in two leading up EH1 and EH2 experimental hutches. Cooling of the sample down to -253°C and heating up to 150°C is allowed by an Omicron 5-axis manipulator equipped with liquid helium (LHe). The analyzer can be positioned in an angle of 45° or 90° relative to the beam axis by means of air cushions. ⁽⁹⁵⁾

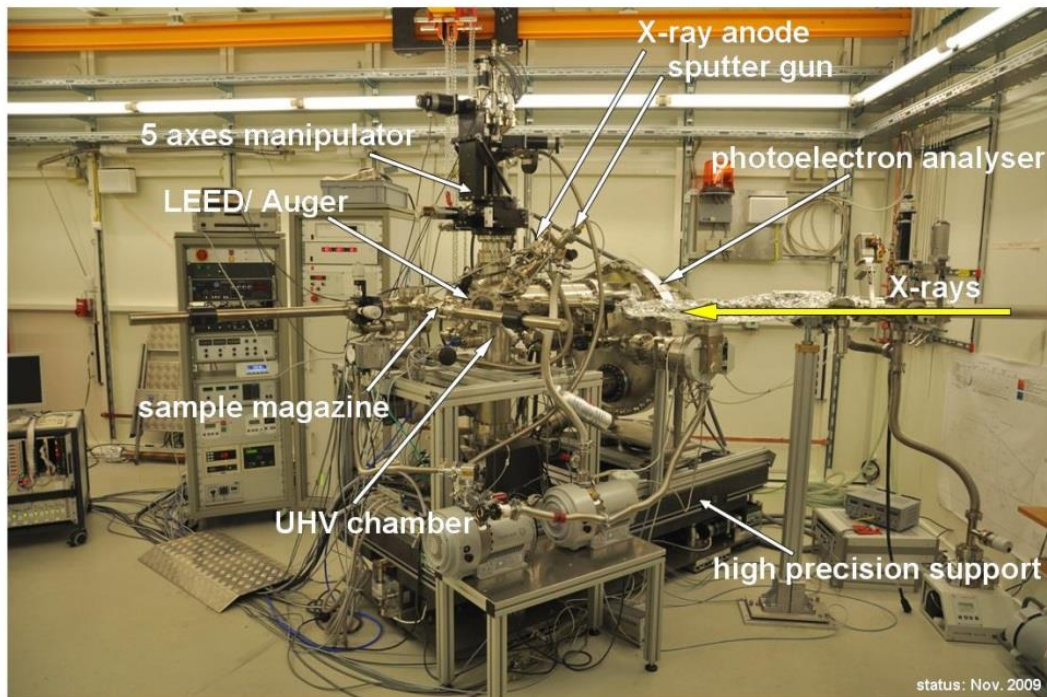


Figure 3.15: Photo of the HAXPES UHV chamber at P09 beamline at DESY in Hamburg (Germany). Adapted from Ref. (95).

- ***In-operando* HAXPES setup**

In order to directly correlate the resistive state of one and the same RRAM cell with its electronic and material changes, a special *in-operando* HAXPES setup, shown in Figure 3.16, was prepared. On the contrary to the integrated TiN/Ti/HfO₂/TiN RRAM devices,⁽³⁰⁾ the samples used for the HAXPES studies were prepared without the TiN top electrode (HAXPES information depth limitation) and with the lateral size of about three orders of magnitude larger (beam size requirement). First, an 8 inch wafer with deposited Ti/HfO₂/TiN/Si(001) films was diced into small pieces (typically 1 × 1 – 0.5 × 0.5 mm²). Then, a 200 × 200 μm² in area TiN bottom electrode contact was prepared by ToF-SIMS depth profiling (Appendix B.1). Next, conductive silver paste dots were put on the top and bottom electrodes. After that, the samples were heated at 120 °C for 10 minutes in order to fix the silver glue. Afterwards, the samples were

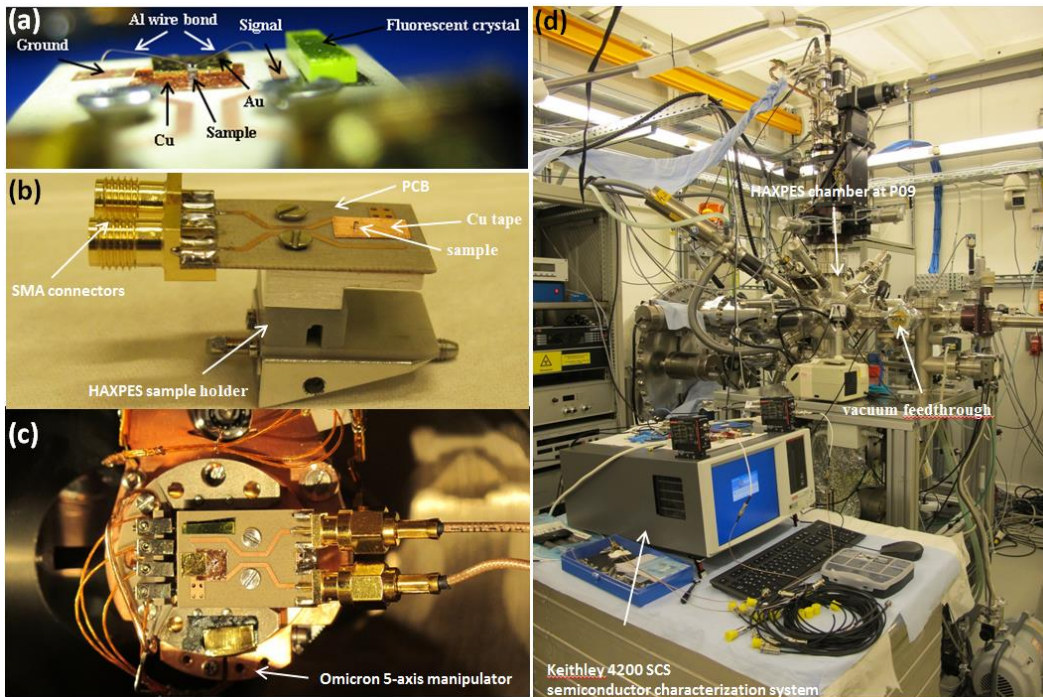


Figure 3.16: *In-operando* HAXPES setup developed at IHP.

mounted on a printed circuit board (PCB) by means of the conductive copper tape (Cu). Then, both electrodes were connected to the signal and ground copper lines by bonding aluminum wires (Figure 3.16(a)). Finally, SMA connectors were soldered to achieve external connections (Figure 3.16(b)). During the *in-operando* measurements, such a prepared PCB was placed on the HAXPES sample holder (Figure 3.16(b)) and attached to the 5-axis manipulator, inside the HAXPES vacuum chamber (Figure 3.16(c)). Next, this assembly was connected with cables via vacuum feedthroughs to the Keithley 4200 SCS semiconductor characterization system (Figure 3.16(d)).

In Table 3.3 are summarized the basic information of the XPS and HAXPES experimental parameters. In detail, the excitation energy ($h\nu$), the experimental geometry (β – the angle between the X-rays source and the photoelectron analyzer, α – the photoelectron take-off angle) as well as the information depth (ID) calculated accordingly to these parameters for the Ti $2p_{3/2}$ photoemission line are given. The ID values of electron travelling through the Ti matrix were

calculated accordingly to the Eq. 3.7 to Eq. 3.10, using the following parameters: E and α change depending on the experiment, $N_{VTi} = 4$, $\rho_{Ti} = 4.507 \text{ gcm}^{-3}$, $M_{Ti} = 47.867$, and $E_{gTi} = 0$. The collected XPS and HAXPES spectra were analyzed with CasaXPS software. The spectra were calibrated by means of the Au $4f_{7/2}$ peak position (84 eV) and the Shirley BG was subtracted from each photoemission spectrum.

Table 3.3: XPS and HAXPES experimental details.

Chapter	Sample	$h\nu^a)$ (eV)	$\beta^b)$ ($^\circ$)	$\alpha^c)$ ($^\circ$)	$ID^d)$ (nm)
4.1	A	1487	45	45	4.8
	B	8000	90	40	21.3
	C			83	33
	D			-	-
4.2	D	5500	90	90	23.7
	E	7000		45	20.7
4.3	F	7000	45	65	26.7
				80	28.1
	G			90	90
4.4	G	8000	90	90	33.3
	H				

^{a)} $h\nu$ is the excitation energy

^{b)} β is the angle between X-rays source and the photoelectron analyzer

^{c)} α is the photoelectron take-off angle

^{d)} ID is the information depth calculated for Ti $2p_{1/2}$ line (454 eV) in Ti metal

Chapter 4

RESULTS AND DISCUSSION

4.1 As-deposited Ti/HfO₂ interface characterization

In this section, the results of the as-deposited Ti/HfO₂ interface study will be firstly shown for the MBE- and then for the BEOL-processed samples.

4.1.1 *In-situ* study

Chemical analysis of the Ti/HfO₂ interface during the growth process

The Ti/HfO₂ interface chemistry was investigated *in-situ* by monitoring X-ray photoemission peaks at various stages of the Ti growth process on HfO₂ at IHP's MBE DCA 600 system. Figure 4.1 contains Hf 4*d* (a) and Ti 2*p* (b) XPS core levels of Sample A, measured after 10 s, 20 s and 240 s of the Ti deposition time. The decreasing substrate signal (Figure 4.1(a)) and the increasing overlayer signal (Figure 4.1(b)) confirm the successive Ti growth on HfO₂ by MBE. The decomposition of the Ti 2*p* spectra in Figure 4.1(b) was performed using Gaussian-Lorentzian and Doniach-Sunjic functions for the oxide and metallic components, respectively. A clear evolution of the Ti bonding chemistry versus deposition time is visible. In the initial stage of growth (10 s) Ti appears only in oxide form. Namely, Ti²⁺ (TiO) and Ti⁴⁺ (TiO₂) states are visible. However, while increasing the deposition time, a metallic Ti (Ti⁰) starts to form (20 s) and slightly shifts towards lower binding energy indicating a further growth of metallic Ti, while the buried Ti layer has an enhanced chemical reactivity with oxygen.

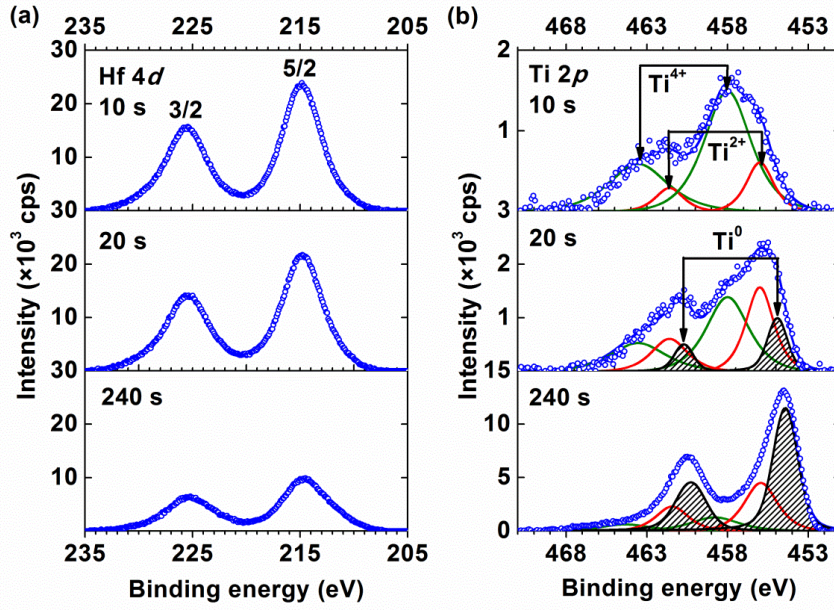


Figure 4.1: Hf 4d (a) and Ti 2p (b) XPS core-level spectra of Sample A taken after 10 s, 20 s and 240 s of the Ti growth on the HfO₂ substrate.

Determination of the Ti growth mode on HfO₂ substrate

The attenuation of the substrate signal in the XPS spectra can be used to determine the overlayer growth mode. Three main thin film growth modes are briefly reviewed in Appendix C. In this Thesis, the growth mode of Ti on the HfO₂ film was determined based on the analysis of the progressively attenuated Hf 4d_{5/2} photoemission line (BE = 214 eV). Following the approach proposed by Silar,⁽⁹⁶⁾ the best fit of the experimental points with the theory (Figure 4.2(a)) was obtained for the Volmer-Weber (or 3D) growth with the assumption that the Ti volume increases linearly with the deposition time. In the 3D growth, the substrate intensity I_0 is attenuated to the intensity I_d with increasing thickness of the average island height d (in nm):

$$I_d/I_0 = (1 - \sigma) + \sigma e^{-d/\lambda \sin \alpha}. \quad (4.1)$$

Here, σ is the HfO₂ surface coverage by the Ti islands ($\sigma = 0$ - uncovered film, $\sigma = 1$ - fully covered film); λ is the IMFP of the Hf 4d_{5/2} photoelectrons through Ti ($\lambda = 2.6$ nm), and α is the photoelectrons take-off angle ($\alpha = 45^\circ$).

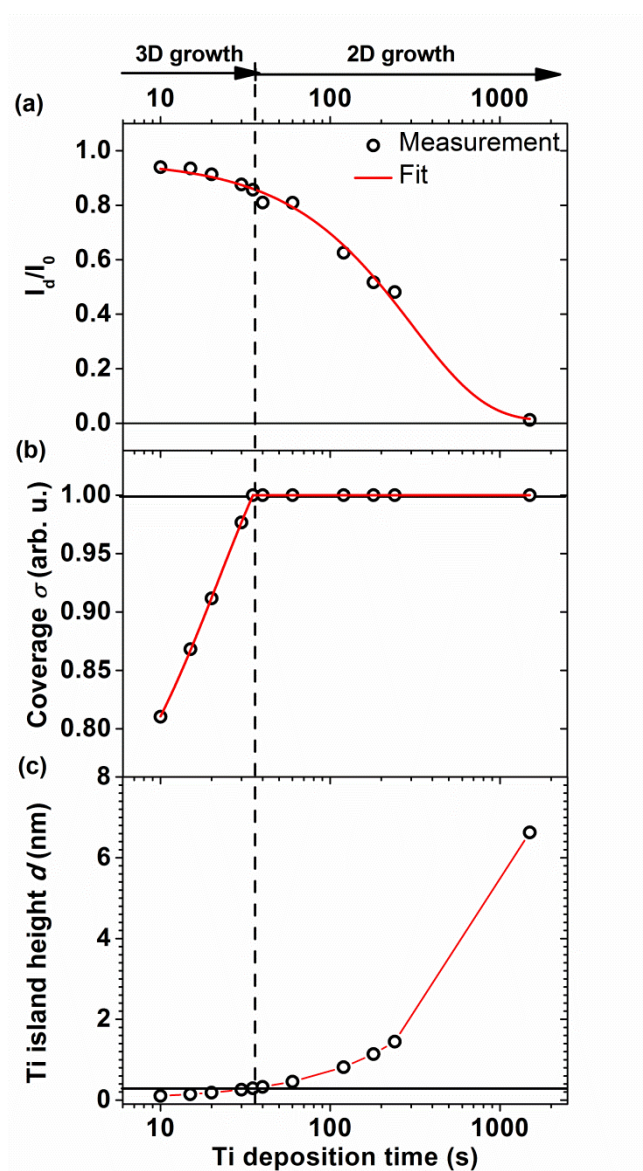


Figure 4.2: (a) Attenuation curve of the Hf 4*d* XPS line (b) HfO₂ surface coverage by the Ti islands and (c) average Ti islands height as a function of the Ti deposition time.

Results of this fitting procedure, shown in Figure 4.2, indicate that the full coalescence of the Ti islands take place after about 35 s (Figure 4.2(b)). After that, the HfO₂ surface is fully covered and the Ti islands height is about 3 Å (Figure 4.2(c)). Both, the time needed to fully cover the HfO₂ film and the average islands height after this time indicate that up to 35 s of deposition, there was not sufficient

Ti material to fully cover the HfO₂ film with the selected Ti deposition parameters. After that, Ti grows layer by layer.

4.1.2 *Ex-situ* study

Oxygen is present in the HfO₂ film and also at low concentration in the MBE chamber (10⁻⁹ mbar); therefore to investigate the origin of the Ti oxidation, the HfO₂ film was prepared with ¹⁸O isotope and complementary *ex-situ* ToF-SIMS and HAXPES studies were performed. Moreover, an impact of the HfO₂ deposition temperature (crystallinity) on the O diffusion into the Ti layer was also studied.

Chemical reaction of Ti with HfO₂ deposited at room temperature

First, the crystalline properties of Sample B prepared with HfO₂ deposited at RT were verified by GIXRD study (Figure 4.3). In this spectrum, there are three broad peaks which can be attributed to HfO₂. The one at 30° corresponds to a bunch of reflections from the monoclinic HfO₂ lattice: (011) or (110) at 24.5°, (-111) at 28.5°, and (111) at 31.5°. Because these peaks are very broad they overlap and form a single component, indicating the formation of an amorphous hafnium

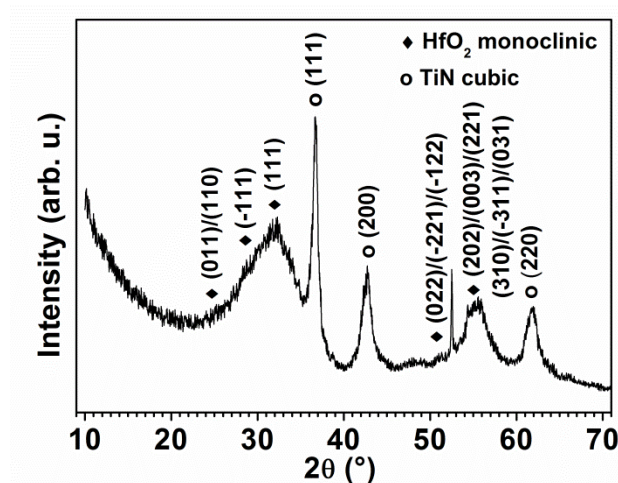


Figure 4.3: GIXRD measurement of the Sample B taken with 1° angle of incidence.

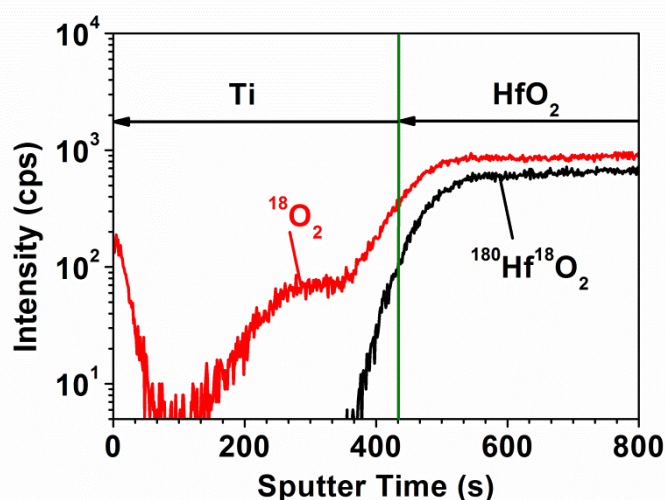


Figure 4.4: ToF-SIMS depth profile of the ¹⁸O isotope and ¹⁸⁰Hf¹⁸O₂ across the Ti and HfO₂ films of Sample B.

oxide containing only small crystallites in the monoclinic phase. The other two peaks located at the angles of 50° and 55° correspond also to the bunch of reflections of the HfO₂ monoclinic phase. These reflections are so close to each other that they cannot be well resolved for poorly crystalline, mostly amorphous thin films. Thus, in the first approximation the RT deposited HfO₂ is considered amorphous.

Next, the chemical reactions of Ti with amorphous HfO₂ (a-HfO₂) were verified by a ToF-SIMS study. As can be seen in Figure 4.4, the ToF-SIMS depth profile of the ¹⁸O₂ isotope performed across Sample B presents gradual oxygen diffusion from the HfO₂ film toward the Ti film and creation of a thick Ti/HfO₂ interface layer. The constant concentration between around 200 s and 400 s can be seen as a strong diffusion of the ¹⁸O₂ isotope from the HfO₂ into the Ti layer to a depth of up to several nanometers. The constant ¹⁸O₂ concentration between 500 s and more indicates also a successive uniform deposition of the HfO₂ film from the Hf metal and the atomic ¹⁸O₂ gas by MBE.

Then, the impact of oxygen diffusion on Ti oxidation states was studied non-destructively by HAXPES. The photon beam energy $h\nu$ and the photoelectron take-off angle α were chosen so that the signal in the Ti 2*p* HAXPES spectra

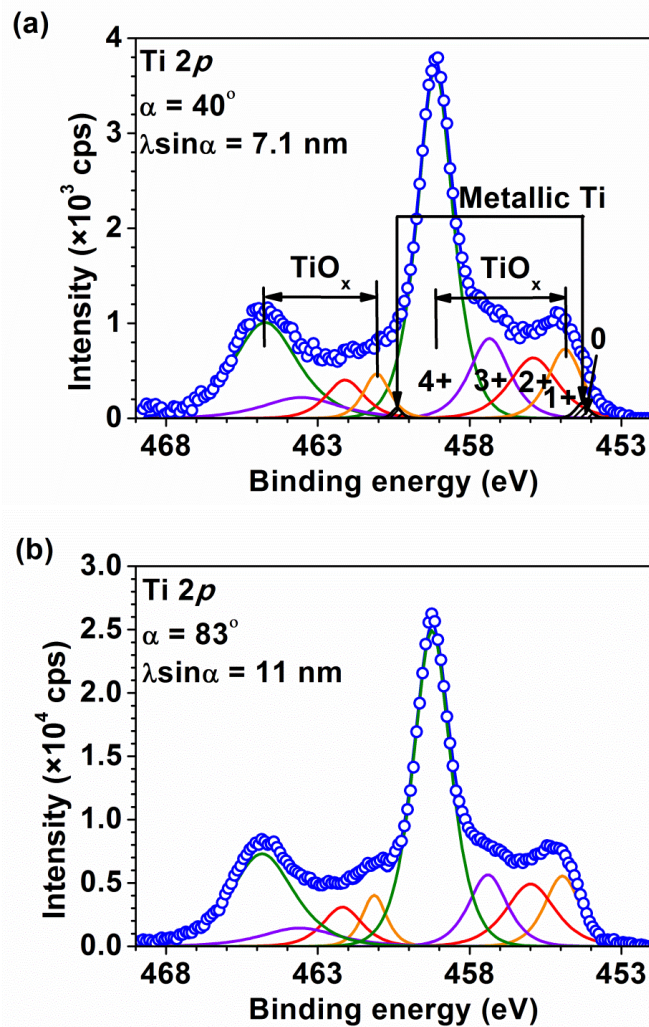


Figure 4.5: Ti $2p$ HAXPES spectra of Sample B taken with excitation energy of 8 keV and take-off angle α of (a) 40° and (b) 83° .

$(\lambda \sin \alpha)$ had originated mainly from the region slightly above (Figure 4.5(a)) and from (Figure 4.5(b)) the Ti/HfO₂ interface area. Both Ti $2p$ spectra were modeled with 5 spin-orbit splitting components attributed to the different Ti oxidation states. The components located at 454.1, 455.2, 456.3, 457.4 and 459.2 eV were assigned to the Ti⁰, Ti¹⁺, Ti²⁺, Ti³⁺ and Ti⁴⁺ states.^{(97), (98)} Each Ti $2p$ orbital doublet peak was fitted with an area ratio of 1:2 and a spin-orbit splitting of 6.17 eV for Ti⁰–Ti³⁺, and 5.80 eV for Ti⁴⁺. A Doniach-Sunjić line shape was used to model the Ti⁰ oxidation state and Gaussian-Lorentzian line shapes to model the

Ti¹⁺ – Ti⁴⁺ oxidation states. Modeled spectra indicate that the Ti layer at the interface with a-HfO₂ film is fully oxidized, whereas a small metallic contribution appears while going away from this interface. It is noted that this metallic Ti⁰ component is very small in intensity in Figure 4.5(a) but this interpretation of HAXPES data is supported by ToF-SIMS. Both ToF-SIMS and HAXPES data thus point to an enhanced chemical activity of the Ti/a-HfO₂ interface, as suggested by the *in-situ* XPS study shown in Figure 4.1.

Chemical reaction of Ti with HfO₂ deposited at 400°C

Next, the impact of the substrate temperature during the HfO₂ film deposition on the oxygen diffusion into the Ti layer was investigated. The GIXRD results of Sample C (Figure 4.6) have revealed that the HfO₂ film fully crystallizes in the monoclinic phase while the substrate holder temperature is kept constant at 400 °C during the deposition. In comparison to the spectra shown in Figure 4.3, the peaks corresponding to the monoclinic lattice reflections (011)/(110) at 24.5°, (-111) at 28.5°, and (111) at 31.5° are now well resolved. It can be concluded that the HfO₂ film deposited on the substrate at 400 °C is monoclinic.

The Ti interaction with monoclinic HfO₂ (m-HfO₂) was then verified by the ToF-

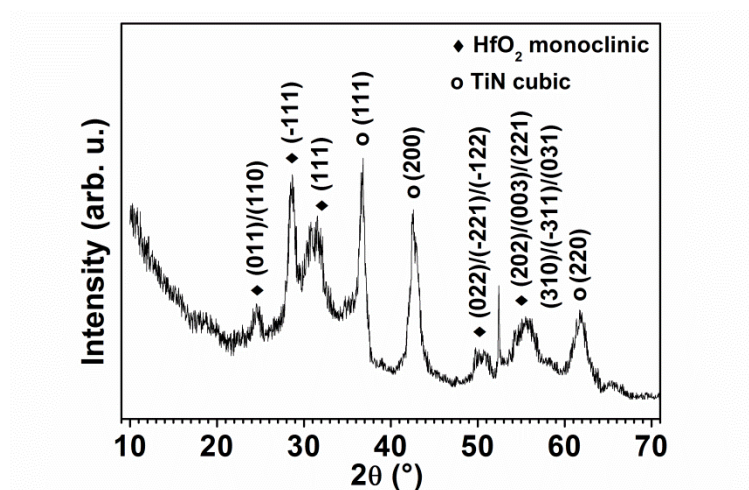


Figure 4.6: GIXRD measurement of Sample C taken with 1° angle of incidence.

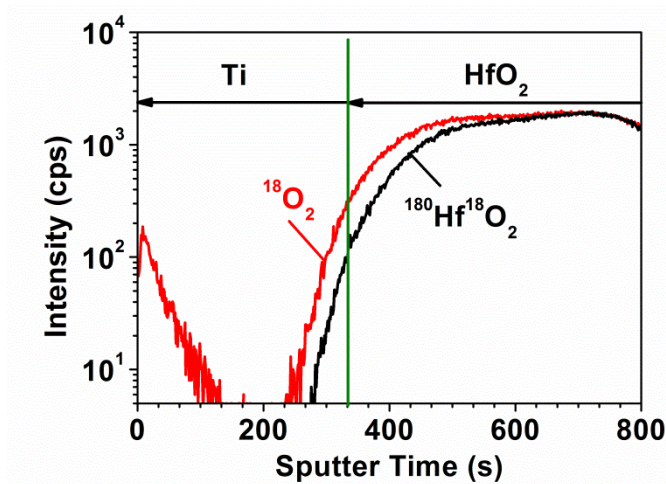


Figure 4.7: ToF-SIMS depth profile of the $^{18}\text{O}_2$ isotope and $^{180}\text{Hf}^{18}\text{O}_2$ across the Ti and HfO_2 films of Sample C.

SIMS study. Firstly, the $^{18}\text{O}_2$ isotope ToF-SIMS depth profile of Sample C (Figure 4.7) shows the uniformity of the HfO_2 layer deposited at MBE. Besides, in comparison to the results presented in Figure 4.4 there is no pronounced accumulation of the $^{18}\text{O}_2$ at the Ti/m- HfO_2 interface. Only a very slight gradual decrease of the $^{18}\text{O}_2$ signal, from the bottom towards the top part of the HfO_2 film (from about 700 s to 400 s), is observed. Moreover, the oxygen signal presents an abrupt drop by going from the HfO_2 film towards the Ti film (from about 400 s to 200 s) indicating that oxygen diffusion is limited to the first metallic interface layers only.

Next, the impact of oxygen diffusion on Ti oxidation states was studied non-destructively by HAXPES. The Ti 2p HAXPES spectra taken at value of α at 40° (Figure 4.8(a)) and 83° (Figure 4.8(b)) at 8 keV excitation energy were fitted with the same parameters as the spectra in Figure 4.5. Five different Ti oxidation states were distinguished in both spectra. However, on contrary to the sample with a- HfO_2 , besides components attributed to the Ti oxide forms, also a strong metallic Ti peak (Ti^0) is visible. This result confirms the lower Ti oxidation at the interface with a monoclinic than with an amorphous HfO_2 , as deduced from ToF-SIMS data.

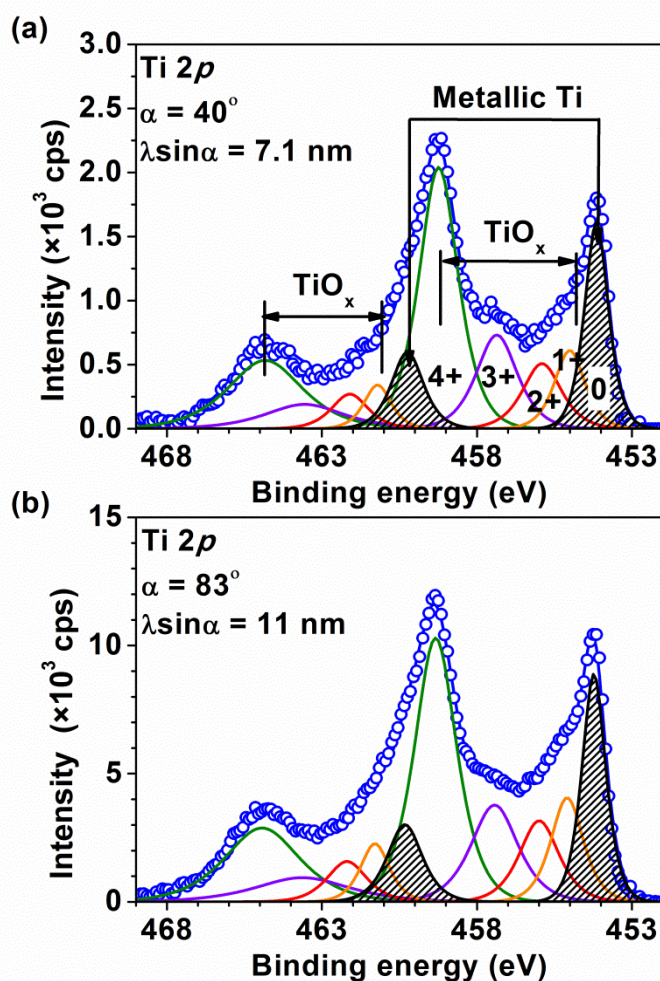


Figure 4.8: Ti 2p HAXPES spectra of Sample C taken with excitation energy of 8 keV and at α of (a) 40° and (b) 83° .

4.1.3 Oxygen vacancy formation energy in HfO_2

The experimental results indicate that the HfO_2 morphology substantially controls the Ti/ HfO_2 interface chemical reactivity. Thus, in order to obtain a microscopic insight into the experimental results, with courtesy from Jordi Suñe and José Cartoixa (both at university of Barcelona), first-principle calculations of charged oxygen vacancy formation energies in the m- HfO_2 and a- HfO_2 phase were performed using the SIESTA package.⁽⁹⁹⁾

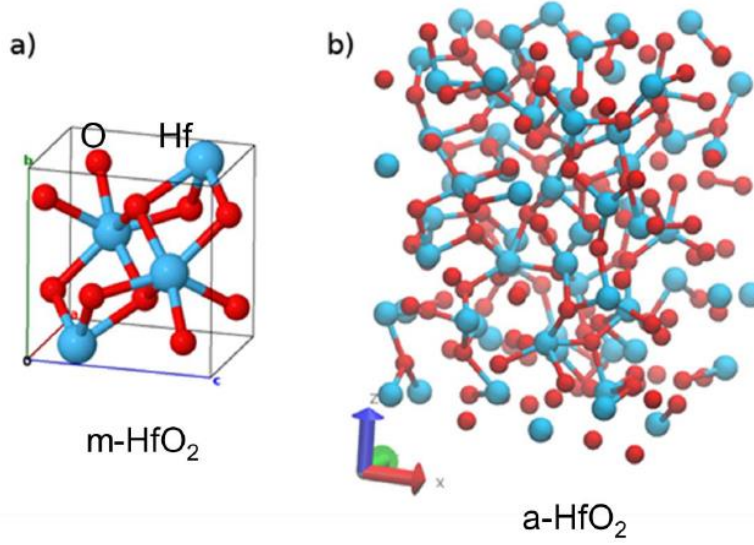


Figure 4.9: Ball-and-stick plots of the simulated (a) monoclinic (primitive cell) and (b) amorphous HfO_2 .

This code implements the Density Functional Theory (DFT) in its Generalized Gradient Approximation (GGA), using the parametrization for the exchange-correlation energy by Perdew-Burke-Ernzerhof.⁽¹⁰⁰⁾ The used norm-conserving pseudopotentials for the core electrons and a single- ζ plus polarization (SZP) basis set for the valence electrons give a good compromise between the accuracy — the obtained lattice parameters for m- HfO_2 – Figure 4.9(a) – are 5.149, 5.185, and 5.296 Å (5.117, 5.175, and 5.291 Å experimentally^{(101), (102)}) — and the computational cost. The a- HfO_2 structure, containing 201 atoms [cf. Figure 4.9(b)], has been generated by a melt/quench cycle with the GULP molecular dynamics program,^{(103), (104)} followed by a structural relaxation with SIESTA until the force on each atom was less than 0.04 eV/Å.

The formation energies of (charged) vacancies, $\Delta E_{form}^{V,q}$, are computed as differences in the total energies between the configuration with the oxygen removed and going to the molecular phase (reference chemical potential), with the electrons going to (coming from) the Fermi level, and the pristine state:

$$\Delta E_{form}^{V,q} = E^{V,q} - E^{pristine} + \frac{1}{2}\mu_{O_2} + q(\varepsilon_{TVB} + \mu_F), \quad (4.2)$$

where $E^{V,q}$ is the energy of the system with a vacancy with charge q , $E^{pristine}$ is the energy of the system without the vacancy, μ_{O_2} is the energy of molecular oxygen and μ_F is the position of the Fermi level with respect to the top of the valence band, ε_{TVB} . Spurious contributions to the total energy in systems with a net charge arising from the use of periodic boundary conditions are removed by the Makov-Payne⁽¹⁰⁵⁾ procedure, which have been properly accounted for the use of non-cubic cells and possibly anisotropic/tensor dielectric constants, as described in Ref. (106).

Table 4.1 shows the oxygen vacancy formation energies for different charge states (Eq. 4.2), for the threefold coordinated O in m-HfO₂ and the three different oxygen positions in the a-HfO₂ structure. In accordance with previous calculations,⁽¹⁰⁷⁾ the vacancy is slightly less costly to create in the amorphous case, which is to be expected given the metastability of the amorphous structure. Also in accordance with previous theoretical results,⁽¹⁰⁸⁾ the +2 charge state vacancy is strongly favored at low Fermi levels.

Moreover, results shown in Table 4.1 indicate that in amorphous structures the formation of charged vacancies is energetically favored with respect to both (1) its crystalline counterpart, and (2) its neutral equivalent, in agreement with the experimental results. In some cases the charge vacancy formation energy is negative, implying a thermodynamically favored process. When looking at the intermediate steps for the structural relaxation, it is observed that, in some cases for charged vacancies, heavy restructuration took place after removal of the

Table 4.1: Oxygen vacancy formation energies, with the Fermi level at the top of the valence band, for the threefold oxygen in monoclinic HfO₂ and oxygen at three different positions (at random) in an amorphous HfO₂ host.

Vacancy charge	O Vacancy formation energy (eV)			
	m-HfO ₂	O(1) a-HfO ₂	O(2) a-HfO ₂	O(3) a-HfO ₂
0	7.94	7.26	7.48	6.61
+1	5.92	7.25	1.69	-0.63
+2	4.04	-2.74	2.45	3.91

oxygen atom. It is believed that this observation can be responsible for the dramatic decrease in formation energies for those cases (i.e. the final state has a much reduced total energy due to the large atomic rearrangement).

4.1.4 *Off-line* characterization

Now, the results collected for the BEOL-processed Sample D will be presented. The as-deposited Ti/HfO₂/TiN stack was characterized by X-ray reflectivity (XRR) and scanning transmission electron microscopy (STEM) with energy-dispersive X-ray spectroscopy (EDX). Results of both experiments are shown in Figure 4.10. The left panel presents a high angle annular dark field (HAADF) STEM image with marked thicknesses of the layers extracted from the XRR measurement (data not shown). Thanks to the HAADF STEM image contrast dependence on the atomic number (Z-contrast), one can easily distinguish

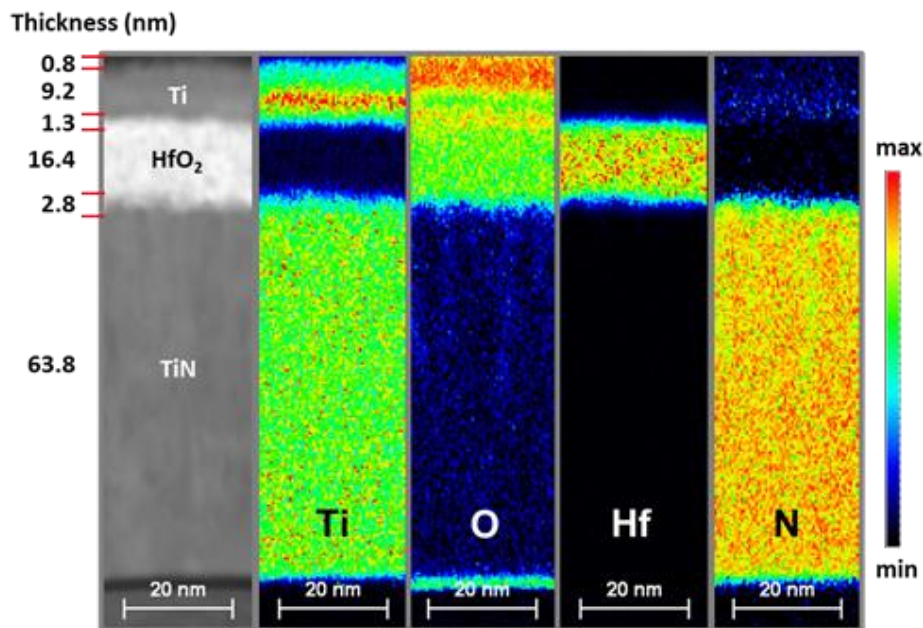


Figure 4.10: High angle annular dark field STEM with EDX image of the as-deposited Sample D. Thicknesses of all layers, given on the left, were determined by XRR.

between the individual layers of Sample D. Clearly, the Ti, HfO₂ and TiN layers, as well as the Ti surface oxidation and the interface layers between the HfO₂ film and both electrodes, are visible.

Next, more detailed element distribution within Sample D was extracted from the EDX maps. In Figure 4.10 on the right side from the HAADF STEM panel there are shown the Ti, O, Hf and N EDX maps. If one compares all these maps, can notice that the HfO₂ film is homogenous and there is no Hf diffusion inside the Ti or TiN layers. Besides, these results indicate the presence of some Ti and N atoms inside the HfO₂ layer. Both can be an artifact effect due to the destructive nature of this technique. However, N as well as other impurities, such like C or H atoms may originate in the HfO₂ film from the deposition technique due to the used organic precursor.^{(91), (92)} Moreover, the Ti layer seems to contain a significant concentration of O, mostly at the top and bottom part of the layer and less of N atoms. Thus, the O concentration is increased at each interface of Sample D.

Therefore, although the combined STEM-EDX study is a destructive technique, it allows to deduce the same conclusions as from the non-destructive studies performed on the MBE-processed samples. Namely, the presence of a TiO_x surface oxidation layer and the interface layer between a-HfO₂ and the Ti top electrode.

4.1.5 Summary and conclusions

The Ti/HfO₂ interface chemistry was investigated by advanced materials science characterization studies. The *in-situ* XPS monitoring of the Ti growth on an amorphous HfO₂ substrate at the MBE facility have revealed the formation of Ti oxides in the initial state of growth. A good agreement between experimental and fitting results has indicated that the Ti deposition at HfO₂ by MBE corresponds to the Volmer-Weber growth mode. In detail, Ti atoms are initially bounded to the HfO₂ substrate, and Ti oxide islands nucleate and expand three dimensionally in all directions. Next, the islands become more and more metallic, coalesce and

form a closed layer after about 35 s of deposition and then follow a 2D growth (layer by layer) mode.

In the next step, the origin of the Ti oxidation was investigated by combined GIXRD, ToF-SIMS and HAXPES studies. Additionally, the impact of the HfO₂ crystalline structure on the Ti oxidation degree was verified. For this purpose, the HfO₂ films were prepared with ¹⁸O isotope atoms. The RT deposited HfO₂ film was X-ray amorphous containing only minor monoclinic nanocrystallites, while the deposited HfO₂ film at 400 °C was monoclinic. Both the ¹⁸O₂ ToF-SIMS depth profiles and the Ti 2*p* HAXPES spectra have revealed that for both samples the as-deposited Ti layer is oxidized at the interface by the ¹⁸O₂ coming from the HfO₂ film. Moreover, a much more pronounced Ti oxidation was found in case of Ti deposited on the amorphous than on the monoclinic HfO₂ film.

Next, the first-principle calculations of the charged oxygen vacancy formation energies in the monoclinic and amorphous phase of HfO₂ were performed. The lower formation energy was found to form stable oxygen vacancies in case of the amorphous than in case of the monoclinic HfO₂ films and thus confirms the experimentally observed enhanced Ti oxidation activity with respect to a-HfO₂ films.

Finally, the as-deposited Ti/HfO₂/TiN stack processed under BEOL conditions was characterized by XRR and EDX. As in case of MBE-processed samples, a thick (around 1.3 nm) TiO_x interface layer between Ti and a-HfO₂ has been found. Moreover, EDX maps indicated the presence of impurities (C, N) in HfO₂, characteristic for samples processed under BEOL conditions.

In conclusion, the *in-situ* and *ex-situ* studies of the Ti/HfO₂/TiN stacks processed at MBE give the same result as the *off-line* characterization studies of the BEOL-AVD processed samples. Namely, the presence of a TiO_x interface layer between the Ti and HfO₂ films. Moreover, it is found that the HfO₂ crystalline structure impacts its chemical reactivity with Ti and thus the oxygen vacancy concentration inside the HfO₂ film. Besides, not only oxygen vacancies but also other defects, such like C or N impurities may change the HfO₂ insulating properties. Therefore,

the control of the parameters used during the sample preparation turns out as important approach to engineer the reactivity of the Ti/HfO₂ interface in order to create the initial amount of defects for reproducible and reliable resistive switching performance.

4.2 *Ex-situ* electroforming study of Ti/HfO₂/TiN cells

The resistive switching properties of the BEOL-processed Ti/a-HfO₂/TiN samples were further investigated in details. In this section the as-deposited and the electroformed sample were investigated *ex-situ* by HAXPES. *Ex-situ* term means that the MIM stack was electroformed outside the HAXPES chamber.

4.2.1 Electrical characterization

I-V characteristic of the **initial electroforming process** of Sample E is presented in Figure 4.11(a). This process was performed under ambient conditions by applying a positive direct current (DC) sweep voltage across the stack from 0 V to 15 V, with a current compliance (CC) set at 10 mA. In the result of this electroforming, the initial resistance of Sample E has changed by about three orders of magnitude. In detail, the resistance ratio between the as-deposited-state and the electroformed state of Sample E, read at 0.2 V, was equal to 2×10^3 . The subsequently applied DC sweep voltage from -3 V to 6 V with CC = 80 mA (Figure 4.11(b)) has revealed that the electroforming process has initiated a

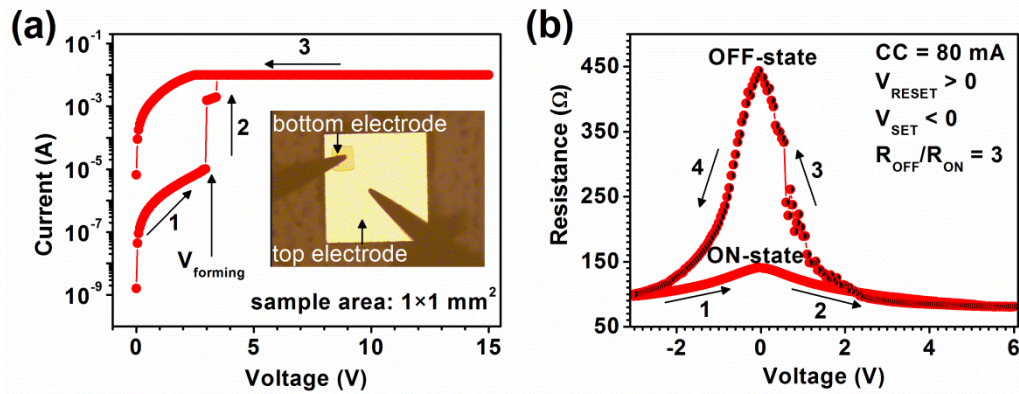


Figure 4.11: (a) *I-V* characteristic of the initial electroforming process applied to the as-deposited Sample E (sweep rate 0.05 V/s). Inset shows a top view of the sample with the bottom and top electrode contacts. (b) *R-V* characteristic of the electroformed sample presenting a bipolar resistive switching.

clockwise bipolar resistive switching behaviour in Sample E. In detail, for the switching operation from the ON- to the OFF-state, a positive reset voltage was required, whereas a negative voltage was needed to set sample from the OFF- to the ON-state. The resistance ratio between the OFF- and the ON-state ($R_{\text{OFF}}/R_{\text{ON}}$) after electroforming, read at 0.2 V, was equal to 3.

4.2.2 HAXPES characterization

The electroformed Sample E, prepared from the same wafer as the as-deposited Sample D, were then analyzed by HAXPES in order to investigate whether the electroforming process have changed also material properties of Sample E.

Chemical modifications

The most prominent chemical changes between both samples occurred in the Ti photoemission spectra. Figure 4.12 shows the Ti 2s HAXPES spectra of the as-deposited (top) and the electroformed (bottom) samples collected at the two excitation energies of 5.5 keV (left) and 7 keV (right). All these spectra were modeled with three components attributed to the metallic titanium (Ti), titanium suboxides (TiO_x) and titanium dioxide (TiO_2) with Gaussian-Lorentzian (for TiO_x and TiO_2) and Doniach-Sunjjic (for Ti) line shapes. The full width at half maximum of each component and the distance between the components were fixed for the fitting. Only the position and the intensity of the peak might thus change. The results of the fitted as-deposited Sample D spectra, presented in Figure 4.12(a) and 4.12(b), confirm the two qualitative information given by the destructive STEM with EDX and the XRR techniques shown in Figure 4.10: (1) **the titanium surface oxidation** - attributed mainly to the existence of the TiO_2 component due to the higher intensity for both excitation energies than TiO_x , and (2) **the existence of the interface layer** between the Ti and HfO_2 films – attributed to the TiO_x and the TiO_2 increase by the increase of the information

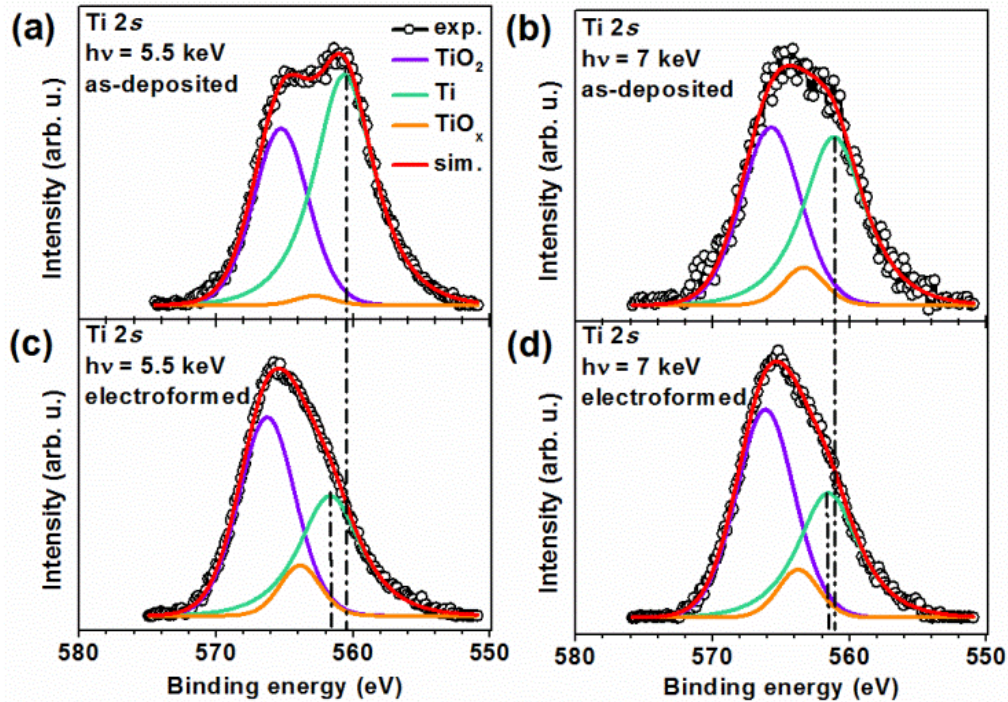


Figure 4.12: Ti 2s HAXPES spectra of the as-deposited Sample D (top) and electroformed Sample E (bottom) taken with 5.5 keV (left) and 7 keV (right) excitation energy. All spectra are normalized and modeled with three components. Dash-dotted lines highlight the changes in the peak position between the as-deposited and electroformed samples.

depth. Moreover, this result is in agreement with the HAXPES results (Figure 4.8) collected for the MBE-processed as-deposited samples. Besides, comparing the top with the bottom HAXPES spectra in Figure 4.12, one can see that the electroforming process has drastically changed the Ti 2s line shape. A decrease of the metallic Ti and an increase of the TiO₂ and TiO_x peaks after electroforming process indicate an **enhanced Ti oxidation at the Ti/a-HfO₂ interface**.

To highlight these changes, the ratio between the metallic titanium to the total titanium oxides intensity (TiO_x + TiO₂) was calculated, and is further denoted as Ti/TiO_y. For the as-deposited sample, the Ti/TiO_y ratio decreased from 1.5 ± 0.1 to 0.9 ± 0.1 when the excitation energy increased from 5.5 to 7 keV. The smaller Ti/TiO_y ratio in case of higher excitation energy (7 keV) demonstrates that the

HAXPES is indeed sensitive to the Ti/HfO₂ interface, important for the switching mechanism. After electroforming, an enhanced Ti/HfO₂ interface oxidation is observed, resulting in an even smaller Ti/TiO_y ratio of 0.6 ± 0.1 at 7 keV. Interestingly, only minor differences in the Ti 2s peak shape were observed for the electroformed Sample E spectra recorded at these two photon energies: for both cases, the Ti/TiO_y ratio is equal to 0.6 ± 0.1 . This can indicate a creation of a more homogeneous system during the electroforming step with an oxygen migration from HfO₂ into the Ti layer. In addition, it is also noticed that the simulation of the Ti 2p HAXPES spectra (not shown) corroborates the same results presented here for the less complex Ti 2s line.

Due to the higher sensitivity of 7 keV of excitation energy to the important Ti/HfO₂ interface, the next HAXPES results on the other photoelectron lines will be presented only for this energy.

Electronic modifications

Besides the chemical changes, also electronic modifications appeared in the HAXPES spectra between both samples. The photoelectron peak positions in the HAXPES spectra of the electroformed Sample E (marked with vertical dash-dotted lines in Figure 4.12, Figure 4.13(a) and Figure 4.13(b)) are shifted towards

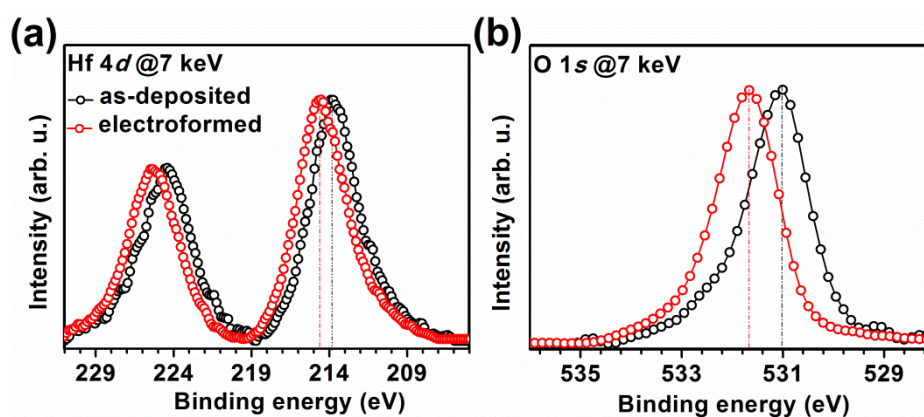


Figure 4.13: Normalized and smoothed Hf 4d (a) and O 1s (b) HAXPES spectra of the as-deposited and electroformed samples recorded at excitation energy of 7 keV. Dash-dotted lines highlight the peak positions.

Table 4.2: Experimental peak shifts ($\Delta BE = BE^{\text{electroformed}} - BE^{\text{as-deposited}}$) between the electroformed and as-deposited samples, for metallic Ti 2s, Hf 4d_{5/2} and O 1s lines, recorded with excitation energy of 7 keV.

	Peak		
	Ti 2s	Hf 4d _{5/2}	O 1s
$\Delta BE \pm 0.05$ (eV)	0.4	0.8	0.7

larger binding energy with respect to the peak positions of the as-deposited Sample D. The binding energy difference between both samples (ΔBE) calculated for the metallic Ti 2s, Hf 4d_{5/2} and O 1s photoemission lines, collected at 7 keV of excitation energy, is shown in Table 4.2. Since the peak shift values upon the electroforming process for Hf 4d (0.8 eV) and O 1s (0.7 eV) are almost the same and higher than that for Ti 2s (0.4 eV), it is assumed that the oxygen signal in the electroformed sample HAXPES spectra arises mainly from the HfO₂ region. Moreover, because ΔBE values for these three components are different, a charging of the electroformed sample during the measurement or an interface dipole creation can be thus excluded as a reason of these shifts.⁽¹⁰⁹⁾

Other chemical modifications

In order to identify whether the chemical changes occurred also in the Hf 4d and O1s HAXPES lines after the electroforming process, the binding energy shifts visible in Figure 4.13(a) and 4.13(b) were corrected and overlapped peaks are shown in Figure 4.14(a) and Figure 4.14(b). It can be seen, that no clear peak shape change is visible in the Hf 4d HAXPES line (Figure 4.14(a)). However, a small change appears in the O 1s HAXPES spectra, highlighted in the inset of Figure 4.14(b). A small subpeak located there around 532.5 eV decreases going from the as-deposited to the electroformed sample. This subpeak can be attributed to the more covalently bonded, probably defect-related oxygen entities in the HfO₂ film. It was previously reported that such species are termed “non-lattice

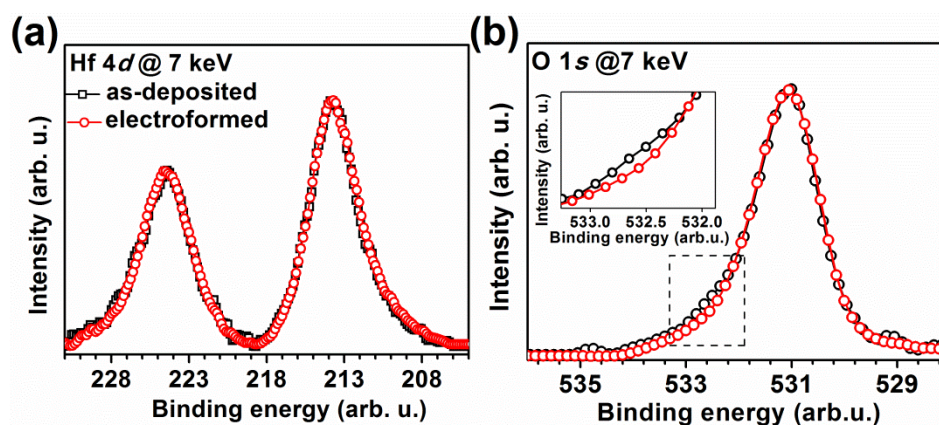


Figure 4.14: Normalized and smoothed Hf 4d (a) and O 1s (b) HAXPES spectra of the as-deposited and electroformed samples recorded at excitation energy of 7 keV. The peak shift is removed. Inset in Fig. 4.14(b) shows the region corresponding to the covalently bonded, probably defect-related oxygen entities in the HfO₂ film.

oxygen”⁽¹¹⁰⁾, and are prone to move in the oxide layer with lower activation energy during the electroforming.⁽¹¹¹⁾ Hence, they can leave oxygen vacancies in the oxide layer behind.

4.2.3 Proposed electroforming model

Possible chemical (top) and electronic (bottom) modifications between the as-deposited (left) and electroformed (right) Ti/HfO₂/TiN samples are proposed in Figure 4.15.

In general, the binding energy in HAXPES spectra is referenced to the Fermi level (E_F). Any change of dopants concentration in the film changes the barrier height (Φ_b) and thus the calculated binding energy in the HAXPES spectra. In order to explain the observed peak shifts in the HAXPES spectra between the as-deposited Sample D and electroformed Sample E the band diagrams are drawn in Figure 4.15 at equilibrium⁽¹¹²⁾ (i.e. Fermi levels of both samples are equal). Knowing the higher work function of the TiN bottom electrode ($\Phi^{TiN} = 4.7$ eV)⁽¹²⁾ compared to the Ti top electrode ($\Phi^{Ti} = 4.2$ eV)⁽¹¹³⁾, and that the barrier height for the top

injection is lower than the barrier height for the bottom injection⁽¹¹⁴⁾, the band diagram of the as-deposited sample is drawn with a downward band bending towards the Ti top electrode.⁽¹¹²⁾ The calculated binding energy in the HAXPES spectra of the electroformed sample – here exemplified for valence band (VB) maximum photoelectrons by the energy difference between E_F and the VB maximum – will be larger than the binding energy of the as-deposited sample only

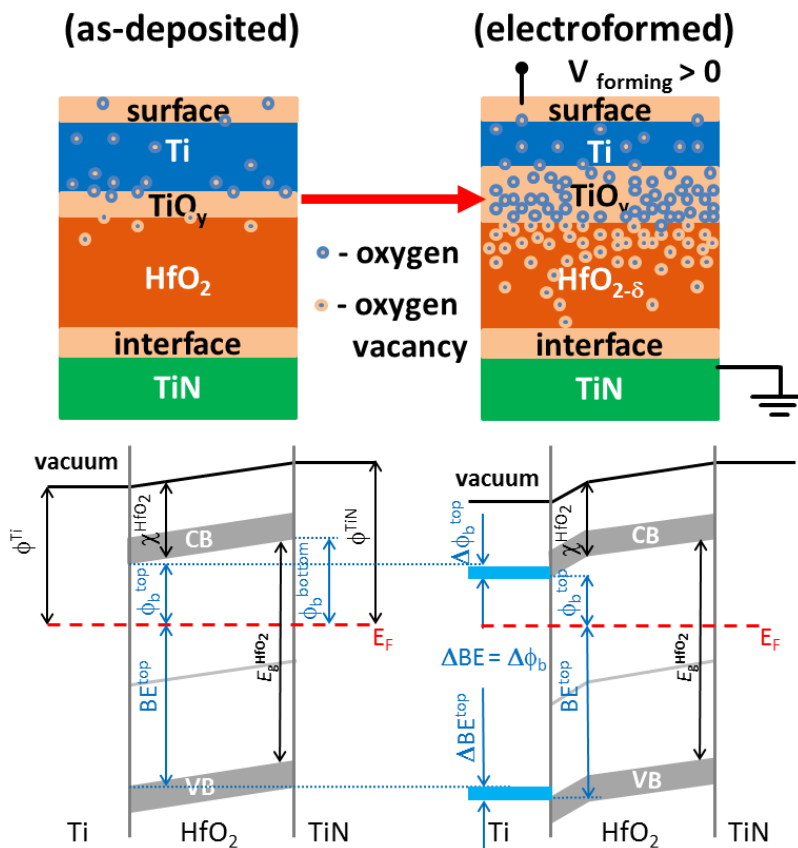


Figure 4.15: Proposed chemical (top) and electronic (bottom) modifications of the Ti/HfO₂ interface between the as-prepared (left) and electroformed (right) samples. An increase of the *n*-type oxygen vacancy defects at the Ti/HfO₂ interface during the electroforming process increases the downward band bending, thereby increasing the sample conductivity. (Φ_b - barrier height, Φ - work function, BE - binding energy, E_g - band gap, CB - conduction band, VB - valence band, χ - electron affinity).

in case when the Φ_b of the HfO₂ at the interface with Ti will be reduced. In other words, this situation occurs when the downward band bending at the Ti/HfO₂ interface will be increased, confirming at the same time a higher conductivity of the electroformed sample. This condition will be only fulfilled when there is an increase of the *n*-type defects concentration at the Ti/HfO₂ interface in the HfO₂ film.

An increase of the Ti oxidation suggests that oxygen vacancies are created inside the HfO₂ film during the electroforming process. Indeed, the oxygen vacancies in the HfO₂ films are known as stable *n*-type defects.^{(46), (115)} Their formation was also predicted by theory.^{(108), (113)} Moreover, the *n*-type doped complex perovskite dielectric-based RRAMs^{(45), (55), (116), (117)} present the same clockwise bipolar resistive switching as the electroformed Sample E (Figure 4.11(b)).

Therefore, assuming that there is an increase of the *n*-type oxygen vacancies at the Ti/HfO₂ interface by a Ti interface oxidation during the electroforming, the downward band bending (present already in case of the as-deposited sample) is further increased in the energy band diagram of the electroformed sample. Furthermore, this assumption is also supported by the observed peaks shifts towards higher binding energy in the HAXPES spectra^{(79), (118)} of the electroformed sample.

4.2.4 Summary and conclusions

The electroforming process performed under ambient conditions on the 1 × 1 mm² as-deposited Ti/a-HfO₂/TiN stack has changed its resistance by three orders of magnitude. The subsequently applied DC sweep voltage has revealed a clockwise bipolar resistive switching behavior in this sample. Next, the as-deposited and the electroformed samples were investigated by HAXPES. This non-destructive studies performed at the 3rd generation synchrotron in Hamburg⁽⁹⁵⁾ have underlined chemical and electronic changes at the Ti/HfO₂ interface between both samples. A detailed analysis has shown an increase of the

Ti oxide components and an increase of the binding energy values in the HAXPES spectra collected for the electroformed sample, in comparison to the as-deposited sample spectra.

It can be concluded that a positive voltage applied to the as-deposited Ti/a-HfO₂/TiN stack during the electroforming process results in an oxygen migration from the HfO₂ film towards the Ti top electrode. The Ti oxidation at the Ti/a-HfO₂ interface is thus enhanced and the interface layer, present already in the as-deposited stack, broadened. In consequence, the removed oxygen atoms from the HfO₂ layer leave oxygen vacancies behind, which act as *n*-type dopants. In consequence of the *n*-type dopants density increases, the barrier height at the top interface decreases and calculated binding energies in the electroformed sample HAXPES spectra thus increased.

4.3 *In-operando* electroforming of Ti/HfO₂/TiN

In order to investigate one and the same sample without having it to expose to ambient conditions (thereby avoiding possible chemical modifications) and suffering from data interpretation ambiguities (e.g. thickness inhomogeneity of two samples) the Ti/a-HfO₂/TiN samples were investigated by *in-operando* HAXPES. In this chapter, the impact of the current compliance and DC sweep voltage parameters on the resistive switching behavior and the material changes in the Ti/a-HfO₂/TiN cells will be presented.

4.3.1 Electroforming at low electrical power

Electrical characterization

The low-power dissipation RRAMs are of major application interest for eNVMs, e.g. for WSN applications. Therefore, the first *in-operando* HAXPES studies were focused on the electroforming of the Ti/a-HfO₂/TiN cell with the smallest possible current compliance and DC sweep voltage parameters. During searching for the parameters which electroform Sample F, the current compliance and DC sweep voltage were gradually increased. When the current compliance was increased to

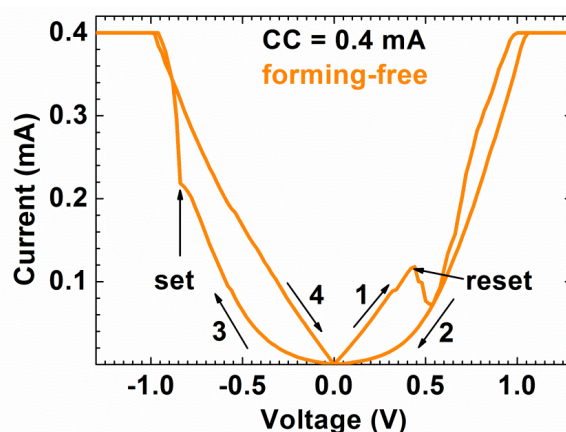


Figure 4.16: *I-V* characteristic of Sample F showing resistive switching at low power conditions.

0.4 mA and the voltage was swept between -1.3 V and +1.3 V, the first reset and set processes were visible in the I - V characteristic. The corresponding clockwise ($V_{\text{reset}} > 0$ and $V_{\text{set}} < 0$) bipolar resistive switching characteristic is shown in Figure 4.16. It should be noted that no initial electroforming process was necessary to establish the resistive switching behaviour in Sample F. The $R_{\text{OFF}}/R_{\text{ON}}$ ratio, read at 0.1 V, was equal to 10. However, subsequently applied DC sweep voltage parameters with same current compliance values have revealed an unstable resistive switching behaviour of Sample F. Namely, it was not always possible to set or reset this sample again.

HAXPES characterization

The collected Ti $2p$ and Hf $4d$ HAXPES spectra of the as-deposited-, and the first OFF- and ON-states of Sample F are shown in Figure 4.17. All spectra presented here were recorded with 7 keV of excitation energy at an electron take-off angle of 80° , thus at the most Ti/HfO₂ interface-sensitive take-off angle used during these investigations. In both regions, there are no significant differences between spectra collected for the three investigated resistive states of Sample F. The same observation can be found in the HAXPES spectra collected for the same resistive

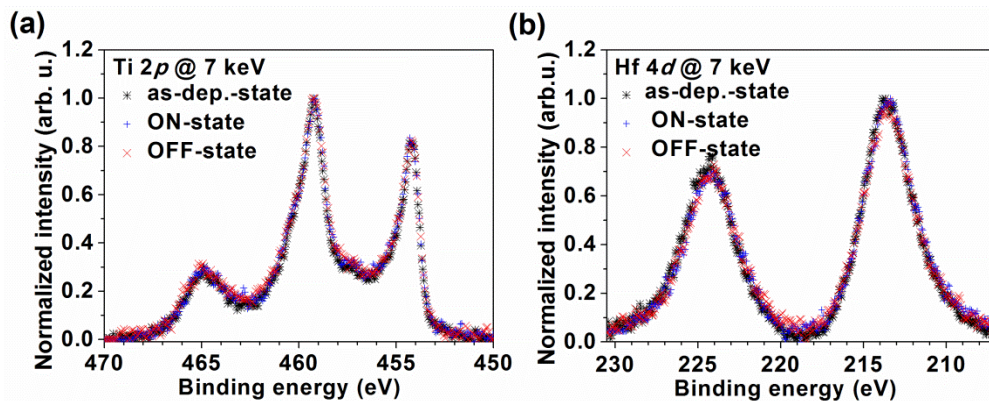


Figure 4.17: Ti $2p$ (a) and Hf $4d$ (b) HAXPES spectra of Sample F in the as-deposited-, ON- and OFF-states, recorded at excitation energy of 7 keV and an electron take-off angle of 80° .

states of Sample F at the two other, less sensitive to the Ti/HfO₂ interface, take-off angles (for $\alpha = 45^\circ$ and 65° HAXPES results are not shown). These results are opposite to the HAXPES peak shifts and to the increase of the Ti top electrode oxidation observed in the HAXPES spectra collected for the as-deposited Sample D and the electroformed under ambient conditions (with higher current compliance and sweep voltage parameters) Sample E.

It can be thus concluded that for low electrical power applied to the Ti/a-HfO₂/TiN cell, forming-free resistive switching behaviour is observed. However, it is unstable and materials changes - which might occur at the Ti/HfO₂ interface region - are below the HAXPES detection sensitivity.

4.3.2 Electroforming with increasing electrical power

Next, the impact of the higher current compliance and DC sweep voltage parameters used during the Ti/HfO₂/TiN cell operation on its resistive switching behaviour and materials changes was investigated by in-operando HAXPES.

Electrical characterization

For this purpose, Sample G was electrically stressed by increasing step by step the current compliance and DC sweep voltage values. The first clockwise bipolar resistive switching characteristic, presented in Figure 4.18(a), appeared when the current compliance was increased to 6 mA and the voltage was swept between -2.4 V and +2.7 V. However, as in the case of Sample F, this resistive switching phenomenon was unstable and the current compliance and DC sweep voltage had to be further increased. When the current compliance was equal to 20 mA and the voltage was swept between -3.5 V and 3.5 V, the step-like current increases around 1.9 V, 2.1 V and 2.3 V were observed in the I - V characteristic (Figure 4.18(b)). In order to reset the device to the OFF- state, the current compliance had to be further increased to 30 mA, while the same sweep voltage was applied. As shown in Figure 4.18(c), the reset process occurred at a positive voltage polarity.

After that, Sample G showed a stable clockwise bipolar resistive switching with a $R_{\text{OFF}}/R_{\text{ON}}$ ratio, read at 0.1 V, equal to 11.

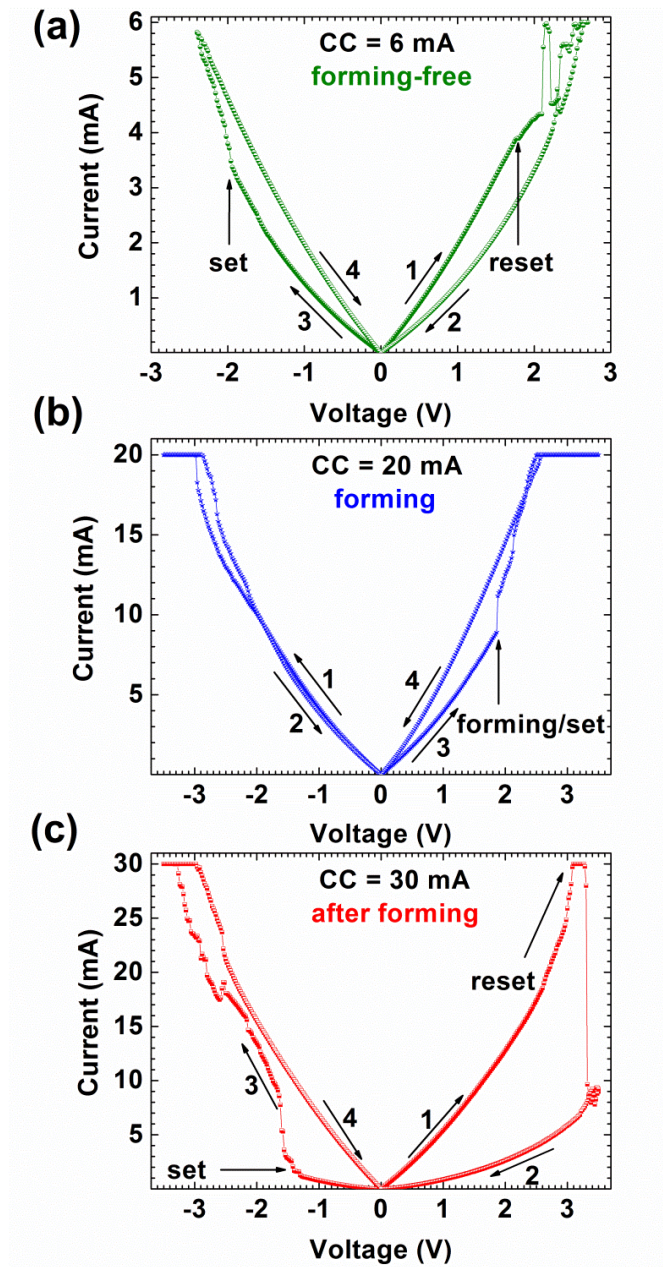


Figure 4.18: I - V characteristics showing resistive switching behavior of Sample G at increasing current compliance (6 mA (a), 20 mA (b) and 30 mA (c)) and DC sweep voltage parameters.

HAXPES characterization

Figure 4.19 shows the Ti $2p$ HAXPES spectra recorded for the as-deposited- and three ON-states (CC = 6, 20 and 30 mA) of Sample G. First, by fitting the theory to the as-deposited-state spectrum, 5 doublet components, attributed to the different Ti oxidation states (0 to +4), were used. Next, the same parameters and full width at half maxima (FWHM ± 0.1 eV) were used to fit the three remaining spectra. Only the peak positions and their intensity could thus change. The results of this fitting allowed to calculate the metallic Ti (Ti^0) to the sum of Ti oxides

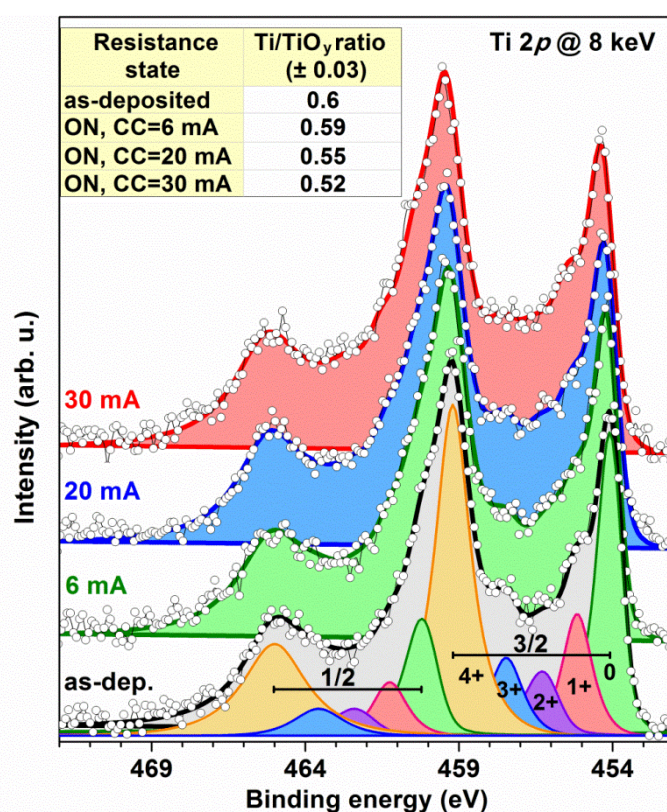


Figure 4.19: Ti $2p$ HAXPES spectra of Sample G in different resistive states: as-deposited-, and three ON-states (CC = 6, 20 and 30 mA) taken at 8 keV of excitation energy at normal emission geometry. Spectra are fitted with five doublet components attributed to the different oxidation states of Ti ($\text{Ti}^0 - \text{Ti}^{4+}$). The dots correspond to the experimental points and the lines to the result of the fitting. Inset presents the metallic Ti (Ti^0) to the total Ti oxides ($\text{Ti}^{1+} - \text{Ti}^{4+}$) ratio (Ti/TiO_y).

($\text{Ti}^{1+} - \text{Ti}^{4+}$) ratio – Ti/TiO_y . The calculated values are summarized in a table shown in the inset of Figure 4.19. A clear monotonous decrease of the Ti/TiO_y ratio from 0.60 (as-deposited-state) to 0.52 (ON-state 30 mA) is observed. This result indicates that by increasing the current compliance and DC sweep voltage values during the forming/set process, a Ti/HfO_2 interface oxidation occurs and is oxidized and in consequence the oxygen vacancies concentration in HfO_2 increases. In consequence, the Φ_b at the top interface decreases and the calculated binding energy of the peaks in the HAXPES spectra increases. It is noted that insulator towards metal transition as a function of increasing oxygen vacancies concentration in HfO_{2-x} thin films has been studied in detail by Hildebrandt *et al.* (119).

An increased oxygen vacancies concentration in the HfO_2 film at the interface with Ti should also increase the calculated binding energy of hafnium photoemission lines in HAXPES spectra. The oxygen vacancy concentration in the different resistive states of Sample G was thus verified by checking the binding energy of HfO_2 in the O 1s and Hf 4f regions. Figure 4.20(a) shows the O 1s photoemission line recorded for the as-deposited-state and three ON-states of Sample G. All spectra were fitted with three Gaussian-Lorentzian line shape components attributed to the Ti oxides (O-Ti, 530.9 eV), hafnium oxides (O-Hf, 531.8 eV) and carbon oxides (O-C, 532.6 eV). The binding energy of the hafnium oxide component (O-Hf), marked in Figure 4.20(a) by the white-dashed line, increases when the current compliance increases. The binding energy values and the calculated peak shifts of both components are shown in Figure 4.20(b). As can be seen, both photoemission lines shift in the same direction, however with different values. Thus, the observed binding energy increase allows to conclude that an increased positive space charge region at the Ti/HfO_2 interface related to the oxygen vacancies is created, accordingly with the increase of the applied electrical power to Sample G.

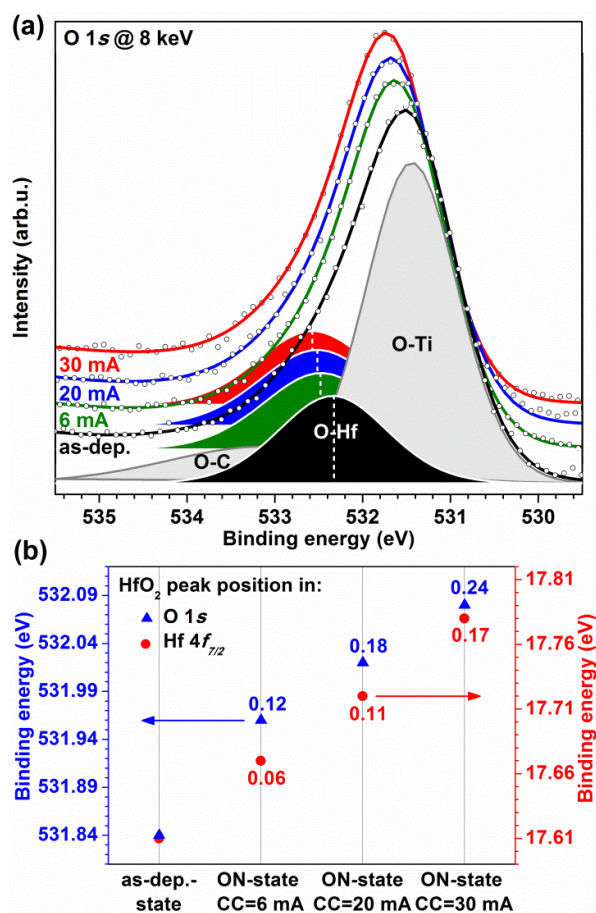


Figure 4.20: (a) O 1s HAXPES spectra of Sample G in different resistive states: as-deposited-, and three ON-states (CC = 6, 20 and 30 mA) collected at 8 keV excitation energy at normal emission geometry. All spectra are fitted with three components attributed to the Ti oxides (O-Ti, 530.9 eV), hafnium oxides (O-Hf, 531.8 eV) and carbon oxides (O-C, 532.6 eV) features. The white dashed lines mark the O-Hf binding energy. (b) Binding energy of hafnium oxide peaks in the O 1s (blue triangles) and the Hf 4f_{7/2} (red circles) regions. The values indicate peak shifts compared to the as-deposited-state peak position.

Besides, the HAXPES data indicate that the applied electrical power to Sample G does not only affect the Ti 2p, Hf 4f and O 1s photoemission lines but also the C 1s, as observed in the part of the survey scan spectra presented in Figure 4.21(a). After the survey scan spectra normalization to the Hf 4d peak intensity, it is

clearly observed that the C 1s peak intensity increases with the increase of the electrical stress applied to the sample. Initially, for the lower current compliance and DC sweep voltage parameters this ratio does not change significantly. However, after sample is electroformed and shows a stable resistive switching behavior, the C 1s to the Hf 4d intensity ratio (I_C/I_{Hf} shown in Figure 4.21(a)) increases from 0.4 (as-deposited-state) to 0.6 (ON-state 30 mA). The C 1s spectra of the as-deposited- and the ON-state CC = 30 mA of Sample G (Figure 4.21(b)) are fitted by four components assigned to the -C-C (285.5 eV), -C-O (286.5 eV), >C=O (287.5 eV) and O-COO (289.7 eV) chemical bonds. This fitting allows to detect the chemical changes within the carbon: (1) the concentration and (2) the chemical environment of carbon located at the Ti/HfO₂ interface change. A significant increase of carbon oxide species (here mainly >C=O) after setting the

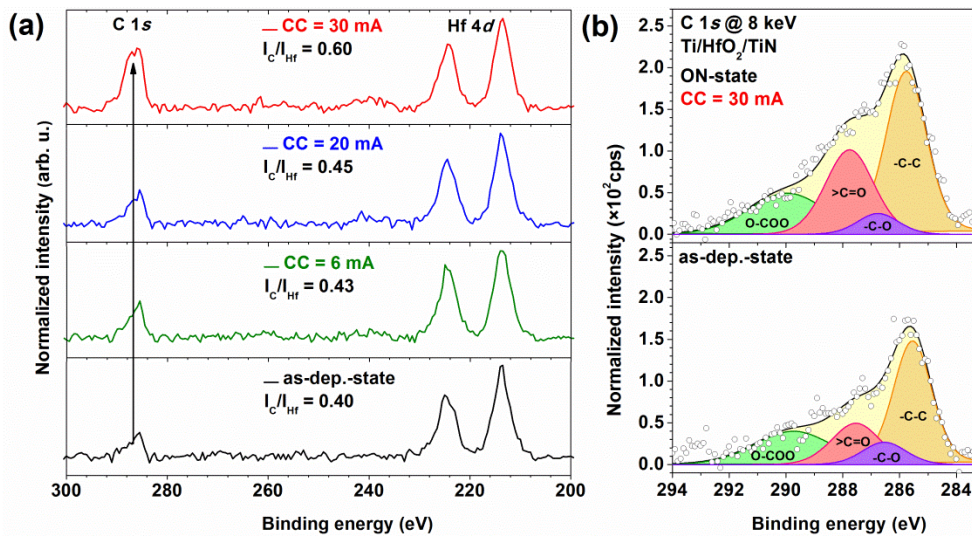


Figure 4.21: (a) Survey spectra of Sample G normalized to the Hf 4d peak intensity for the different resistive states: as-deposited, and three ON-states (CC = 6, 20 and 30 mA) recorded at 8 keV of excitation energy at normal emission geometry. The C 1s to Hf 4d peak intensity ratios (I_C/I_{Hf}) are indicated. (b) C 1s HAXPES spectra of Sample G in the as-deposited- and ON-state 30 mA. Both spectra are fitted with four components attributed to the -C-C (285.5 eV), -C-O (286.5 eV), >C=O (287.5 eV) and O-COO (289.7 eV) chemical bonds.

sample to the ON-state $CC = 30$ mA is visible. This result indicates that carbon impurities inside the AVD HfO_2 film may accumulate at the Ti/ HfO_2 interface during the resistive switching and become oxidized. As this might alter the oxygen vacancy balance at the Ti/ HfO_2 interface, the experimental findings will be investigated in more detail.

4.3.3 Discussion

The *in-operando* HAXPES study allows to correlate the forming/set characteristics of various current compliance and DC sweep voltage parameters with the materials modifications of the Ti/ HfO_2 /TiN RRAM cells. When the low current compliance and voltage parameters are used to operate the RRAM cell (Sample F and first cycle of Sample G), the forming-free resistive switching phenomenon is unstable. The absence of changes in the HAXPES spectra of Sample F indicates that – if at all – only subtle modifications may have occurred in the stack, however below the detection limit of the HAXPES technique and not sufficient to stabilize the resistive switching phenomenon. On the other hand, using higher current compliance and DC sweep voltage parameters during the forming/set operation of Sample G, the small material changes start to be detected in the HAXPES spectra. The monotonic decrease of Ti/ TiO_y and increasing binding energy of hafnium oxide components in the HAXPES spectra are observed and can be attributed to the increase of the positive oxygen vacancy-related space charge at the Ti/ HfO_2 interface region by an electrically driven Ti/ HfO_2 interface oxidation. A stable resistive switching is obtained only after the stepwise current (on positive voltage polarity) occurs in the I - V characteristic, as shown in Figure 4.18(b). It is supposed that this phenomenon is related to the electroforming process rather than to a change of the switching polarity mentioned in Ref. (120), because the subsequent resistive switching is again clockwise as before. Moreover, sudden increases of the current in I - V curves are attributed to the growth of multiple, parallel conductive filaments between the top and bottom electrodes when a sufficient amount of oxygen vacancies is created

inside the oxide, supporting the hypothesis of the electroforming process.^{(121) - (123)} Besides, Xue *et al.*,⁽¹²⁴⁾ have predicted that in the highly deficient hafnia the presence of tetragonal semimetallic Hf_2O_3 structures can serve as a basic explanation of the low resistive state of $\text{HfO}_{2-\delta}$ -based RRAMs. Experimentally, a metal-insulator transition as a function of oxygen vacancy concentration in the HfO_{2-x} thin films has been also observed.⁽¹¹⁹⁾ Furthermore, the first principle calculations⁽¹²⁵⁾ have also shown that a critical amount of oxygen vacancies have to be created inside the a- HfO_2 film to stabilize the resistive switching phenomenon. In more details, if the number of oxygen vacancies in the conductive filaments is too low, the transport may be in the trap-assisted regime and be dominated by the weakest link between vacancies. As the conductive filament lateral size is increased by the addition of more oxygen vacancies, the transport gap is reduced and sizable conductivity obtained.

Thus, it can be concluded that before the real electroforming occurs (i.e. for Sample F and Sample G with CC = 6 mA) the number of oxygen vacancies is too low and the conductive filaments are too weak to maintain a stable resistive switching. As the current compliance and DC sweep voltage parameters are increasing, the oxygen vacancies concentration in the HfO_2 also increases and expands the conductive filaments lateral size. When the amount of oxygen vacancies in such filaments is sufficient, the resistive switching is stabilized and the ON-state current can be controlled by the current compliance and/or DC sweep voltage parameters.

4.3.4 Summary and conclusions

In summary, the impact of various current compliance and DC sweep voltage parameters on the forming/set process of the Ti/a- HfO_2 /TiN cells was investigated by correlating the material science aspects of the Ti/a- HfO_2 interface with electrical measurements using *in-operando* HAXPES. Stable resistive switching in amorphous AVD HfO_2 -based RRAMs was only possible after that the sample

was electroformed by using higher current compliance and DC sweep voltage parameters. HAXPES data have shown the slight increases of the Ti oxidation and the C concentration at the Ti/a-HfO₂ interface, and the binding energy, with the increasing electrical power applied to the cell.

Both the electrical and HAXPES results correlated with literature indicate that the value of the applied electrical power during the forming/set operation to the RRAM cell defines the oxygen vacancies concentration in the oxide and thus the resistive switching properties.^{(126) - (129)} Besides, the defect physics in the AVD a-HfO₂-based RRAMs seems to be not only limited to the oxygen vacancies, but other impurities, such as C, may contribute under electrical stress to the resistive switching behavior and thus influence the switching characteristics.

In conclusion, it seems that the materials modification in the RRAM cells must overcome a certain threshold (i.e. critical concentration of oxygen vacancies in HfO₂) to stabilize the resistive switching phenomenon.

4.4 *In-operando* switching of Ti/HfO₂/TiN cells

In this chapter, the *in-operando* HAXPES results of the as-deposited- and the 7th ON- and OFF-state of DC sweep cycled Sample G will be presented. Additionally, the segregation of C impurities at the Ti/a-HfO₂ interface, while DC sweep voltage cycling of Sample H, was investigated by means of *in-operando* HAXPES.

4.4.1 Electrical characterization

In Figure 4.22(a) the *I-V* characteristics of the 7 DC sweep voltage cycles are shown, performed on the electroformed (at positive voltage polarity) Sample G. The $R_{\text{OFF}}/R_{\text{ON}}$ ratio, read at 0.1 V, after the 7th resistive switching cycle is equal to 7. The conduction mechanism of Sample G in the ON- and OFF-state can be determined from the double logarithmic *I-V* characteristic (Figure 4.22(b)). As can be seen, there is a linear relationship between current and voltage in the ON-state. The slope coefficient of the curve related to the ON-state is equal to 1 on both voltage polarities. This result indicates that the conduction mechanism in the ON-state can be attributed to ohmic conduction.⁽¹²¹⁾ Thus, Sample G being in the ON-state behaves as a metallic conductor. However, when this sample is reset to the OFF-state a nonlinear current versus voltage relationship is observed, suggesting a non-ohmic conduction mechanism. In the higher voltage range of the OFF-state, the curve can be approximately fitted with a straight line, which slope coefficient is equal to 1.7 (on a positive voltage polarity) and to 1.6 (on a negative voltage polarity), while in the lower voltage range the *I-V* slope coefficient is equal to 1. The non-ohmic conduction mechanism in the OFF-state can probably be related to a trap-unfilled space charge limited current, for which the slope coefficient in a double logarithmic *I-V* plot is equal to 2.⁽¹²¹⁾

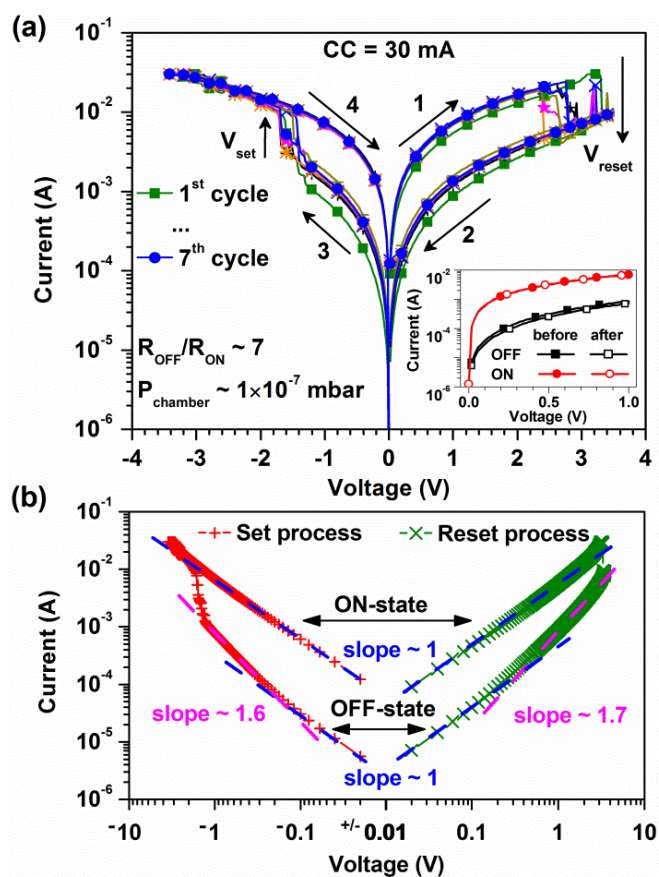


Figure 4.22: (a) I - V characteristics showing the resistive switching behavior of Sample G in a DC sweep mode. After 7 cycles the $R_{\text{OFF}}/R_{\text{ON}}$ ratio, read at 0.1 V, is equal to 7. The inset shows the current levels for both ON- and OFF-states before and after the HAXPES experiments. (b) I - V characteristic of the 7th cycle presented in a double logarithmic plot with marked slope coefficient in OFF- and ON-states.

4.4.2 HAXPES characterization

The chemical and electronic modifications that occur in Sample G between the as-deposited and the 7th OFF- and ON-states are analyzed by HAXPES spectra.

Chemical modifications

The most visible chemical changes between these three resistive states of Sample G were found again in the Ti photoemission lines. Figure 4.23 shows fitted (with

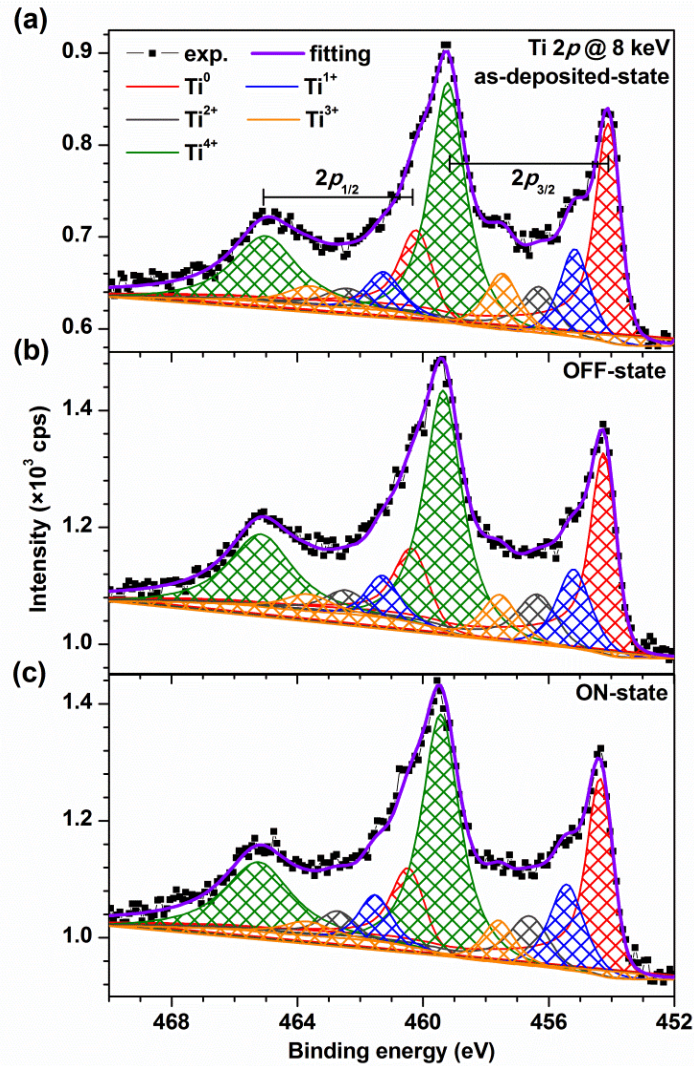


Figure 4.23: Ti 2*p* HAXPES spectra of Sample G in the as-deposited- (a), OFF- (b), and ON-states (c), recorded at excitation energy of 8 keV. A Shirley background and 5 components attributed to titanium oxidation states between 0 and +4 are shown.

same parameters as in the previous sections) Ti 2*p* HAXPES spectra of the as-deposited- (a), OFF- (b) and ON-states (c). The individual Ti oxidation states intensities in the Ti 2*p* photoemission line, ρ , for each investigated resistance state of Sample G was derived from the fitting results and is shown in Table 4.3. The results of this fitting allowed to calculate the Ti/TiO_y ratio. The increase of the Ti oxidation from the as-deposited- (0.60 ± 0.03) to the OFF- (0.52 ± 0.03) and ON-

state (0.53 ± 0.03) is consistent with the previously observed relation between the as-deposited and electroformed samples. Namely, the interface between Ti and HfO_2 becomes more oxidized under electrical manipulation by an oxygen migration from the HfO_2 towards Ti film. Despite the fact that the overall Ti/TiO_y ratio for the ON- and OFF-states does not significantly differ, a clear redistribution of intensity between the different Ti oxidation states is detected. Whereas only minor or no changes are observed for the Ti^0 , Ti^{2+} and Ti^{4+} components between the ON- and OFF-states, a clear intensity redistribution is observed for the $\text{Ti}^{1+}/\text{Ti}^{3+}$ redox system. Indeed, the increase of the Ti^{1+} intensity at the expense of the Ti^{3+} intensity, when passing from the OFF- to the ON-state, indicates a decrease of the oxidation state of the Ti in the interface layer. The set process at a negative voltage polarity can be thus interpreted either by attracting oxygen vacancies to the Ti/ HfO_2 interface or repelling oxygen anions from it, both reducing the metallic Ti content in the top electrode film. In turn, the reset process of the device to the OFF-state by a positive voltage can be related to the attraction of oxygen anions (or to the repulsion of oxygen vacancies from the top electrode to the bulk HfO_2) causing enhanced Ti oxidation. This behavior, independent of considering oxygen anions or oxygen vacancies, suggests that the TiO_x interface layer plays the role of an oxygen reservoir in exchange with the $\text{HfO}_{2-\delta}$ film during the resistive switching process.^{(57), (120)}

Table 4.3: Percentage intensity I_{Ti} of the different oxidation states in the Ti 2p core level for the as-deposited-, OFF- and ON-states. The grey cells show the main differences between the OFF- and ON-states.

$I_{\text{Ti}} \pm 0.2$ (%)	Ti^0	Ti^{1+}	Ti^{2+}	Ti^{3+}	Ti^{4+}
As-deposited	37.3	9.9	10.8	7.1	34.8
OFF	34.3	9.9	12.8	5.9	37.1
ON	34.5	10.8	12.8	4.9	36.9

Table 4.4: Experimental peak shifts ($\Delta BE^{\text{OFF/ON}} = BE^{\text{OFF/ON}} - BE^{\text{as-deposited}}$) between the OFF- or ON-states and the as-deposited-state, for metallic Ti $2p_{3/2}$ (Ti^0), Hf $4f_{7/2}$ and O $1s$ lines.

$\Delta BE \pm 0.03$ (eV)	Ti $2p_{3/2}$ (Ti^0)	Hf $4f_{7/2}$	O $1s$
ΔBE^{OFF}	0.15	0.07	0.14
ΔBE^{ON}	0.27	0.18	0.23

Electronic modifications

Now the electronic changes detected in the HAXPES spectra of the three resistance states of Sample G will be presented. Figure 4.24(a) shows the Hf $4f$ doublet (including also the O $2s$ line) and Figure 4.24(b) the intensive O $1s$ line (including less intensive Hf $4s$ peak). As shown in the insets, the Hf $4f_{7/2}$ and O $1s$ lines shift towards higher binding energy in the order of $BE^{\text{as-deposited}} < BE^{\text{OFF}} < BE^{\text{ON}}$. The binding energy shifts values are summarized in Table 4.4. As proposed by other groups^{(79), (115), (118)} and in the Section 3.2, these peak shifts towards higher binding energy can be attributed to the increase of the n -type dopants concentration in the HfO_2 film, which can be further related to the oxygen

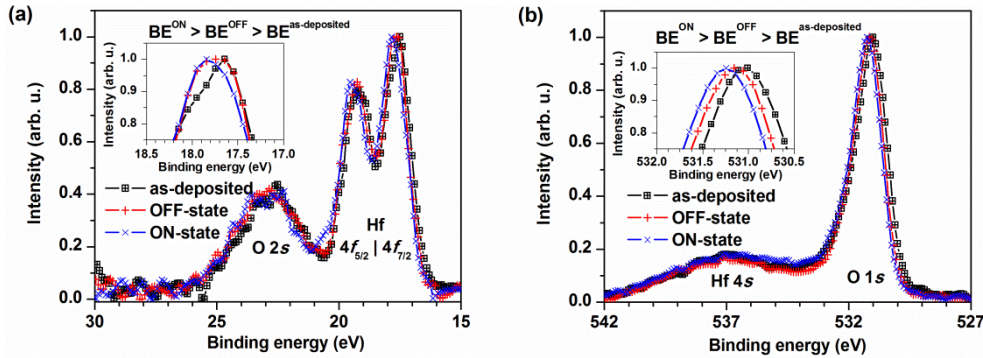


Figure 4.24: Normalized and smoothed HAXPES spectra of (a) the Hf $4f$ doublet and the O $2s$ line and (b) of the O $1s$ and Hf $4s$ lines recorded at excitation energy of 8 keV from the sample in the as-deposited-, OFF- and ON-states. The shifts of the Hf $4f_{7/2}$ and O $1s$ main peaks are highlighted in the insets.

vacancies. Thus the observed different peak shifts in the HAXPES spectra between the ON- and OFF-state can be attributed to the different oxygen vacancies concentrations at the Ti/HfO₂ interface.

4.4.3 Proposed resistive switching model

Comparing electrical data with the observed chemical and electronic modifications in the HAXPES spectra, the possible scenario of the resistive switching origin in the Ti/a-HfO₂/TiN cell is proposed in Figure 4.25. In the as-

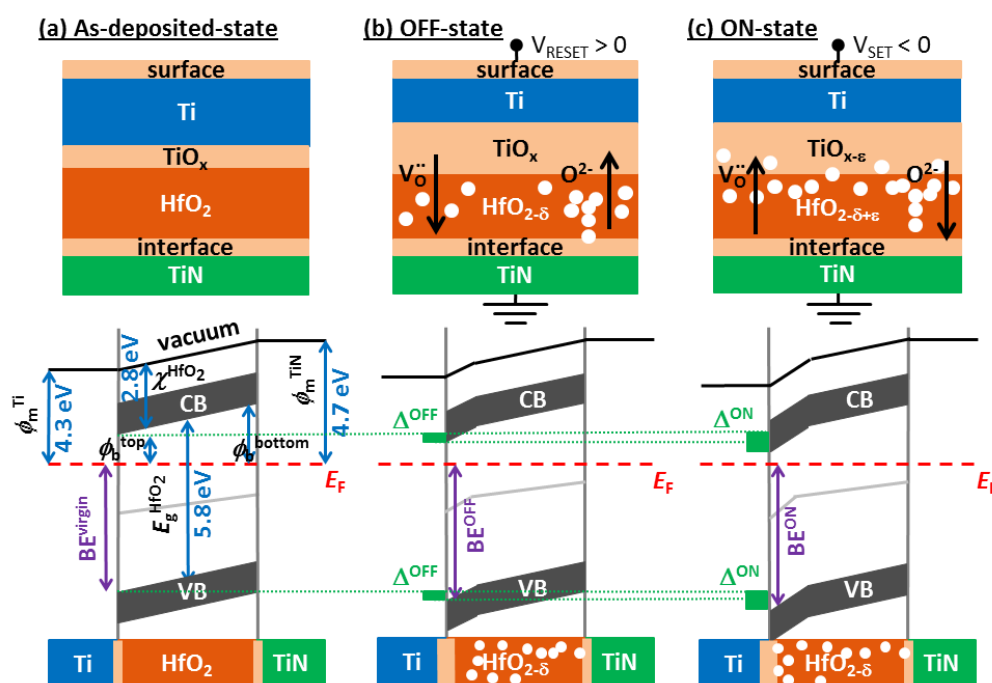


Figure 4.25: Schematic of proposed chemical (top) and electronic (bottom) modifications between the as-deposited- (a), OFF- (b) and ON- (c) states of the resistive switching in the Ti/HfO₂/TiN-based system. The different concentrations of oxygen vacancies ($V_{O^{\bullet}}$) at the Ti/HfO₂ interface in the OFF- and ON-states give rise to the band bending. The used symbols are defined as: Φ_b – the conduction band offset, Φ_m – the metal work function, BE – the binding energy, E_g – the gap energy, E_F – the Fermi level, CB – the conduction band, VB – the valence band, χ – the electron affinity.

deposited-state (a), the MIM stack already presents a TiO_x interface layer between the Ti and HfO_2 films and a downward band bending towards the top electrode in the energy band diagram, due to the difference in the Ti and TiN metal work functions.^{(12), (114)} The electroforming step leads to a further oxidation of the as-deposited Ti/ HfO_2 interface by enhancing the TiO_x layer. It is supposed that during this process oxygen vacancies are formed in HfO_2 , and a downward band bending at the Ti/ HfO_2 interface increases, lowering at the same time the barrier height and increasing thus the conduction.⁽¹³⁰⁾ The OFF- and ON-states arise from different concentrations of oxygen vacancies, $[\text{V}_{\text{O}}^{\cdot\cdot}]$, at the Ti/ HfO_2 interface: $[\text{V}_{\text{O}}^{\cdot\cdot}]^{\text{as-deposited}} < [\text{V}_{\text{O}}^{\cdot\cdot}]^{\text{OFF}} < [\text{V}_{\text{O}}^{\cdot\cdot}]^{\text{ON}}$. This raising concentration of oxygen vacancies induces a higher bending of the conduction and valence bands and a decrease of the barrier height at the top electrode interface, as sketched.⁽¹¹²⁾ A push-pull model can describe the migration of oxygen vacancies at the top interface.⁽¹³¹⁾ A positive voltage applied to the top electrode (reset process) repels positively charged vacancies from the interface and in effect, the band bending is reduced and the device is set to the OFF-state (Figure 4.25(b)). At the reversed polarity (set process), oxygen vacancies are attracted which increases the band bending and brings the device to the ON-state (Figure 4.25(c)). This is in agreement with the picture that the TiO_x interlayer plays the role of an oxygen reservoir, according to the higher oxidation state of the Ti in the OFF-state than in the ON-state, as also previously reported for Ta-based devices.^{(57), (132)}

4.4.4 Carbon behavior during cycling

In order to investigate the C impurities behavior during the resistive switching cycling, Sample H was cycled 120 times by means of *in-operando* HAXPES. The relevant *I-V* characteristics presenting the 1st, 10th, 20th and 120th cycle are shown in Figure 4.26(a). In Figure 4.26(b) is shown an endurance plot reporting at 0.2 V the current levels for the ON- and OFF-states. As can be seen, while the ON-state current level is quasi constant the OFF-state current level is going towards the ON-state over the cycling. As the final effect of this cycling, the device presents a

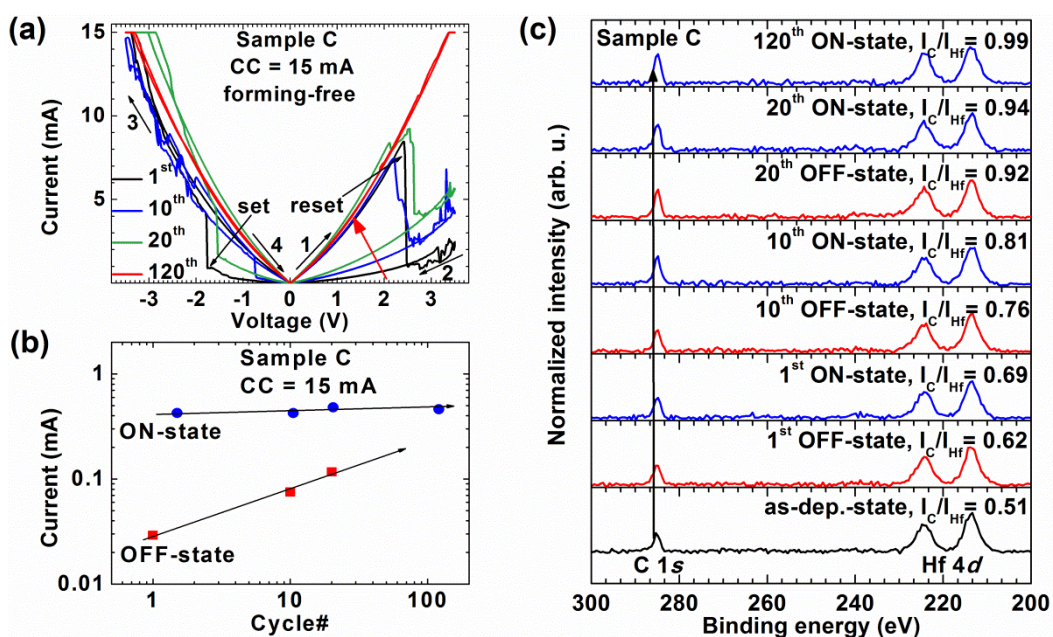


Figure 4.26: (a) I - V characteristics showing the 1st, 10th, 20th and 120th resistive switching cycle of Sample H. (b) Current levels read at 0.2 V for ON- and OFF-states. (c) Normalized survey scan spectra recorded at 8 keV excitation energy, for the as-deposited-, OFF- and ON-states of Sample C (I_C/I_{Hf} ratio is indicated).

reset failure (120th cycle in Figure 4.26 (a)), i.e. it cannot be reset to the OFF-state. The relevant HAXPES survey scan spectra normalized to the Hf 4d peak intensity are shown in Figure 4.26(c). A clear increase of the C peak intensity over the cycles is observed. The calculated I_C/I_{Hf} ratio in Figure 4.26(c) indicates that the cycling increases the C concentration at the Ti/HfO₂ interface. In particular, the I_C/I_{Hf} ratio increases by a factor of two from 0.51 for the as-deposited-state to 0.99 for the 120th ON-state. These results suggest that the resistive switching may be not only based on oxygen vacancies migration but also C impurities might participate to the switching mechanism and should thus be taken into account. The exact role of C impurities in the resistive switching phenomena is not yet clear but three different scenarios can be envisioned. Firstly, ab-initio calculations indicate that the isolated, non-reacted C impurities behave electronically very similar to the oxygen vacancies in HfO₂.⁽¹³³⁾ This means that a chain of C

impurities is capable of regular transport. Moreover, the creation of conductive C filament(s), in addition to oxygen vacancies-based filaments, might be then possible and will thus certainly impact the resistive switching properties. Secondly, C can form defect complexes with oxygen vacancies.^{(134) - (136)} In consequence, increased C segregation to the metal/oxide interface^{(137), (138)} can thus critically influence the oxygen vacancies balance in the HfO₂ film. Thirdly, another possibility of influencing the oxygen vacancies concentration in the HfO₂ film by C impurities is given by C oxidation in the HfO₂ film.

4.4.5 Summary and conclusions

A stable resistive switching phenomenon in the Ti/a-HfO₂/TiN cell was investigated by means of *in-operando* HAXPES. The collected HAXPES spectra have indicated an increase of the overall titanium oxidation in the ON- and OFF-state of Sample G. The detected differences in the HAXPES spectra of both states correspond to a redistribution of the different Ti oxidation states. In particular, the data indicate that a redox reaction between the HfO₂ and the Ti films (via the Ti¹⁺ and Ti³⁺ oxidation states) is at the very heart of this oxygen reservoir role of the TiO_x interface. Moreover, the higher peak shift for the ON- than for the OFF-state can be attributed to the higher oxygen vacancies concentration at the Ti/HfO₂ interface in the ON-state. Besides, the detailed analyses of the electrical data indicate that the ON-state behaves as a metallic conductor whereas the conduction in the OFF-state is rather non-ohmic and can be attributed to the conduction of the trap-unfilled space charges. Moreover, the *in-operando* HAXPES cycling experiment shows that the endurance of a stable resistive switching as well as the resistive switching phenomenon itself may be affected by other HfO₂ defects, such like C impurities present in that film due to the deposition process. In particular, an increasing C segregation at the Ti/HfO₂ interface is observed over the increasing number of cycles.

Therefore, despite the fact that the resistive switching origin in the HfO₂-based RRAMs is already well accepted and attributed to the creation and rupture of

conducting oxygen vacancies filaments the *in-operando* results indicate that other HfO₂ impurities may be also involved. This finding is of particular relevance to improve the reliability (endurance, retention, etc.) of RRAM devices.

Chapter 5

SUMMARY AND OUTLOOK

5.1 Summary

Non-volatile memory devices are currently key elements for many different system applications in Si-based CMOS technologies, including high-end and mobile computing, consumer electronics, and various sensor and medical health care devices. They can be used e.g. in digital cameras, solid state disks, smartphones, computers, e-books, tablets or WSNs. Even though the Flash memory represents today the leading non-volatile memory technology it is approaching physical limits. To achieve higher scalability but also better performance, density and speed than Flash, as well as to address low power consumption, low thermal budget and compatibility with flexible substrates and embedded systems, new emerging non-volatile memory concepts are of importance. Among them, ReRAM is a major candidate to replace nowadays Flash in future.

Whereas a fully CMOS compatible TiN/Ti/HfO₂/TiN ReRAM stack, whose potential is currently evaluated, has been successfully integrated with a select transistor (1T1R memory) by IHP, the **reliability** and **insufficient understanding of the resistive switching mechanism** have been the two main issues limiting the ReRAM technology development for e.g. WSN applications.

With this respect, to improve the performance of the TiN/Ti/HfO₂/TiN ReRAM cells, an innovative *in-operando* HAXPES setup has been established to non-destructively investigate the material changes within the HfO₂ film and/or at the

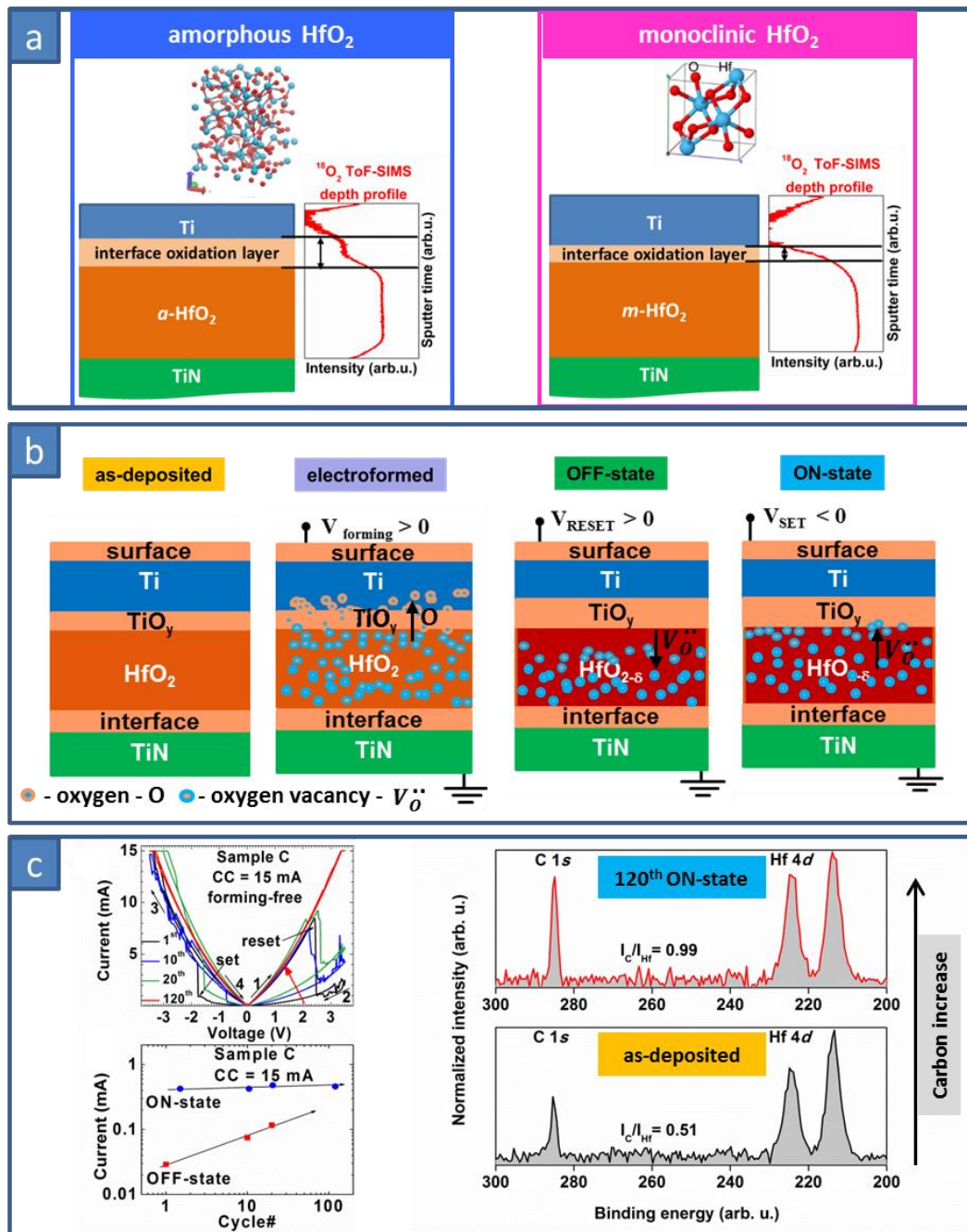


Figure 5.1: Overview of three most important results of this Thesis (a) Ti oxidation degree dependence on HfO₂ film crystallinity. (b) Proposed chemical and electronic changes of Ti/HfO₂/TiN ReRAM based on *in-operando* HAXPES results. (c) Carbon accumulation at Ti/HfO₂ interface during switching of Ti/HfO₂/TiN ReRAM cells.

Ti/HfO₂ interface (in conjunction with complementary material science characterization techniques and theoretical calculations). It is noted, that the defect-based switching physics in ReRAM provides a challenge for today's laboratory based materials science techniques so that the innovative non-destructive HAXPES technique with high energy resolution and sensitivity at 3rd generation synchrotron sources was applied in this Thesis.

The summary of the main results obtained in this Thesis and an overview of three main achievements, shown in Figure 5.1, are presented hereafter.

5.1.1 As-deposited Ti/HfO₂ interface

At the beginning, the as-deposited Ti/HfO₂ interface was investigated by means of different techniques. First, the growth of Ti on HfO₂ was monitored *in-situ* at IHP's MBE system. This is because *in-situ* studies are not possible under typical IHP's BEOL processing of the Ti/HfO₂/TiN ReRAM cells in the AVD chamber. The *in-situ* XPS results indicate that during the MBE process Ti atoms are initially poorly bonded to the HfO₂ substrate, and thus Ti oxides islands nucleate and expand three dimensionally in all directions. In a further process, the Ti islands become more and more metallic and after certain time they coalesce and grow further as a metallic film (layer by layer). These results allow to conclude that there is an oxidation process of the Ti film at the interface with HfO₂, and thus **the creation of the Ti//TiO_x/HfO_{2-δ} interface layer in the as-deposited stack.**

Next, ToF-SIMS studies performed on samples prepared with ¹⁸O isotope-marked HfO₂ confirmed the Ti layer's chemical reactivity with the oxygen coming from the HfO₂ film. Moreover, GIXRD and HAXPES studies have revealed **a higher degree of Ti oxidation in case of Ti films deposited on amorphous than on monoclinic HfO₂ films** (Figure 5.1(a)). This experimental result was then confirmed by first principle calculations, namely, a lower formation energy was found for the formation of oxygen vacancies in amorphous than in monoclinic

HfO₂ films. Experiment and theory confirm thus an enhanced Ti oxidation activity with amorphous HfO₂ films.

Finally, *off-line* characterization of BEOL-processed Ti/AVD a-HfO₂/TiN samples confirmed the same results, as observed for the MBE-processed model samples. In detail, the presence of the TiO_x interface layer between the as-deposited Ti and a-HfO₂ layers was detected in particular by STEM-EDX studies. Besides, the EDX characterization **revealed the presence of impurities in the HfO₂ film** (e.g. N, C etc.), probably resulting from the used AVD precursor chemistry.

5.1.2 *Ex-situ* study of electroformed Ti/a-HfO₂/TiN cells

In the next step, the BEOL-processed Ti/AVD a-HfO₂/TiN samples were investigated in terms of their resistive switching properties. First, the positive DC sweep voltage applied to the as-deposited Ti/AVD a-HfO₂/TiN stack during the electroforming process changed its resistance by about three orders of magnitude. The subsequent DC sweep voltage cycle showed **a clockwise bipolar resistive switching behavior of the positively electroformed Ti/AVD a-HfO₂/TiN stack**. Next, *ex-situ* HAXPES study performed on both samples (as-deposited and electroformed) revealed significant chemical and electronic differences. Namely, in comparison to the as-deposited sample, HAXPES detected an increase of (1) the Ti/a-HfO₂ interface oxidation and (2) of the binding energy in the electroformed sample. Both changes, compared with the literature, indicate the **creation of *n*-type dopants in the a-HfO₂ film during the electroforming process, probably related to the formation of positively charged oxygen vacancies in a-HfO₂ by the electrochemical Ti/a-HfO₂ interface oxidation** (Figure 5.1(b)).

5.1.3 Impact of electrical power on changes in Ti/a-HfO₂/TiN cells

Next, the impact of various current compliance and DC sweep voltage parameters on the Ti/AVD a-HfO₂/TiN ReRAM cells was investigated by means of *in-operando* HAXPES. These studies evaluated the **possibility of a forming-free resistive switching in the Ti/AVD a-HfO₂/TiN samples while using low electrical power**. However, this resistive switching was unstable and a stable switching was observed only after the sample was firstly electroformed at a positive voltage polarity using higher electrical power.

By correlating the materials science aspects of the Ti/a-HfO₂ interface with electrical measurements and literature, it can be concluded that **the value of the applied electrical power to the Ti/AVD a-HfO₂/TiN cells during the forming/set operation defines the oxygen vacancies concentration in the a-HfO₂ and thus the stability of the resistive switching properties**. It means that the higher the electrical power parameters, the more oxygen vacancies are formed in the a-HfO₂ film by the electrically driven Ti/a-HfO₂ interface oxidation. A critical oxygen vacancy concentration needs thus to be formed to achieve stable switching characteristics.

Besides, **the defect physics in the Ti/AVD a-HfO₂/TiN ReRAM seems to not be limited to oxygen vacancies, as other impurities, such as carbon, may contribute under electrical stress to the resistive switching and thus influence the switching characteristics**. Namely, with increasing electrical power parameters, an increasing segregation of carbon at the Ti/a-HfO₂ interface was observed in the HAXPES spectra. This result could be attributed to an electrically driven carbon segregation mechanism at this interface.

5.1.4 Stable resistive switching in Ti/a-HfO₂/TiN cells

Finally, by means of *in-operando* HAXPES technique, the differences between the as-deposited-, and the stable ON- and OFF-states were investigated. As in previous studies, the HAXPES results of the electrically changed states showed,

in comparison to the as-deposited-state, an increase of the Ti oxidation and an increase of the binding energies of peaks related to Hf oxides. Next, the main difference between the OFF- and ON-states is that there is a different Ti oxides redistribution in the Ti 2*p* HAXPES spectra. **The observed redox reactions between the a-HfO₂ and the Ti films via the Ti¹⁺ and Ti³⁺ oxidation states is, according to these results, at the very heart of the Ti/a-HfO₂ interface layer role as an oxygen exchange reservoir for the resistive switching** (Figure 5.1(b)). Its role is then confirmed by observed higher photoemission peak shift in the ON- than in the OFF-state HAXPES spectra. As stated previously, the higher peak shift can be attributed to a space charge region created by the higher oxygen vacancies concentration at the Ti/a-HfO₂ interface. Moreover, the simulation of the *I-V* characteristics of both states revealed that the **ON-state behaves as metallic conductor whereas the OFF-state conduction can be attributed to trap-unfilled space charge limited current**. Besides, the *in-operando* HAXPES cycling experiment showed that the endurance of a stable resistive switching as well as the resistive switching phenomenon itself may be affected by other HfO₂ defects, such like C impurities present in the film due to the AVD deposition process. In particular, **an increasing C segregation at the Ti/a-HfO₂ interface is observed over the increasing number of switching cycles** (Figure 5.1(c)).

5.2 Conclusions

5.2.1 Resistive switching origin in Ti/a-HfO₂/TiN ReRAM cells

Results of the studies presented in this PhD Thesis indicate that the resistive switching phenomenon in the Ti/AVD a-HfO₂/TiN ReRAM cells can be related to the oxygen vacancies migration under the influence of an electrical field. The as-deposited, amorphous HfO₂ film contains already a certain amount of oxygen vacancies due to the oxygen scavenging by a chemically reactive Ti electrode. This fact leads further to the possibility of a forming-free resistive switching. However, it is not stable and thus indicates that the initial oxygen vacancies concentration in HfO₂ is not sufficient to stabilize the resistive switching event. Therefore, an electroforming step is thus required to stabilize it. However, the *in-operando* HAXPES results indicate that the resistive switching in the Ti/AVD a-HfO₂/TiN ReRAM cells is not limited to oxygen vacancies. An observed increase of the C 1s signal in HAXPES spectra while increasing the applied electrical power to the RRAM cell or while cycling the device indeed showed that the carbon impurity role in the resistive switching cannot be ignored. Therefore, other impurities present in the as-deposited a-HfO₂ films, highlighted in this Thesis by carbon, may contribute under electrical stress to the resistive switching phenomenon and thus influence the switching characteristics (e.g. reliability, etc.).

5.2.2 Improved Ti/a-HfO₂/TiN RRAM cells performance

In order to verify the last finding of this Thesis – the carbon impact on the resistive switching behavior of Ti/HfO₂/TiN ReRAM – the HfO₂ films were deposited by AVD at different temperatures, in order to reduce the carbon content in these films. As can be seen in Figure 5.2, showing the ¹²C ToF-SIMS depth profile, the carbon content was reduced from around 8 at.% to 3.3 at.% while increasing the deposition temperature from standard 320 °C to 450 °C. It is noted

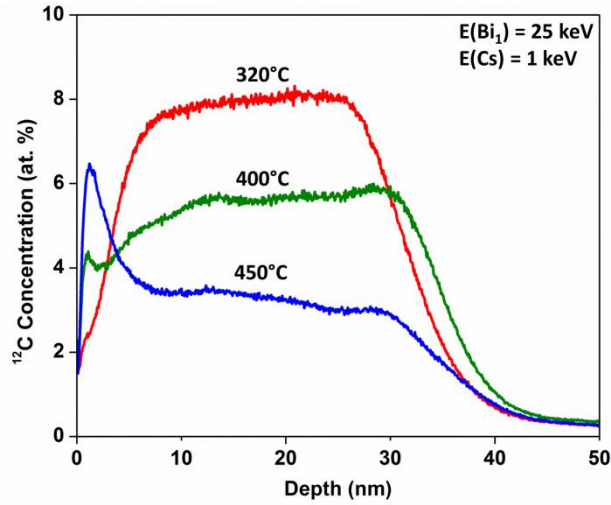


Figure 5.2: ^{12}C ToF-SIMS depth profiles performed across the HfO_2 film deposited at 320 °C, 400 °C and 450 °C.

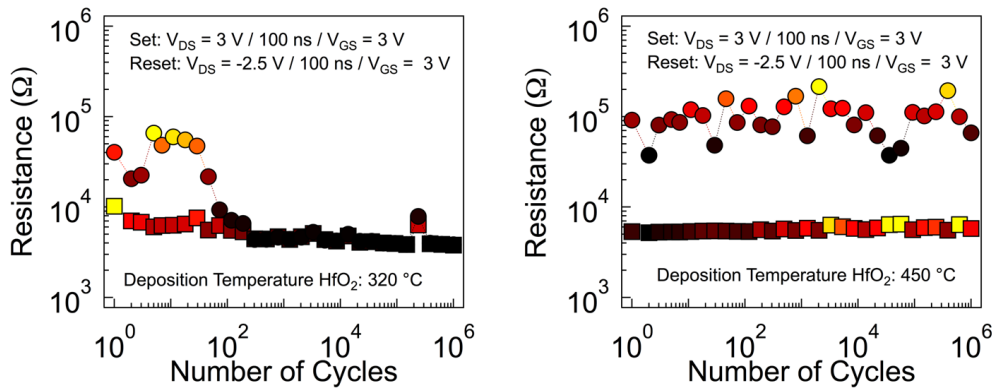


Figure 5.3: Endurance plot of 1T1R integrated $\text{Ti}/\text{HfO}_2/\text{TiN}$ ReRAM cells with HfO_2 film deposited at (a) 320 °C and (b) 450 °C.

that this temperature is the maximum value to keep the RRAM process BEOL compatible. Next, two integrated 1T1R devices, one with the HfO_2 film deposited at 320 °C and one at 450 °C, were prepared in order to perform pulse-induced resistive switching endurance measurements. During the measurements, for both samples, the gate-source voltage (V_{GS}) was equal to 3 V for the set and reset processes, the pulse lengths and amplitudes were set to 100 ns and 3 V (for set) or -2.5 V (for reset), on the drain side. Figure 5.3 shows the endurance plots of $0.6 \times 0.6 \mu\text{m}^2$ integrated $\text{TiN}/\text{Ti}/\text{HfO}_2/\text{TiN}$ cells with HfO_2 deposited at (a) 320 °C and

(b) 450 °C. As can be seen, a stable pulse-induced endurance with $> 10^6$ cycles was observed for HfO₂ deposited at 450 °C while for the 320 °C deposited HfO₂ film, the resistance window closed after around 10^2 cycles. Thus, this result points to the possibility to improve the performance of the TiN/Ti/HfO₂/TiN ReRAM cells by a reduction of the carbon content in the dielectric layer. This is a very promising result for the development of reliable future ReRAM technologies for WSNs applications.

5.2.3 Limitations of HAXPES

The resistive switching origin in the Ti/AVD a-HfO₂/TiN cells, attributed by HAXPES investigations to an electrochemically active Ti/HfO₂ interface in combination with a push-pull mechanism of oxygen vacancy migration under electrical bias, classifies this ReRAM system to the **valence change memories**.

Polarity characteristics of the switching phenomenon

The VCM mechanism, proposed in Figure 2.6 for *n*-conducting oxide, is in line with the push-pull model of oxygen vacancies proposed in this Thesis. In detail, this mechanism also attributes the location of the switching event for the clockwise resistive switching polarity at the top Ti/HfO₂ interface while grounding bottom electrode and applying signal to the Ti top electrode (see Figure 5.4(a)).

However, if in accordance with literature models,⁽⁵²⁾ one assumes TiN as an active electrode, at which the switching takes place (a metal with a low oxygen affinity) and Ti as an ohmic electrode (a metal with a low work function and a high oxygen affinity), then this widely accepted switching model does not describe the resistive switching behavior in the model Ti/AVD a-HfO₂/TiN samples. To this assumption, the resistive switching should present a counter clockwise behavior while applying the signal to the Ti top electrode and grounding the TiN bottom electrode and the switching event should thus occur at the bottom HfO₂/TiN interface. Such counter clockwise character (Figure 5.4(b))

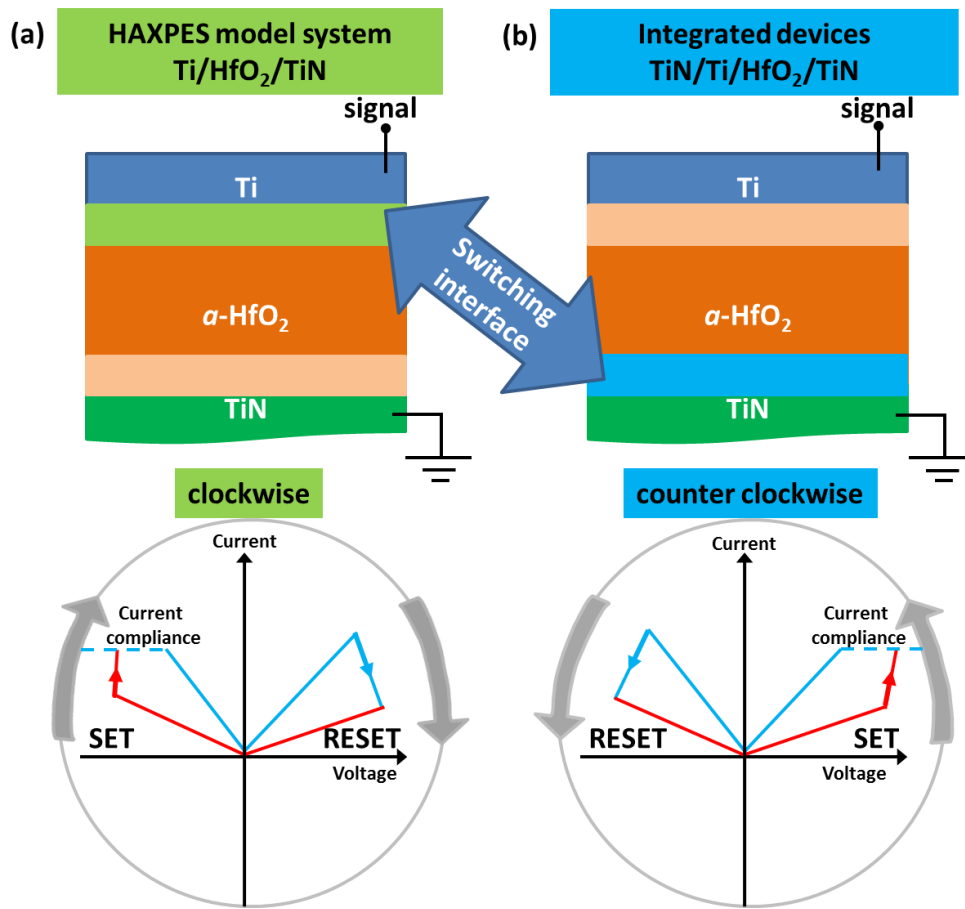


Figure 5.4: Schematic representation of resistive switching polarity (bottom) and indication of switching interface (top) in Ti/HfO₂/TiN model HAXPES system (a) and in integrated TiN/Ti/HfO₂/TiN devices (b).

is indeed observed for IHP's integrated TiN/Ti/HfO₂/TiN devices⁽¹⁴⁾ and in other integrated HfO₂-based VCM systems^{(27), (139)}. Therefore, it can be assumed that in case of the integrated HfO₂-based ReRAM devices, the Ti layer acts as an ohmic electrode and TiN layer as an active electrode and the resistive switching can be explained according to the model shown in Figure 2.6. A possible explanation, why for one and the same ReRAM system opposite polarity for the switching characteristics may be observed, might be based on the initial oxygen vacancies gradient profile across the oxide film.^{(52), (62)} In the model proposed in Ref. (62) for a symmetric Pt/TiO_{2-x}/Pt ReRAM system, if an oxygen deficient *n*-type layer is located at the bottom electrode and the fully oxidized

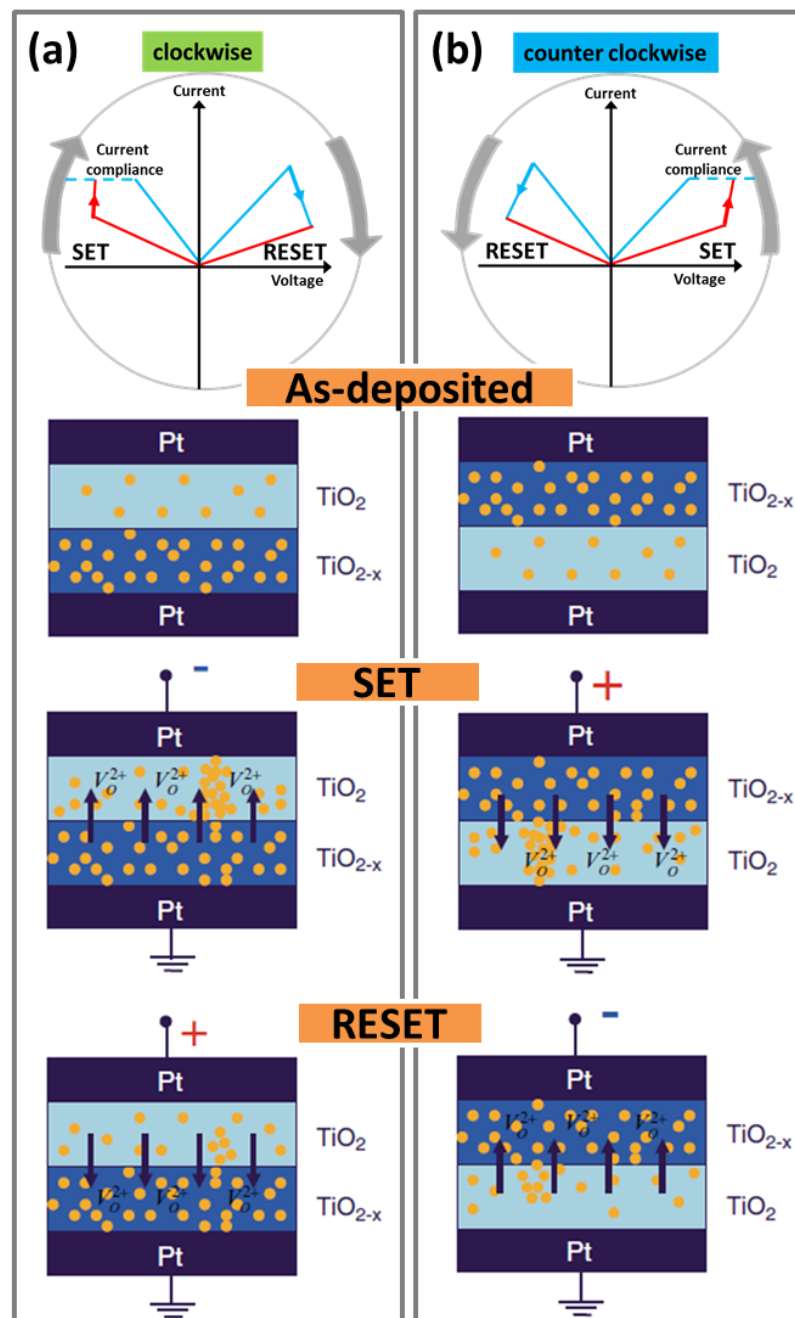


Figure 5.5: Schematic representation of clockwise (a) and counter clockwise (b) resistance switching in titanium oxide films with oxygen vacancy gradient for symmetric Pt top and bottom electrodes. ⁽⁶²⁾

stoichiometric oxide on the top electrode side then the oxygen vacancy concentration in the deficient oxide is higher compared to the near stoichiometric part. Next, if the doping level of oxygen vacancies at the bottom electrode interface is high enough, then an ohmic contact is formed and the switching process occurs only at the rectifying interface between the stoichiometric oxide part of the bilayer and the electrode, as shown in Figure 5.5(a).⁽⁶²⁾ Application of a negative voltage to the top electrode attracts the oxygen vacancies into the near stoichiometric oxide layer and toward the top interface and the sample is set to the ON-state. Then, a positive voltage applied to the top electrode repels oxygen vacancies from the top interface and resets the sample to the OFF-state. It should be noted, that under bias voltage the oxygen vacancy concentration and distribution will also change at the bottom electrode interface. However, this change is not significant enough to change the ohmic behavior. Upon reversing the fabrication sequence (fully oxidized oxide at the bottom electrode and the non-stoichiometric oxide at the top electrode) the polarity for reset and set processes are reversed, as shown in Figure 5.5(b). According to this model, the rectification and the switching polarities are thus determined by the initial distribution of the oxygen vacancies in the dielectric layer.

The reason why the resistive switching polarity is opposite for integrated HfO₂ ReRAM and HAXPES HfO₂-based ReRAM model system is not yet clear. Intuitively, the following differences can be stated:

- **(1) Sample size:** integrated devices are at least three orders of magnitude smaller than the model samples used in this Thesis;
- **(2) Layer thickness:** a 150 nm TiN top layer is used in the integrated devices in order to protect the Ti layer against unwanted oxidation.
- **(3) Applied power:** as a consequence of (1) and (2), the applied power parameters to switch HAXPES model system substantially differ with respect to integrated devices.

Unfortunately, due to the limited sample size and the TiN top electrode thickness, it is not possible to directly apply HAXPES to fully integrated device but model systems need to be addressed.

Interface versus filamentary switching

The HAXPES technique cannot distinguish between filamentary and interface type resistive switching, due to too low lateral resolution. However, HAXPES results clearly confirm literature reports that oxygen vacancies – probably in filament shape – are decisive for HfO₂-based ReRAMs. This oxygen vacancies-based filamentary type resistive switching – instead of an interface model – is further supported by the observed conductive filament(s) resistance dependence on the DC sweep voltage range ⁽¹²⁶⁾ and/or current compliance used during the forming/set operation. ^{(127) - (129), (140), (141)}

In consequence, *in-operando* materials science techniques which are non-destructive and provide high energy as well as spatial resolution plus highest sensitivity are highly needed in order to unveil the defect-related physics of ReRAM systems.

5.3 Outlook

Certain ambiguities between presented here results and the proposed resistive switching models, as well as a need for further improvement of the ReRAM cells performance, motivate further work in order to arrive at application-relevant, reliable ReRAMs for WSNs.

Even though the performance of the integrated TiN/Ti/AVD a-HfO₂/TiN ReRAM cells could be improved thanks to the reduction of carbon content in the HfO₂ film, further theoretical and experimental studies have still to be done in order to understand the full complexity of the switching phenomena in these memory cells:

- **Materials science:** In order to achieve ReRAMs with excellent performance and low energy dissipation for WSN applications, materials science by (1) *in-operando* HAXPES on endurance as well as bottom HfO₂/TiN interface science are in preparation; (2) *in-operando* micro extended X-ray absorption fine structure (μ -EXAFS) study with high lateral resolution, which allow to directly investigate the resistive switching in the complete TiN/Ti/HfO₂/TiN stack, are planned in future at the European Synchrotron Radiation Facility (ESRF, Grenoble, France).
- **Theory support:** Concerning the HAXPES results, theoretical calculations are especially required in order to correlate e.g. the observed increase of the carbon signal in the HAXPES spectra with (1) an increase of sample conduction (while increasing the current compliance) and (2) the OFF-state failure (while cycling the device).
- **Process technology:** An impact of the HfO₂ crystallinity as well as the use of different deposition techniques^{(119), (142) - (145)} (e.g. chlorine-based HfO₂ atomic layer deposition (ALD)) on the ReRAM performance parameters need to be evaluated.

Finally, it is interesting to give two long-term perspectives for ReRAM research:

- **Radiation hard RRAM modules:** given the BEOL integration and the non-charge based storage mechanism, embedded RRAM modules offer a high potential for radiation hard electronics for space applications. ^{(146), (147)}
- **Neuromorphic RRAM networks:** the RRAM resistance adjustment to an external voltage stimulus is currently discussed in literature as a central building block for neuromorphic, self-learning networks. ^{(148) - (151)}

Chapter 6

SCIENTIFIC VISIBILITY

6.1. Publications in peer-reviewed journals

1. **M. Sowinska**, T. Bertaud, D. Walczyk, S. Thiess, P. Calka, L. Alff, Ch. Walczyk, T. Schroeder, *In-operando hard X-ray photoelectron spectroscopy study on the impact of current compliance and switching cycles on oxygen and carbon defects in resistive switching Ti/HfO₂/TiN cells*, Journal of Applied Physics **115**, 204509 (2014).
2. Ch. Walczyk, **M. Sowinska**, D. Walczyk, P. Calka, and T. Schroeder, *Resistive switching and current status of HfO₂-based RRAM*, ECS Transactions, **61** (2) 315 (2014).
3. P. Calka, **M. Sowinska**, T. Bertaud, D. Walczyk, J. Dabrowski, P. Zaumseil, C. Walczyk, A. Gloskovskii, X. Cartoixà, J. Suñé, T. Schroeder, *Engineering of the Chemical Reactivity of the Ti/HfO₂ Interface for RRAM: Experiment and Theory*, ACS Applied Materials Interfaces **6**, 5056 (2014).
4. D. Walczyk, E. Miranda, C. Wolf, T. Bertaud, **M. Sowinska**, G. Schoof, R. Korolevych, V. Stikanov, C. Zambelli, A. Grossi, P. Olivo, A. Feriani, J. Dabrowski, J. Suñé, R. Kraemer, B. Tillack, T. Schroeder, C. Walczyk, *Electroforming process in a 4 kbit RRAM array*, submitted to IEEE Transactions on Electron Devices (2014).
5. S. U. Sharath, T. Bertaud, J. Kurian, E. Hildebrandt, C. Walczyk, P. Calka, P. Zaumseil, **M. Sowinska**, D. Walczyk, A. Gloskovskii, T. Schroeder, and

- L. Alff, *Towards forming-free resistive switching in oxygen engineered HfO_{2-x}*, Applied Physics Letters **104**,063502 (2014).
6. T. Bertaud, D. Walczyk, **M. Sowinska**, D. Wolansky, B. Tillack, G. Schoof, V. Stikanov, Ch. Wenger, S. Thiess, T. Schroeder, Ch. Walczyk, *HfO₂-based RRAM for Embedded Non-Volatile Memory: From Materials Science to Integrated 1T1R RRAM Arrays*, ECS Transactions **50**(4), 21 (2012).
 7. T. Bertaud, **M. Sowinska**, D. Walczyk, S. Thiess, A. Glosovskii, Ch. Walczyk, T. Schroeder, *In-Operando and Non-Destructive Analysis of the Resistive Switching in the Ti/HfO₂/TiN-based System by Hard X-Ray Photoelectron Spectroscopy*, Applied Physics Letters **101**, 143501 (2012).
 8. T. Bertaud, D. Walczyk, Ch. Walczyk, Ch. Wenger, S. Kubotsch, **M. Sowinska**, T. Schroeder, Ch. Wenger, C. Vallée, P. Gonon, C. Mannequin, V. Jousseau, H. Grampeix, *Resistive Switching of HfO₂ based Metal-Insulator-Metal Diodes: Impact of the Top Electrode Material*, Thin Solid Films **520**, 4551 (2012).
 9. **M. Sowinska**, T. Bertaud, D. Walczyk, S. Thiess, M.A. Schubert, M. Lukosius, W. Drube, Ch. Walczyk, T. Schroeder, *Hard X-Ray Photoelectron Spectroscopy Study of the Electroforming in Ti/HfO₂-based Resistive Switching Structures*, Applied Physics Letters **100**, 233509 (2012).
 10. Ch. Walczyk, D. Walczyk, T. Schroeder, T. Bertaud, **M. Sowinska**, M. Lukosius, M. Fraschke, D. Wolansky, E. Miranda, B. Tillack, Ch. Wenger, *Impact of Temperature on the Resistive Switching Behavior of Embedded HfO₂-based RRAM Devices*, IEEE Transactions on Electron Devices **58**, 3124 (2011).
 11. D. Walczyk, Ch. Walczyk, T. Schroeder, T. Bertaud, **M. Sowinska**, M. Lukosius, M. Fraschke, B. Tillack, Ch. Wenger, *Resistive Switching Characteristics of CMOS embedded HfO₂-based 1T1R Cells*, Microelectronic Engineering **88**, 1133 (2011).

6.2. Own presentations at conferences

1. **M. Sowinska**, T. Bertaud, D. Walczyk, P. Calka, A. Gloskovskii, L. Alff, Ch. Walczyk, T. Schroeder, Defects Behavior in HfO₂-based Resistive Switching Devices, DPG-Frühjahrstagung, Dresden, March 30 - April 04, 2014, Germany
2. **M. Sowinska**, T. Bertaud, D. Walczyk, P. Calka, S. Thiess, Ch. Walczyk, T. Schroeder, *In-operando Hard X-ray Photoelectron Spectroscopy for RRAM physics*, GMM Meeting, Frankfurt (Oder), March 6, 2014, Germany
3. **M. Sowinska**, T. Bertaud, D. Walczyk, S. Thiess, A. Gloskovskii, Ch. Walczyk, T. Schroeder, *Impact of Used Power During Resistive Switching on Ti/HfO₂/TiN Cells Studied by in-operando HAXPES*, 5th International Conference on Hard X-Ray Photoelectron Spectroscopy (HAXPES 2013), Uppsala, June 17 - 20, 2013, Sweden
4. **M. Sowinska**, T. Bertaud, D. Walczyk, P. Calka, Ch. Walczyk, T. Schroeder, *Investigation of the Ti/HfO₂ Interface by in-situ XPS for RRAM Applications*, E-MRS Meeting, Strasbourg, May 27 - 31, 2013, France
5. **M. Sowinska**, T. Bertaud, D. Walczyk, S. Thiess, E. Hildebrandt, L. Alff, Ch. Walczyk, T. Schroeder, *Impact of the Current Compliance and Voltage Range on Resistive Switching of Ti/HfO₂/TiN Structures by HAXPES*, Materials for Advanced Metallization (MAM 2013), Leuven, March 10 - 13, 2013, Belgium
6. **M. Sowinska**, T. Bertaud, D. Walczyk, S. Thiess, Ch. Walczyk, T. Schroeder, *Correlation of the Electrical with the Material Changes during Resistance Switching of Ti/HfO₂ RRAM Devices by in-Operando HAXPES*

- Study*, IWAN Workshop, Frankfurt (Oder), November 12 - 13, 2012, Germany
7. **M. Sowinska**, T. Bertaud, D. Walczyk, S. Thiess, Ch. Walczyk, T. Schroeder, *HAXPES as a Non-Destructive Technique for RRAM Investigations*, 17th Workshop on Dielectrics in Microelectronics (WODIM 2012), Dresden, June 25 - 27, 2012, Germany
 8. **M. Sowinska**, T. Bertaud, D. Walczyk, S. Thiess, Ch. Walczyk, T. Schroeder, *In-Operando HAXPES Analysis of the Resistive Switching Phenomenon in Ti/HfO₂-Based Systems*, Frontiers in Electronic Materials: Correlation Effects and Memristive Phenomena, Aachen, June 17 - 20, 2012, Germany
 9. **M. Sowinska**, T. Bertaud, D. Walczyk, Ch. Walczyk, S. Thiess, W. Drube, T. Schroeder, *Unveiling the Resistive Switching Mechanism of Ti/HfO₂/TiN RRAM Cells by Nondestructive Hard X-Ray Photoelectron Spectroscopy*, DPG Frühjahrstagung, Berlin, March 25 - 30, 2012, Germany
 10. **M. Sowinska**, K. Furman, D. Walczyk, Ch. Walczyk, Ch. Wenger, T. Schroeder, S. Thiess, H. Schulz-Ritter, S. Botta, A. Allagholi, F. Okrent, W. Drube, A. Gloskovskij, G. Fecher, C. Felser, G. Berner, M. Sing, R. Claessen, *Hard X-Ray Photoelectron Spectroscopy at PETRA III Beamline P09*, European XFEL User's Meeting 2011 - HASYLAB User's Meeting 2011, Hamburg, January 28, 2011, Germany
 11. **M. Sowinska**, D. Walczyk, Ch. Wenger, Ch. Walczyk, T. Bertaud, S. Thiess, W. Drube, T. Schroeder, *Nondestructive in-situ HAXPES Study of Resistive Switching TiN/Ti/HfO₂/TiN RRAM Cells*, 4th International Workshop on Hard X-Ray Photoelectron Spectroscopy, Hamburg, September 13 - 19, 2011, Germany

12. **M. Sowinska**, S. Thiess, Ch. Walczyk, D. Walczyk, Ch. Wenger, M. Lukosius, W. Drube, T. Schroeder, *Nondestructive Hard X-Ray Photoelectron Spectroscopy Study of Resistive Switching TiN/Ti/HfO₂/TiN RRAM Cells*, 75th Annual Meeting of the DPG and DPG Spring Meeting, Dresden, March 13 - 18, 2011, Germany

APPENDIX A

Photoemission in quantum mechanical formalism

A.1 Hamilton operator

In quantum mechanics, the operator corresponding to the total energy of the electronic system is called **Hamiltonian**. It is usually denoted as H , \hat{H} , or \check{H} . Hamiltonian is commonly expressed as the sum of operators corresponding to the potential \hat{V} and kinetic \hat{K} energies of a system in the form:

$$\hat{H} = \hat{V} + \hat{K}, \quad (\text{A.1})$$

where

$$\hat{V} = V = V(\mathbf{r}, t), \quad (\text{A.2})$$

and

$$\hat{K} = \frac{\hat{p}^2}{2m} = -\frac{\hbar^2}{2m} \nabla^2, \quad (\text{A.3})$$

where m is the mass of the particle, and

$$\hat{p} = -i\hbar\nabla, \quad (\text{A.4})$$

is the momentum operator wherein ∇ is the gradient operator and the dot product of ∇ with itself is the Laplacian ∇^2 . In three dimensions using Cartesian coordinates the Laplace operator reads

$$\nabla^2 = \frac{\partial^2}{\partial x^2} + \frac{\partial^2}{\partial y^2} + \frac{\partial^2}{\partial z^2}, \quad (\text{A.5})$$

and \hbar is the so called reduced Planck constant and given by:

$$\hbar = \frac{h}{2\pi}, \quad (\text{A.6})$$

where h is the Planck constant.

Thus, Eq. A.1 can be written in a form:

$$\hat{H} = -\frac{\hbar^2}{2m}\nabla^2 + V(\mathbf{r}, t), \quad (\text{A.7})$$

which allows one to apply the Hamiltonian to systems described by a wave function $\Psi(\mathbf{r}, t)$.

A.2 Fermi's golden rule

A way to calculate the transition rate (probability of transition per unit time) from one energy eigenstate of a quantum system into a continuum of energy eigenstates, due to a perturbation is given in quantum mechanics by Fermi's golden rule. This rule is valid when the initial state has not been significantly depleted by scattering into the final states. If one considers the system to begin in an eigenstate, $|i\rangle$, of a given Hamiltonian, \hat{H}_0 , and the effect of a (possibly time-dependent) perturbing Hamiltonian, \hat{H}' , Fermi's golden rule describes scattering from initial states to the final states. In case \hat{H}' is oscillating as a function of time with an angular frequency ω , the transition is into final states with energies that differ by $\hbar\omega$ from the energy of the initial state. The one-to-many transition probability per unit of time from the state $|i\rangle$ to a set of final states $|f\rangle$ is given, to first order in the perturbation, by:

$$T_{i \rightarrow f} = \frac{2\pi}{\hbar} |\langle f | \hat{H}' | i \rangle|^2 \rho, \quad (\text{A.8})$$

where ρ is the density of final states (number of states per unit of energy) and $\langle f | \hat{H}' | i \rangle$ is the matrix element (in bra-ket notation) of the perturbation \hat{H}' between the final and initial states. This transition probability is also called decay probability and is related to mean lifetime.

A.3 Photoemission process

The excitation of electrons from the initial states i with the wave function Ψ_i to the final state f with wave function Ψ_f by the photon field with the vector potential \mathbf{A} , results in a production of photocurrent in an XPS experiment. Thus, the transition probability T per unit time between N -electron states Ψ_i (initial) and Ψ_f (final), assuming a small perturbation Δ , can be calculated by **Fermi's golden rule** given as:

$$T = \frac{2\pi}{\hbar} |\langle \Psi_f | \Delta | \Psi_i \rangle|^2 \delta(E_f - E_i - \hbar\omega), \quad (\text{A.9})$$

In the most general form

$$\Delta = \frac{e}{2mc} (\mathbf{A} \cdot \hat{\mathbf{p}} + \hat{\mathbf{p}} \cdot \mathbf{A}) - e\varphi + \frac{e^2}{2mc^2} \mathbf{A} \cdot \mathbf{A}, \quad (\text{A.10})$$

where \mathbf{A} and φ are the vector and scalar potentials of the incident light field, and $\hat{\mathbf{p}}$ is given by Eq. A.4. Based on the commutation relationship, the expression

$$\mathbf{A} \cdot \hat{\mathbf{p}} + \hat{\mathbf{p}} \cdot \mathbf{A} = 2\mathbf{A} \cdot \hat{\mathbf{p}} + i\hbar(\nabla \cdot \mathbf{A}). \quad (\text{A.11})$$

Next, for the gauge where $\varphi = 0$, the assumption that $\nabla \cdot \mathbf{A} = \text{div}\mathbf{A} = 0$ (this is true for free space where the vector potential \mathbf{A} is written as a plane wave: $\mathbf{A}(\mathbf{r}, t) = \mathbf{A}_0 e^{-i\omega t + i\mathbf{q} \cdot \mathbf{r}}$), and neglecting the $\mathbf{A} \cdot \mathbf{A}$ term (which represents two photon processes) one retains:

$$\Delta = \frac{e}{mc} \mathbf{A} \cdot \hat{\mathbf{p}}. \quad (\text{A.12})$$

Now, assuming that the wavelength is large compared to the atomic distances, \mathbf{A} can be taken as a constant $\mathbf{A} = \mathbf{A}_0$ and if the Hamiltonian of the electron (e.g. in the solid in the absence of the electromagnetic field) is given by Eq. A.13:

$$\hat{H} = \frac{\hat{\mathbf{p}}^2}{2m} + V(\mathbf{r}), \quad (\text{A.13})$$

and the commutation relationships lead to the following equivalence:

$$\langle \Psi_f | \mathbf{A} \cdot \hat{\mathbf{p}} | \Psi_i \rangle = \langle \Psi_f | \mathbf{A} \nabla \cdot V | \Psi_i \rangle = \langle \Psi_f | \mathbf{A} \cdot \mathbf{r} | \Psi_i \rangle. \quad (\text{A.14})$$

For a discussion of the transition matrix element certain assumptions have to be made. In the simplest approximation, a one electron view for the initial and final

state wave function is taken. In the final state one has, in addition, one free electron with kinetic energy E_{kin} . Assuming that the system under consideration has N electrons, k is the quantum number of the excited electron, the initial state wave function $\Psi_i(N)$ can be written as a product of the orbital φ_k from which the electron is excited and wave function of the remaining electrons $\Psi_{i,R}^k(N-1)$:

$$\Psi_i(N) = C \varphi_{i,k} \Psi_{i,R}^k(N-1), \quad (\text{A.15})$$

where C is the operator that antisymmetrizes the wave function properly and R stands for remaining. The final state is written then as a product of the wave function of the photoemitted electron $\varphi_{f,E_{kin}}$ and that of the remaining $(N-1)$ electrons $\Psi_{f,R}^k(N-1)$:

$$\Psi_f(N) = C \varphi_{f,E_{kin}} \Psi_{f,R}^k(N-1), \quad (\text{A.16})$$

so that the transition matrix element in Eq. A.1 is obtained as:

$$\langle \Psi_f | \mathbf{r} | \Psi_i \rangle = \langle \varphi_{f,E_{kin}} | \mathbf{r} | \varphi_{i,k} \rangle \langle \Psi_{f,R}^k(N-1) | \Psi_{i,R}^k(N-1) \rangle. \quad (\text{A.17})$$

As can be seen, the matrix element is simply a product consisting of a one-electron matrix element and an $(N-1)$ -electron overlap integral. Evaluating the overlap integral, one can assume that in the first assumption, the remaining orbitals are the same in the final and initial state. This means that $\Psi_{f,R}^k(N-1) = \Psi_{i,R}^k(N-1)$, which renders the overlap integral unity, and the transition matrix element is just the one-electron matrix element. This assumption states that the photoelectron spectroscopy experiment measures the negative Hartree-Fock orbital energy of the orbital k , i.e.

$$E_{B,k} \simeq -\varepsilon_k, \quad (\text{A.18})$$

called also Koopmans' binding energy.

However, as one can intuitively realize, the system after ejection of the electron from orbital k will try to minimize its energy (relaxation) by readjusting its remaining $N-1$ charges, showing that this approximation cannot always be exact. Therefore, a better approximation is in such cases to assume that the final state with $N-1$ electrons has s excited states with the wave function $\Psi_{f,s}^k(N-1)$

and energy $E_s(N - 1)$. For a convenience s is used as the number of states and the running index. By summing over all possible excited final states the transition matrix element is calculated yielding:

$$\langle \Psi_f | \mathbf{r} | \Psi_i \rangle = \langle \varphi_{f,E_{kin}} | \mathbf{r} | \varphi_{i,k} \rangle \sum_s c_s, \quad (\text{A.19})$$

where

$$c_s = \langle \Psi_{f,s}^k(N - 1) | \Psi_{i,R}^k(N - 1) \rangle. \quad (\text{A.20})$$

The probability that the removal of an electron from orbital φ_k on the N -electron ground state leaves the system in the excited states s of the $N - 1$ -electron system is equal to $|c_s|^2$. For strongly correlated systems many of these c_s values are non-zero. This means that in terms of the photoelectron spectrum for $s = k$ one has the main line and for the other non-zero c_s additional satellite lines. This is the case when final states are observed and Koopmans' Theorem is not valid. On the other hand, for weak correlated system one has

$$\Psi_{f,s}^k(N - 1) \simeq \Psi_{i,R}^k(N - 1), \text{ for } s = k. \quad (\text{A.21})$$

Therefore, it means that $|c_s|^2 \simeq 1$ for $s = k$ and $|c_s|^2 \simeq 0$ for $s \neq k$, i.e. one has only one peak in the photoelectron spectrum.

Finally, the detected photocurrent in the XPS experiment can be calculated from Fermi's golden rule given by Eq. A.9 together with Eq. A.19 as follows:

$$I = \sum_{f,i,k} |\langle \varphi_{f,E_{kin}} | \mathbf{r} | \varphi_{i,k} \rangle|^2 \sum_s |c_s|^2 \times \delta(E_{f,kin} - E_s(N - 1) - E_0(N) - \hbar\omega), \quad (\text{A.22})$$

where $E_0(N)$ is the ground state energy of the N -electron system. XPS spectra thus consist of lines created by photoionizing the various orbitals k , and each line can be accompanied by satellites according to the number of excited states s created in the photoexcitation of that particular orbital k .

More details about photoemission spectroscopy in quantum mechanical formalism can be found in Refs. (88), (152) and (153).

APPENDIX B

Other characterization techniques

B.1 Time of flight secondary ion mass spectrometry

Time of flight secondary ion mass spectrometry (ToF-SIMS) depth profiling was used in this Thesis to open contacts to the TiN bottom electrode in the Ti/HfO₂/TiN RRAM cells as well as to verify the oxygen diffusion from the HfO₂ into the Ti film in the same RRAM stack composition. The principle of a ToF-SIMS experiment is shown in Figure B.1.

The depth profiles were made by sputtering over a certain raster area under an incident angle of 45° the sample either with an oxygen (O) or cesium (Cs) sputter gun. Negatively polarized cesium ions (Cs⁻) with a sputter energy of 0.5 keV were used to investigate the oxygen diffusion from HfO₂ into Ti film from the area of 300 × 300 μm². Positively polarized oxygen ions (O⁺) with a sputter energy of 1

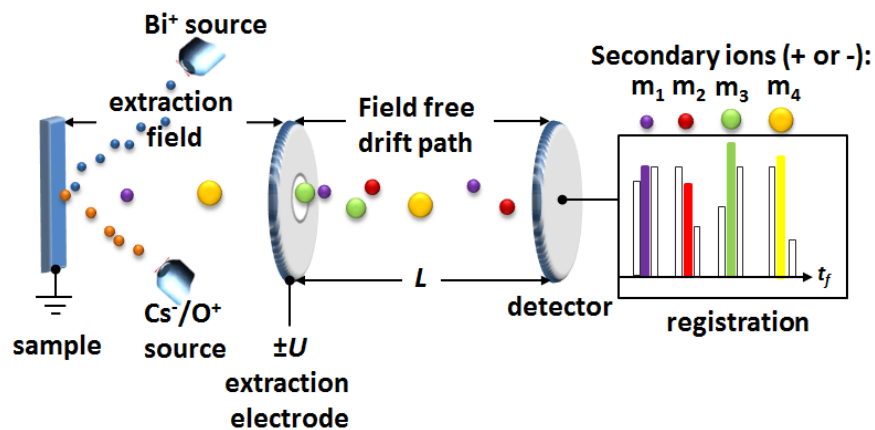


Figure B.1: The principle of ToF-SIMS experiment.

keV opened $200 \times 200 \mu\text{m}^2$ in size bottom contacts in the Ti/HfO₂/TiN RRAM cells. Data was acquired from $100 \times 100 \mu\text{m}^2$ and $50 \times 50 \mu\text{m}^2$ sample area coaxially centered with the sputter crater by pulsing the sample surface (in both experiments) with positively polarized bismuth ions (Bi⁺) with an energy of 25 keV. Finally, secondary ions having different masses were ejected from the sample surface and travelled to the detector. The time of flight (t_f) of ions having the same kinetic energy due to a given potential for acceleration was measured and subsequently converted to their mass (m), based on the Eq. B.1:

$$m = \frac{2 U t_f^2}{L^2} q, \quad (\text{B.1})$$

where U is the potential drop, L is the flight distance from the sample to the detector and q is an ion charge. The different masses can be thus identified. The typical ToF-SIMS spectrum plots the intensity in terms of counts per second as a function of mass.

More details about ToF-SIMS technique can be found in Ref. (154).

B.2 Scanning transmission electron microscopy

A high angle annular dark field (HAADF) scanning transmission electron microscopy (STEM) with energy dispersive X-ray spectroscopy (EDX) was used to characterize the as-deposited Ti/HfO₂/TiN stack. Although the combined HAADF STEM-EDX study is a destructive technique, it allows deducing information about the sample morphology, surface and interfaces, and to determine the film thicknesses down to nanometer resolution.

As the sample is irradiated by electrons, several phenomena may occur: emission of back-scattered electrons, secondary electrons, Auger electrons, X-rays and transmission of elastically and inelastically scattered electrons. In STEM the transmitted electrons are measured. The transmission decreases when the sample thickness increases therefore, the sample thickness has to be limited to several tens of nm. In HAADF-STEM, a high energy electron beam (20-300 keV) is

focused into a narrow spot on an ultrathin specimen of 200 nm or less, so that the accelerated beam of electrons passes through the sample. This electron beam interacts with the TEM lamella and high-angle scattered electrons are detected by an angular dark-field detector. The HAADF image contrast is proportional to the atomic number (Z -contrast image), as well as to the sample thickness. For homogeneous sample preparation, in particular the Z -contrast allows that the significant signals can be distinguished.

During the same experiment, an electron beam removes inner shell electrons, so a higher energy electrons fill the holes emitting at the same time X-rays of specific energies related to each element. This so-called characteristic X-ray fluorescence radiation can be detected by the EDX detector and give information about the element distribution within the sample, benefiting from the high resolution of the TEM technique.

More details about STEM in contribution with EDX can be found in Ref. (155)

B.3 Grazing incidence X-ray diffraction

The crystallographic structure of the sample can be revealed by the nondestructive X-ray diffraction (XRD) technique. In the XRD experiment a monochromatic X-ray beam is focused on the sample at an incident angle θ with respect to the lattice

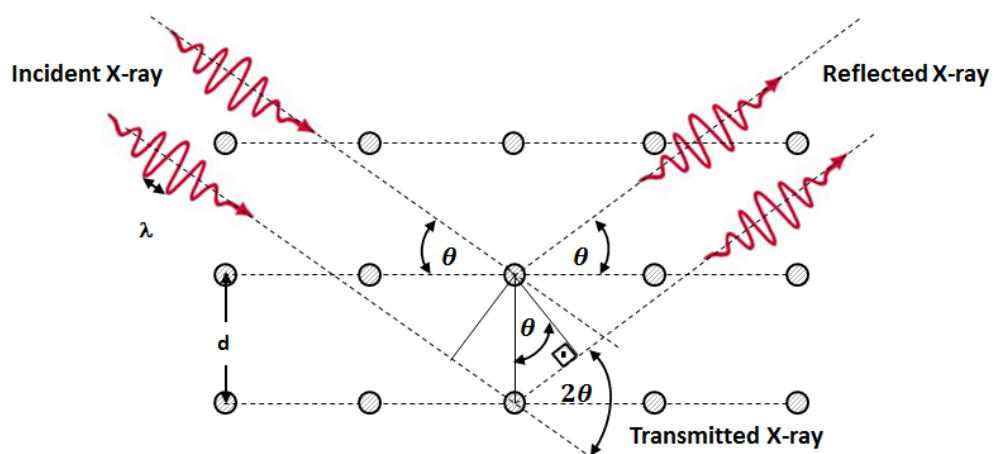


Figure B.2: Diagram of Bragg's law.

plain. Diffraction from a given lattice plane of the sample is observed only when:

$$n\lambda = 2d \sin \theta, \quad (\text{B.2})$$

where λ - X-ray wavelength, d - distance between lattice planes, θ - angle of incidence with lattice plane - Bragg angle, n - integer, is satisfied by varying either λ or θ . Eq. B.2 shows the essence of Bragg's law schematically shown in Figure B.2. The diffracted X-rays are then detected, processed and counted. In the typical XRD spectrum the intensity of the diffraction signal is usually plotted against the diffraction angle 2θ (in $^\circ$). The observed features in a diffractogram are called Bragg or diffraction peaks, lines or reflections. To determine what phases are present in the sample, experimental XRD data is compared to reference patterns. Each phase has a unique diffraction pattern. Crystalline materials produce a sharp diffraction peaks whereas for amorphous materials these peaks become more and more broadened.

Using conventional $\theta/2\theta$ scanning methods, an XRD measurement of thin films generally produces an intense signal from the substrate and a weak signal from the film. One way to increase the signal from the film itself and suppress the intense signal from the substrate is to perform a 2θ scan with a fixed grazing angle of incidence, known as GIXRD technique. The fixed incident angle is generally chosen to be slightly above the critical angle for total reflection from the film material.

More details about X-ray diffraction technique can be found in Ref. (156)

B.4 X-ray reflectivity

X-ray reflectivity (XRR) techniques rely on standard symmetric θ - 2θ geometry, but much smaller 2θ angles in comparison to XRD are used. The typical range of θ for this measurement is between 0° and 5° . For incident angles θ below a critical angle θ_c (for most materials $\theta_c < 0.3^\circ$), total external reflection occurs. Above θ_c the X-ray beam penetrates inside the film and reflects at the top and the bottom

Other characterization techniques

surfaces of the film giving rise to interference oscillations, so called Kiessing fringes. The thicker the film, the shorter the period of this oscillation is. The thicknesses of the layers and multilayers are determined with high precision, but surface roughness could limit accuracy. The amplitude of the Kiessing oscillation and the θ_c for total reflection provide information about the film density. The amplitude of the oscillations depends on the difference between densities of the film and its substrate. The larger this difference, the higher the amplitude of the oscillation is. In order to obtain all information about the film structure (e.g. film thickness, roughness, electron density), the XRR curve is fitted with a theoretical curve calculated based on a layer structure model.⁽⁹⁴⁾

More details about X-ray reflectivity technique can be found in Ref. (157).

APPENDIX C

Thin film growth mode

Thin film nucleation and growth can be described in principle by the three general mechanisms: Frank van der Merwe, Volmer-Weber, and Stranski-Kastranov (Figure C.1). The growth mode is globally dictated by the energy balances (depicted under each schematic) between the film-substrate interfacial energy (E_{int}), the energy of the substrate free surface (E_{sub}), and the energy of the film free surface (E_{film}). In a broad sense, the presence of a Frank van der Merwe suggests a strong film-substrate interaction. In this mode before the next layer starts to grow the previous layer is fully closed. The Frank van der Merwe growth is called also the 2D layer by layer growth. In the Volmer-Weber growth, there is a weak interaction between film and substrate. In consequence, the adatoms condense on the substrate surface and form individual nuclei that grow in form of 3D islands and eventually coalesce. The Stranski-Krastanov growth mode is a 3D growth on an initial 2D overlayer of the film. Thus, the initial stages of growth follow the Frank van der Merwe mode for the first few monolayers, after which islands nucleate. The film-substrate interaction in Stranski-Kastranov mode decreases rapidly as the film thickness increases.

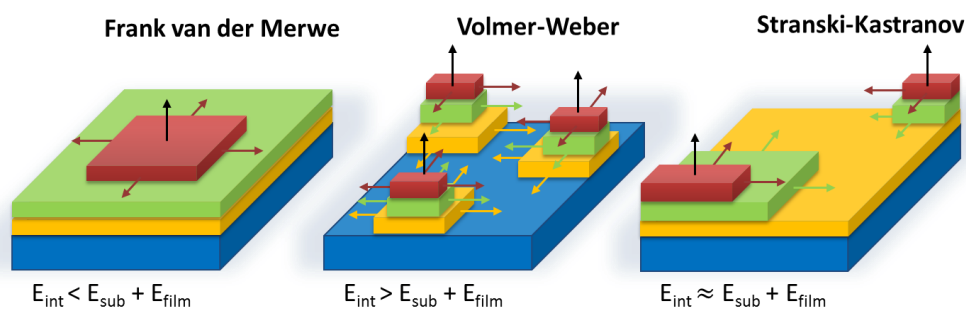


Figure C.1: Thin film growth modes.

A well suited technique to study *in-situ* the growth mode of thin films is XPS. The attenuation of the photoelectron peak intensity originating from the substrate is dependent on the morphology of the overlayer and can be derived from the approach proposed by Silar.⁽⁹⁶⁾ As film growth proceeds, the data can be fitted to one of several decay functions, which uniquely describe each growth mode.

Because in Frank van der Merwe growth, the film grows as a dense overlayer, the photoelectrons originating from the substrate attenuate accordingly to:

$$\frac{I_d}{I_0} = e^{-d/\lambda \sin \alpha}. \quad (\text{C.1})$$

In practice, I_0 is the initial intensity of the photoelectron originating from the substrate (prior to the growth), I_d is the intensity of the attenuated photoelectron across the overlayer with thickness d , and λ is the IMFP as determined from Eq. 3.10.

The Volmer-Weber growth attenuates the substrate photoelectron intensity as:

$$\frac{I_d}{I_0} = (1 - \sigma) + \sigma e^{-d/\lambda \sin \alpha}, \quad (\text{C.2})$$

where σ is the area fraction of the islands' coverage over the substrate. As σ increases from zero to $\sigma = 1$, the film coalesces.

In the Stranski-Krastanov growth mode the substrate photoelectron intensity attenuation combines attenuation due to the initial 2D monolayer(s) (exponential attenuation – here na – but weighted by the $(1 - \sigma)$ term) growth and the attenuation due to the 3D islands growth with a total thickness d and coverage σ .

The corresponding substrate signal intensity attenuation in XPS is thus given by:

$$\frac{I_d}{I_0} = (1 - \sigma)e^{-ba/\lambda \sin \alpha} + \sigma e^{-d/\lambda \sin \alpha}, \quad (\text{C.3})$$

where a is the thickness of one monolayer and b is the number of complete monolayers.

APPENDIX D

List of symbols

$ i\rangle$	-	initial eigenstate
$ f\rangle$	-	final eigenstate
$[V_o^{\cdot\cdot}]$	-	concentration of oxygen vacancies
α	-	photoelectron take-off angle
a	-	thickness of one monolayer
\mathbf{A}	-	vector potential of incident light field
Ag	-	silver
Ag^+	-	ionized silver
Ag_2S	-	silver sulfide
Al	-	aluminum
Al_2O_3	-	aluminum trioxide
Au	-	gold
Ar	-	argon
b	-	number of complete monolayers
β	-	angle between X-rays source and photoelectron analyzer
BE	-	binding energy
BE_K	-	Koopmans' binding energy
χ	-	electron affinity
C	-	carbon or operator that antisymmetrizes wave function
CoO	-	cobalt oxide
Cu	-	copper
Cu_2O	-	copper oxide

Cu_2S	-	copper(I) sulfide
Cs^+	-	ionized cesium
Δ	-	perturbation or change
D	-	dimension
d	-	depth, distance between lattice plains or average island height
$\Delta E_{form}^{V,q}$	-	formation energies of (charged) vacancies
$\delta\epsilon_{corr}$	-	correlation energy
$\delta\epsilon_{rel}$	-	relativistic energy
$\delta\epsilon_{relax}$	-	relaxation energy
E_{eh}	-	electron-hole energy
E_{film}	-	energy of film free surface
E_{int}	-	film-substrate interfacial energy
ϵ_k	-	orbital energy
E_{kin}	-	kinetic energy
E_F	-	Fermi level or Fermi energy
E_g	-	band gap
E_p	-	bulk plasmon energy
$E^{pristine}$	-	energy of the system without the vacancy
E_{sub}	-	energy of substrate free surface
ϵ_{TVB}	-	top valence band energy
eV	-	electron volt
$E^{V,q}$	-	energy of system with vacancy with charge
φ	-	scalar potential of incident light field
Φ	-	work function
Φ_b	-	barrier height
ϕ_e	-	energy of flooding electrons
Φ_m	-	metal work function
ϕ_s	-	work function of spectrometer

List of symbols

f	- final state
GeS	- germanium sulfide
$Ge_2Sb_2Te_5$	- germanium-antimony-tellurium (GST)
\hbar	- reduced Planck constant
\hat{H}	- Hamiltonian operator
\hat{H}'	- perturbing Hamiltonian
h	- Planck constant
H	- Hamiltonian or hydrogen
He	- helium
Hf	- hafnium
HF	- hydrofluoric
HfO_2	- hafnium dioxide
$h\nu$	- excitation energy
i	- initial state
I	- current
I_0	- initial intensity or substrate intensity
I_d	- intensity at depth d
ID	- information depth
Ir	- iridium
I_{Ti}	- intensity of different oxidation states in Ti $2p$ core level
J_{ij}	- Coulomb potential
\hat{K}	- operator of kinetic energy
k	- orbital
K	- exchange integrals
KE	- kinetic energy
∇	- gradient operator
l	- orbital quantum number
L	- lateral dimension or distance from sample to detector
LHe	- liquid helium

λ	- inelastic mean free path or X-ray wavelength
m	- mass of particle
M	- atomic or molecular weight
Mg	- magnesium
μ_F	- position of Fermi level with respect to top of valence band
μ_{O_2}	- energy of molecular oxygen
n	- principal quantum number or integer
N	- nitrogen or number of electrons in atom
N_V	- number of valence electrons per atom
NiO	- nickel oxide
ω	- angular frequency
O	- oxygen
\hat{p}	- momentum operator
Pt	- platinum
q	- charge
ρ	- density of material or density of final states
r	- distance between charges
R	- resistance or constant
σ	- surface coverage
s	- spin angular momentum number
SiO_2	- silicon dioxide
θ	- incident angle
T	- transition probability
Ta_2O_5	- tantalum pentoxide
θ_c	- critical angle
t_f	- time of flight
Ti	- titanium
TiN	- titanium nitride
TiO_2	- titanium dioxide

TiO_x	- titanium suboxide
U	- potential drop
\hat{V}	- operator of potential energy
V	- voltage or potential
V_{GS}	- gate-source voltage
$V_O^{\cdot\cdot}$	- oxygen vacancy
V_{reset}	- reset voltage
V_{set}	- set voltage
W	- tungsten
WO_3	- tungsten oxide
x	- thin film thickness
Ψ	- wave function
z	- constant
Z	- atomic number
Zr	- zirconium
ZrO_x	- zirconium suboxide

APPENDIX E

List of abbreviations

a-HfO ₂	- amorphous hafnium dioxide
AE	- active electrode
AVD	- atomic vapor deposition
BE	- binding energy
BEOL	- back-end of line
BG	- background
CB	- conduction band
CBRAM	- conductive bridge random access memories
CC	- current compliance
CCD	- charge-coupled device
CMOS	- complementary metal–oxide–semiconductor
cps	- count per second
CT	- characterization techniques
DC	- direct current
DESY	- Deutsches Elektronen-Synchrotron
DFT	- density functional theory
DLD	- delay line detector
DRAM	- dynamic random-access memory
e-gun	- electron beam
ECM	- electrochemical metallization
EDX	- energy-dispersive X-ray spectroscopy
EEM	- electrostatic/electronic effect memories
EEPROM	- electrically erasable programmable read-only memory
EH	- experimental hutch

ESCA	- electron spectroscopy for chemical analysis
FEOL	- front-end-of-line
FRAM	- ferroelectric random access
GGA	- generalized gradient approximation
GIXRD	- grazing incidence x-ray diffraction
GPS	- global positioning system
HAADF	- high angle annular dark field
HAXPES	- hard X-ray photoelectron spectroscopy
HV	- high vacuum
I	- insulator layer
ID	- information depth
IHP	- Leibniz Institute for High-Performance Microelectronics
IMFP	- inelastic mean free path
ITRS	- international technology roadmap for semiconductors
K-cell	- Knudsen cell
KE	- kinetic energy
LED	- light-emitting diode
LHe	- liquid helium
M	- metal
m-HfO ₂	- monoclinic hafnium dioxide
MBE	- molecular beam epitaxy
MCU	- microcontroller unit
MEMS	- micro-electro-mechanical systems
MIEC	- mixed ionic-electronic conducting layer
MIM	- metal-oxide-metal
MRAM	- magnetoresistive random access memory
OE	- ohmic electrode
OFF	- high resistance
ON	- low resistance

List of abbreviations

PA-MBE	- plasma assisted molecular beam epitaxy
PCB	- printed circuit board
PCM	- phase change memories
PETRA	- Positron-Electron Tandem Ring Accelerator
PMC	- programmable metallization cells
ReRAM	- redox-based resistive switching memory
RF	- radio frequency
RRAM	- resistance change random access memory
RT	- room temperature
SCLC	- space charge-limited-conduction
SiP	- system in package
SoC	- system on chip
SRAM	- static random-access memory
STEM	- scanning transmission electron microscopy
SZP	- single- ζ plus polarization
TCM	- thermal chemical memories
TEMAHf	- tetrakis(ethylmethylamino)hafnium
ToF-SIMS	- time of flight secondary ion mass spectroscopy
UHV	- ultrahigh vacuum
VB	- valence band
VCM	- valence change memories
WSN	- wireless sensor network
XPS	- X-ray photoelectron spectroscopy
XRR	- X-ray reflectivity

REFERENCES

- (1) G. Moore, *Lithography and the Future of Moore's Law*, Proceedings of SPIE, 2437, 1995.
- (2) W. Arden, M. Brillouët, P. Coge, M. Graef, B. Huizing, and R. Mahnkop, *More than Moore White Paper*, <http://www.itrs.net/Links/2010ITRS/IRC-ITRS-MtM-v2%203.pdf>
- (3) G. Q. Zhang, *More than Moore: Creating High Value Micro/Nanoelectronics Systems*, Springer, Berlin, 2008.
- (4) J. Suhonen, M. Kohvakka, V. Kaseva, T. D. Hämäläinen, and M. Hännikäinen, *Low-Power Wireless Sensor Networks*, Springer, Berlin, 2009.
- (5) H. F. Rashvand, and J. M. Alcaraz Calero, *Distributed Sensor Systems*, Wiley, Chichester, 2012.
- (6) *ABI research*, <https://www.abiresearch.com/>.
- (7) *Toumaz Technology*, <https://www.toumaz.com/>.
- (8) *Shimmer*, <http://www.shimmersensing.com/>.
- (9) C. Bachmann, M. Ashouei, V. Pop, M. Vidojkovic, H. de Groot, and B. Gyselinckx, *IEEE Communications Magazine* **50**(1), 20 (2012).
- (10) Y. V. Pershin, and M. Di Ventra: *Advances in Physics* **60**, 145 (2011).

- (11) T. Bertaud, D. Walczyk, Ch. Walczyk, S. Kubotsch, M. Sowinska, T. Schroeder, Ch. Wenger, C. Vallée, P. Gonon, C. Mannequin, V. Jousseume, and H. Grampeix, *Thin Solid Films* **520**, 4551 (2012).
- (12) Ch. Walczyk, Ch. Wenger, R. Sohal, M. Lukosius, A. Fox, J. Dąbrowski, D. Wolansky, B. Tillack, H.-J. Müssig, and T. Schroeder, *J. Appl. Phys.* **105**, 114103, (2009).
- (13) Ch. Walczyk, Ch. Wenger, D. Walczyk, M. Lukosius, I. Costina, M. Fraschke, J. Dabrowski, A. Fox, D. Wolansky, S. Thiess, E. Miranda, B. Tillack, and T. Schroeder, *J. Vac. Sci. Technol. B*, **29**(1), 01AD02 (2011).
- (14) Ch. Walczyk, D. Walczyk, T. Schroeder, T. Bertaud, M. Sowinska, M. Lukosius, M. Fraschke, D. Wolansky, E. Miranda, B. Tillack, and Ch. Wenger, *IEEE Transactions on Electron Devices* **58**, 3124 (2011).
- (15) H. Y. Lee, P.S. Chen, T.Y. Wu, Y.S. Chen, C.C. Wang, P.J. Tzeng, C.H. Lin, F. Chen, C.H. Lien and M.-J. Tsai, in *Tech. Dig. Int. Electron Devices Meeting*, San Francisco, CA (2008), 297.
- (16) K. Szot, W. Speier, G. Bihlmayer, and R. Waser, *Nature Mat.* **5**, 312 (2006).
- (17) M.-H. Lin, M.-C. Wu, C.-H. Lin, and T.-Y. Tseng, *IEEE Trans. Electron Devices* **57**, 1801 (2010).
- (18) S.-S. Sheu, M.-F. Chang, K.-F. Lin, C.-W. Wu, Y.-S. Chen, P.-F. Chiu, C.-C. Kuo, Y.-S. Yang, P.-C. Chiang, W.-P. Lin, C.-H. Lin, H.-Y. Lee, P.-Y. Gu, S.-M. Wang, F. Chen, K.-L. Su, C.-H. Lien, K.-H. Cheng, H.-T. Wu, T.-K. Ku, M.-J. Kao, and M.-J. Tsai, *Solid-State Circuits Conference Digest of Technical Papers (ISSCC), 2011 IEEE International* **200**, 20-24 (2011).

-
- (19) D. Walczyk, Ch. Walczyk, T. Schroeder, T. Bertaud, M. Sowinska, M. Lukosius, M. Fraschke, B. Tillack, and Ch. Wenger, *Microelectron. Eng.* **88**, 1133 (2011).
- (20) *International Technology Roadmap for Semiconductors (2011)*, <http://www.itrs.net/>.
- (21) P.-S. Chen, H.-Y. Lee, Y.-S. Chen, P.-Y. Gu, F. Chen, and M.-J. Tsai, *Electrochem. Solid-State Lett.* **13**, H423 (2010).
- (22) Y.-S. Chen, H.-Y. Lee, P.-S. Chen, T.-Y. Wu, C.-C. Wang, P.-J. T. Chen, F. M.-J. Tsai, and C. Lien, *IEEE Electron Device Lett.* **31**, 1473 (2010).
- (23) T. W. Hickmott, *J. Appl. Phys.* **33**, 9 (1962).
- (24) A. Chen, and M.-R. Lin, *Reliability Physics Symposium (IRPS), 2011 IEEE International*, MY.7.1- MY.7.4, (2011).
- (25) S. Hong, D. X. Long, I. Hwang, J.-S. Kim, Y. C. Park, S.-O. Kang, and B. H. Park, *Appl. Phys. Lett.* **99**, 052105 (2011).
- (26) L. Goux A. Fantini, B. Govoreanu, G. Kar, S. Clima, Y. Y. Chen, R. Degraeve, D. J. Wouters, G. Pourtois, and M. Jurczak, *ECS Solid State Letters* **1**(4), P63-P65 (2012).
- (27) Y. Y. Chen, L. Goux, S. Clima, B. Govoreanu, R. Degraeve, G. S. Kar, A. Fantini, G. Groeseneken, D. J. Wouters, and M. Jurczak, *IEEE Transactions on Electron Devices* **60**, 1114 (2013).
- (28) T. Bertaud, D. Walczyk, M. Sowinska, D. Wolansky, B. Tillack, G. Schoof, V. Stikanov, Ch. Wenger, S. Thiess, T. Schroeder, and Ch. Walczyk, *ECS Transactions* **50**(4), 21 (2012).

- (29) T. Bertaud, M. Sowinska, D. Walczyk, Ch. Walczyk, S. Kubotsch, Ch. Wenger, and T. Schroeder, *IOP Conference Series: Material Science and Engineering* **41**, 012018 (2012).
- (30) D. Walczyk, T. Bertaud, M. Sowinska, M. Lukosius, M.A. Schubert, A. Fox, D. Wolansky, A. Scheit, M. Fraschke, G. Schoof, Ch. Wolf, R. Kraemer, B. Tillack, R. Korolevych, V. Stikanov, Ch. Wenger, T. Schroeder, Ch. Walczyk, 2012 International Semiconductor Conference Dresden-Grenoble (ISCDG 2012), Grenoble, September 24-26, 2012, France.
- (31) J. F. Gibbons, and W. E. Beadle, *Solid-State Electron.* **7**, 785 (1964).
- (32) D. C. Kim, S. Seo, S. E. Ahn, D. S. Suh, M. J. Lee, B. H. Park, I. K. Yoo, I. G. Baek, H. J. Kim, E. K. Yim, J. E. Lee, S. O. Park, H. S. Kim, U. I. Chung, J. T. Moon and B. I. Ryu, *Appl. Phys. Lett.* **88**, 202102 (2006).
- (33) I. H. Inoue, S. Yasuda, H. Akinaga, and H. Takagi, *Phys. Rev. B* **77**, 035105 (2008).
- (34) J. Y. Son, and Y. H. Shin, *Appl. Phys. Lett.* **92**, 222106 (2008).
- (35) C. Yoshida, K. Kinoshita, T. Yamasaki, and Y. Sugiyama, *Appl. Phys. Lett.* **93**, 042106 (2008).
- (36) M.-J. Lee, S. Han, S. H. Jeon, B. H. Park, B. S. Kang, S.-E. Ahn, K. H. Kim, C. B. Lee, C. J. Kim, I.-K. Yoo, D. H. Seo, X.-S. Li, J.-B. Park, J.-H. Lee, and Y. Park, *Nano Lett.* **9**, 1476 (2009).
- (37) S. R. Lee, H. M. Kim, J. H. Bak, Y. D. Park, K. Char, H. W. Park and D.-H. Kwon, *Jpn. J. Appl. Phys.* **49**, 31102 (2010).

-
- (38) M. H. Lee, S. J. Song, K. M. Kim, G. H. Kim, J. Y. Seok, J. H. Yoon, and C. S. Hwang, *Appl. Phys. Lett.* **97**, 062909 (2010).
- (39) P. Calka, E. Martinez, D. Lafond, S. Minoret, S. Tirano, B. Detlefs, J. Roy, J. Zegenhagen, and C. Guedj, *J. Appl. Phys.* **109**, 124507 (2011).
- (40) D. Yu, L. F. Liu, B. Chen, F. F. Zhang, B. Gao, Y. H. Fu, X. Y. Liu, J. F. Kang, and X. Zhang, in *Proceedings of the International Conference of Electron Devices and Solid-State Circuits (EDSSC)*, November 17–18, 2011, p. 1.
- (41) D. Yu, L. F. Liu, P. Huang, F. F. Zhang, B. Chen, B. Gao, Y. Hou, D. D. Han, Y. Wang, J. F. Kang, and X. Zhang, *Silicon Nanoelectronics Workshop (SNW), 2012 IEEE*, 2012.
- (42) J.-J. Huang, C.-W. Kuo, W.-C. Chang, and T.-H. Hou, *Appl. Phys. Lett.* **96**, 262901 (2010).
- (43) Y. C. Huang, H.-M. Lina, H.-H. Lia, C.-T. Changa, W.-L. Tsaia, and H.-C. Chenga, *ECS Transactions* **45**(28), 13 (2013).
- (44) I. Salaoru, T. Prodromakis, A. Khiat, and C. Toumazou, *Appl. Phys. Lett.* **102**, 013506 (2013).
- (45) V. Y.-Q. Zhuo, Y. Jiang, M. H. Li, E. K. Chua, Z. Zhang, J. S. Pan, R. Zhao, L. P. Shi, T. C. Chong, and J. Robertson, *Appl. Phys. Lett.* **102**, 062106, (2013).
- (46) J. J. Yang, F. Miao, M. D. Pickett, D. A. A. Ohlberg, D. R Stewart, C. N. Lau, and R. S. Williams, *Nanotechnology* **20**, 215201 (2009).
- (47) G. Dearnaley, A. M. Stoneham, and D. V. Morgan, *Rep. Prog. Phys.* **33**, 1129 (1970).

-
- (48) D. P. Oxley, *Electrocomponent Sci. Technol.* **3**, 217 (1977).
- (49) H. Pagnia, and N. Sotnik, *Phys. Status Solidi* **108**, 11 (1988).
- (50) E. Miranda, and J. Suñé, *Microelectron. Reliab.* **44**, 1 (2004).
- (51) E. A. Miranda, C. Walczyk, C. Wenger, and T. Schroeder, *IEEE Electron Device Lett.* **31**, 609 (2010).
- (52) R. Waser, *Nanoelectronics and Information Technology*, Wiley-VCH, Weinheim, 2012.
- (53) C. Schindler, G. Stikanov, and R. Waser, *Appl. Phys. Lett.* **94**, 072109 (2009).
- (54) B. Govoreanu G. S. Kar, Y. Y. Chen, V. Paraschiv, S. Kubicek, A. Fantini, I. P. Radu, L. Goux, S. Clima, R. Degraeve, N. Jossart, O. Richard, T. Vandeweyer, K. Seo, P. Hendrickx, G. Pourtois, H. Bender, L. Altimime, D. J. Wouters, J. A. Kittl, and M. Jurczak, *IEEE IEDM Tech Dig.*, 2011, p.729-732.
- (55) A. Sawa, *Mater. Today* **11**, 28 (2008).
- (56) J. G. Simmons and R. R. Verderber, *Proc. Roy. Soc. A* **301**, 77 (1967).
- (57) H. Akinaga and H. Shima, *Proceedings of the IEEE* **98**, 12 (2010).
- (58) R. Waser, R. Dittmann, G. Staikov, and K. Szot, *Adv. Mater.* **21**, 2632 (2009).
- (59) S. F. Karg, G. I. Meijer, J. G. Bednorz, C. T. Rettner, A. G. Schrott, E. A. Joseph, C. H. Lam, M. Janousch, U. Staub, F. LaMattina, S. F. Alvarado, D. Widmer, R. Stutz, U. Drechsler, and D. Caimi, *IBM J. Res. & Dev.* **52**, 481 (2008).

-
- (60) R. Waser, R. Dittmann, M. Salinga, and M. Wuttig, *Int. J. Mat. Res. (formerly Z. Metallkd.)* **101**, 182 (2010).
- (61) R. Waser, R. Dittmann, M. Salinga, and M. Wuttig, *Solid-State Electronics* **54**, 830 (2010).
- (62) S. Ramanathan, *Thin Film Metal-Oxides: Fundamentals and Applications in Electronics and Energy*, Springer, New York, 2009.
- (63) R. Waser and M. Aono, *Nat. Mater.* **6**, 833 (2007).
- (64) Ch. Schindler, *Resistive switching in electrochemical metallization memory cells*, Dissertation, RWTH Aachen, Germany, 2009.
- (65) R. Meyer, L. Schloss, J. Brewer, R. Lambertson, W. Kinney, J. Sanchez, and D. Rinerson, *Proceedings IEEE Non-Volatile Memory Technology Symposium* (IEEE, Pacific Grove, CA, 2008), pp. 1–5.
- (66) R. Muenstermann, T. Menke, R. Dittmann, S. Mi, C.-L. Jia, D. Park, and J. Mayer, *J. Appl. Phys.* **108**, 124504 (2010).
- (67) J. Hutchby, and M. Garner: *Assessment of the Potential and Maturity of Selected Emerging Research Memory Technologies Workshop and Emerging Research Devices (ERD) and Emerging Research Materials (ERM) Technology Work Group Meeting*.
- (68) C. H. Sie, R. Uttecht, H. Stevenson, J. D. Griener, and K. Raghavan, *Journal of Non-Crystalline Solids* **2**, 358 (1970).
- (69) K. Greene, *A Memory Breakthrough*, Technology Review, 04.02.2008.
- (70) R. Waser, *IEEE Tech. Dig. IEDM*, 289 (2008).

-
- (71) K. Siegbahn, C. Nordling, A. Fahlman, K. Hamrin, J. Hedman, R. Ndberg, C. Johansson, T. Bergmark, S.-E. Karlsson, I. Lindgren, and B. Lindberg, *Nova Acta Regiae Soc. Sci. Ups.* 20.1-282 (1967).
- (72) J. C. Vickerman and I. S. Gilmore editors, *Surface Analysis – The Principal Techniques*, 2nd Edition, Manchester Interdisciplinary Biocentre, University of Manchester, UK IAN S. GILMORE National Physical Laboratory, Teddington, UK.
- (73) F. Reinert and S. Hufner, *New Journal of Physics* **7**, 97 (2005).
- (74) M. T. Anthony and M. P. Seah, *Surf. and Interf. Anal.* **6**, 95 (1984).
- (75) M. P. Seah, *Surf. and Interf. Anal.* **14**, 488 (1989).
- (76) M. P. Seah, I. S. Glimore, and S. J. Spencer, *Surf. and Interf. Anal.* **26**, 617 (1998).
- (77) M. P. Seah, I. S. Glimore, and S. J. Spencer, *Applied Surf. Science* **145**, 178 (1999).
- (78) K. Horn, M. Alonso, and R. Cimino, *Applied Surf. Science* **271**, 56 (1991).
- (79) Y. Lebedinskii, A. Zenkievich, and E. P. Gusev, *J. Appl. Phys.* **101**, 074504 (2007).
- (80) S. Tanuma, C. J. Powell, and D. R. Penn, *Surf. and Interf. Anal.* **35**, 268 (2003).
- (81) S. Tanuma, C. J. Powell, and D. R. Penn, *Surf. and Interf. Anal.* **43**, 689 (2010).

- (82) M. P. Seah, *Quantification of AES and XPS in Practical Surface Analysis by Auger and X-ray Photoelectron Spectroscopy*, ed. D Briggs & M.P. Seah, John Wiley & Sons, Chichester UK, 1983, p. 204.
- (83) N. Fairly, *XPS lineshapes and Curve Fitting in Surface Analysis by Auger and X-ray Photoelectron Spectroscopy*, in: D. Briggs, J.T. Grant (Eds.), *Surface Analysis by Auger and X-ray Photoelectron Spectroscopy*, IM Publications, Chichester, 2003, p. 398.
- (84) D. Briggs, *XPS: Basic Principles, Spectral Features and Qualitative Analysis*, in: D. Briggs, J.T. Grant (Eds.), *Surface Analysis by Auger and X-ray Photoelectron Spectroscopy*, IM Publications, Chichester, 2003, pp. 31-56.
- (85) J. F. Moulder, W. F. Stickle, P. E. Sobol, and K. D. Bomben, *Handbook of X-ray Photoelectron Spectroscopy*, Perkin-Elmer Corp, Eden Prairie, MN, 1992.
- (86) C. D. Wagner, A. V. Naumkin, A. Kraut-Vass, J. W. Allison, C. J. Powell, J. R. Jr. Rumble, *NIST Standard Reference Database 20*, Version 3.4 (Web Version) (<http://srdata.nist.gov/xps/>) 2003.
- (87) J. J. Pireaux, J. Riga, R. Caudano, and J. Verbist, *Electronic structure of Polymers*, ACS Symposium Series, Washington, D.C: American Chemical Society, 1981, pp. 169-201.
- (88) S. Hüfner, *Photoelectron Spectroscopy. Principles and Applications*, Springer-Verlag Berlin Heidelberg New York, Germany, 2003.

- (89) S. Van Elshocht, M. Baklanov, B. Brijs, R. Carter, M. Caymax, L. Carbonell, M. Claes, T. Conard, V. Cosnier, L. Date, S. De Gendt, J. Kluth, D. Pique, O. Richard, D. Vanhaeren, G. Vereecke, T. Witters, C. Zhao, and M. Heyns, *Journal of The Electrochemical Society* **151**(10), F228 (2004).
- (90) U. Weber, M. Schumacher, J. Lindner, O. Boissiere, P. Lehnen, S. Miedl, G. Barbar, C. Lohe, and T. McEntee, *Microelectron. Reliab.* **5**, 945 (2005).
- (91) M. Lukosius: *Atomic Vapor Depositions of Metal Insulator Metal capacitors: Investigation, Development and Integration*, Dissertation, Oldenburg University, Germany, 2010.
- (92) Ch. Wenger, M. Lukosius, H.-J. Müssig, G. Ruhl, S. Pasko, and Ch. Lohe, *J. Vac. Sci. Technol. B* **27**, 286 (2009).
- (93) D. Wolansky, and P. Zaumseil, *J. Electron. Mater.* **38**, 797 (2009).
- (94) P. Zaumseil, *Rocking and Reactivity Simulation Software (RCRef-SimW)*, IHP, Frankfurt (Oder), Germany.
- (95) A. Gloskovskii, G. Stryganyuk, G. H. Fecher, C. Felser, S. Thiess, H. Schulz-Ritter, W. Drube, G. Berner, M. Sing, and R. Claessen, *J. Electron Spectroscopy Related Phenomena* **185**, 47 (2012).
- (96) Z. Sitar, L. Smith, and R. Davis, *J. Cryst. Growth* **141**, 11 (1994).
- (97) T. Schroeder, G. Lupina, R. Sohal, G. Lippert, Ch. Wenger, O. Seifarth, M. Tallarida and D. Schmeisser, *J. Appl. Phys.* **102**, 014103 (2007).

-
- (98) J. J. Yang, J. P. Strachan, Q. Xia, D. A. A. Ohlberg, P. J. Kuekes, R. D. Kelley, W. F. Stickle, D. R. Stewart, G. Medeiros-Ribeiro, and R. S. Williams, *Adv. Mater.* **22**, 4036 (2010).
- (99) M. S. José, A. Emilio, D. G. Julian, G. Alberto, J. Javier, O. Pablo, and S.-P. Daniel, *J. Phys.: Condens. Matter* **14**, 2745 (2002).
- (100) J. P. Perdew, K. Burke, and M. Ernzerhof, *Phys. Rev. Lett.* **77**, 3865 (1996).
- (101) J. Adam, and M. D. Rogers, *Acta Crystallogr.* **12**, 951 (1959).
- (102) R. E. Hann, P. R. Suitch, and J. L. Pentecost, *J. Am. Ceram. Soc.* **68**, C285 (1985).
- (103) J. D. Gale, *J. Chem. Soc., Faraday Trans.* **93**, 629 (1997).
- (104) J. D. Gale, and A. L. Rohl, *Molec. Simul.* **29**, 291 (2003).
- (105) G. Makov, and M. C. Payne, *Phys. Rev. B* **51**, 4014 (1995).
- (106) R. Rurali and X. Cartoixa, *Nano Lett.* **9**, 975 (2009).
- (107) W. L. Scopel, A. J. R. da Silva, and A. Fazzio, *Phys. Rev. B* **77**, 172101 (2008).
- (108) P. Brouqvist, and A. Pasquarello, *Appl. Phys. Lett.* **89**, 262904 (2006).
- (109) C. C. Fulton, G. Lucovsky, and R. J. Nemanich, *Appl. Phys. Lett.* **84**, 580 (2004).
- (110) M. K. Yang, J.-W. Park, T. K. Ko, and J.-K. Lee, *Appl. Phys. Lett.* **95**, 042105 (2009).

-
- (111) S. Yu, Y. Y. Chen, X. Guan, H.-S. P. Wong, and J. A. Kittl, *Appl. Phys. Lett.* **100**, 043507 (2012).
- (112) S. M. Sze, and K. K. Ng, *Physics of Semiconductor Devices*, p. 22-27, John Wiley & Sons, Inc., Hoboken, 2006.
- (113) J. Robertson, O. Sharia, and A. A. Demkov, *Appl. Phys. Lett.* **91**, 132912 (2007).
- (114) V. Afanas'ev (*private communication, 2011*).
- (115) D. -Y. Cho, J. M. Lee, S. -J. Oh, H. Jang, J.-Y. Kim, J. -H. Park, and A. Tanaka, *Phys. Rev. B* **76**, 165411 (2007).
- (116) T. Fujii, M. Kawasaki, A. Sawa, H. Akoh, Y. Kawazoe, and Y. Tokura, *Appl. Phys. Lett.* **86**, 012107 (2005).
- (117) T. Fujii, M. Kawasaki, A. Sawa, Y. Kawazoe, H. Akoh, and Y. Tokura, *Phys Rev. B* **75**, 165101 (2007).
- (118) C. L. Hinkle, R. V. Galatage, R. A. Chapman, E. M. Vogel, H. N. Alshareef, C. Freeman, E. Wimmer, H. Niimi, A. Li-Fatou, J. B. Shaw, and J. J. Chambers, *Appl. Phys. Lett.* **96**, 103502 (2010).
- (119) E. Hildebrandt, J. Kurian, M. M. Müller, T. Schroeder, H.-J. Kleebe, and L. Alff, *Appl. Phys. Lett.* **99**, 112902 (2011).
- (120) K. Shibuya, R. Dittmann, S. Mi, and R. Waser, *Adv. Mat.* **22**, 411 (2010).
- (121) F. De Stefano, M. Houssa, J. A. Kittl, M. Jurczak, V. V. Afanas'ev, and A. Stesmans, *Appl. Phys. Lett.* **100**, 142102 (2012).
- (122) Q. Liu, C. Dou, Y. Wang, S. Long, W. Wang, M. Liu, M. Zhang, and J. Chen, *Appl. Phys. Lett.* **95**, 023501 (2009).

-
- (123) E. Miranda, *J. Vac. Sci. Technol. B* **29**, 01AD05 (2011).
- (124) K.-H. Xue, P. Blaise, L. R. C. Fonseca, and Y. Nishi, *Phys. Rev. Lett.* **110**, 065502 (2013).
- (125) X. Cartoixa, R. Rurali, and J. Sune, *Phys. Rev. B* **86**, 165445 (2012).
- (126) X. Liu, K. P. Biju, J. Lee, J. Park, S. Kim, S. Park, J. Shin, S. Md. Sadaf, and H. Hwang, *Appl. Phys. Lett.* **99**, 113518 (2011).
- (127) G. Bersuker, D. C. Glimmer, D. Veksler, P. Kirsch, L. Vandelli, A. Padovani, L. Larcher, K. McKenna, A. Shluger, V. Iglesias, M. Porti, and M. Nafria, *J. Appl. Lett.* **110**, 124518 (2011).
- (128) F. Nardi, S. Larentis, S. Balatti, D. C. Gilmer, and D. Ielmini, *IEEE Trans. Electr. Devices* **59**, 2461 (2012).
- (129) S. Larentis, F. Nardi, S. Balatti, D. C. Gilmer, and D. Ielmini, *IEEE Trans. Electr. Devices* **59**, 2468 (2012).
- (130) M. Sowinska, T. Bertaud, D. Walczyk, S. Thiess, M. A. Schubert, M. Lukosius, W. Drube, Ch. Walczyk and T. Schroeder, *Appl. Phys. Lett.* **100**, 233509 (2012).
- (131) Ch. Lenser, A. Kuzmin, J. Purans, A. Kalinko, R. Waser, and R. Dittmann, *J. Appl. Phys.* **111**, 076101 (2012).
- (132) F. Miao, J. P. Strachan, J.-J. Yang, M.-X. Zhang, I. Goldfarb, A. C. Torrezan, P. Eschbach, R. D. Kelley, G. Medeiros-Ribeiro, and R. S. Williams, *Adv. Mater.* **23**, 5633 (2011).
- (133) J. Sune, and X. Cartoixa, *private communication* (2013).

- (134) M. Cho, J. H. Kim, C. S. Hwang, H.-S. Ahn, S. Han, and J. Y. Won, *Appl. Phys. Lett.* **90**, 182907 (2007).
- (135) B. Miao, R. Mahapatra, N. Wright, and A. Horsfall, *J. Appl. Lett.* **104**, 054510 (2008).
- (136) W. S. Lau, and T. Han, *Appl. Phys. Lett.* **86**, 152107 (2005).
- (137) T. Grasser, and S. Selberherr (eds.), *Simulation of semiconductor processes and devices*, Springer, Vienna, 2007, **12**, 165 (2007).
- (138) K. Suzuki, T. Inoue, and H. Miura, *Proc. of International conference on Simulation of Semiconductor Processes and Devices (SISPAD 2010)*, pp. 213-216 (2010).
- (139) Y. Y. Chen, B. Govoreanu, L. Goux, R. Degraeve, A. Fantini, G. S. Kar, D. J. Wouters, G. Groeseneken, J. A. Kittl, M. Jurczak, and L. Altimime, *IEEE Trans. Electr. Devices* **59**, 3242 (2012).
- (140) D. Ielmini, *IEEE Trans. Electr. Devices* **58**, 4309 (2011).
- (141) D. Wouters, *Resistive switching materials and devices for future memory applications*, Tutorial on 43rd IEEE Semiconductor Interface Specialists Conference (SISC), San Diego, 5 December 2012.
- (142) L. Alff, A. Klein, P. Komissinskiy, and J. Kurian, *Vapor phase deposition of oxides Ceramics Science and Technology*, Volume 3: Synthesis and Processing, R. Riedel and I.-W. Chen eds., 267-289, 2012, Wiley-VCH Verlag GmbH, Weinheim, Germany.
- (143) E. Hildebrandt, J. Kurian, and L. Alff, *J. Appl. Phys.* **112**, 114112 (2012).

- (144) T. Bertaud, B. Hudec, M. Lukosius, E. Hildebrandt, M. Sowinska, D. Walczyk, S. Kubotsch, P. Calka, Ch. Walczyk, L. Alff, A. Rosova, E. Dobrocka, J. Derer, J. Fedor, A. Paskaleva, K. Fröhlich, T. Schoeder, *Proc. 18th Conference Insulating Films on Semiconductors (INFOS 2013)*, abstr. book, 226 (2013).
- (145) K. Fröhlich, P. Jančovič, B. Hudec, J. Dérer, A. Paskaleva, T. Bertaud, T. Schroeder, *ECS Transactions* **58**(10), 163 (2013).
- (146) S. P. Skorobogatov: *Semi-invasive attacks - a new approach to hardware security analysis*, Computer Laboratory, University of Cambridge, Technical report ACAM-cl-tr-630, 2005.
- (147) C. De Nardi, R. Desplats, P. Perdu, F. Beaudoin, J. L. Gauffier, *Proceedings of the 31 International Symposium for Testing and Failure Analysis November 6–10, 2005*, McEnery Convention Center, San Jose, California, USA, 2005.
- (148) S. Yu, and H.-S. P. Wong, IEEE International Electron Devices Meeting (IEDM) 2010, pp. 520-523, San Francisco, USA.
- (149) K. Seo, I. Kim, S. Jung, M. Jo, S. Park, J. Park, J. Shin, K. P. Biju, J. Kong, K. Lee, B. Lee, and H. Hwang, *Nanotechnology* **22**, 25423 (2011).
- (150) S.-J. Choi, G.-B. Kim, K. Lee, K.-H. Kim, W.-Y. Yang, S. Cho, H.-J. Bae, D.-S. Seo, S. I. Kim, and K.-J. Lee, *Appl. Phys. A* **102**, 1019 (2011).
- (151) T. Chang, S.-H. Jo, K.-H. Kim, P. Sheridan, S. Gaba, and W. Lu, *Appl. Phys. A* **102**, 857 (2011).
- (152) R. Eisberg, and R. Resnick, *Quantum Physics of Atoms, Molecules, Solids, Nuclei, and Particles. (2nd ed.)*, John Wiley & Sons, Canada, 1985.

-
- (153) H. Haken, and H. C. Wolf, *The Physics of Atoms and Quanta. Introduction to Experiments and Theory*, Springer, New York, 2005.
- (154) T. Grehl, *Improvement in TOF-SIMS Instrumentation for Analytical Application and Fundamental Research*, Dissertation, Westfälischen-Wilhelms Universität Münster, 2003.
- (155) D. B. Williams, C. B. Carter, *Transmission Electron Microscopy: A Textbook for Materials Science*, 2nd edn., Springer, New York, 2009.
- (156) B. Warren, *X-ray Diffraction*, Dover Publications, New York, 1990.
- (157) M. Birkholz, *Thin Film Analysis by X-ray Scattering*, Wiley-VCH, Weinheim, 2006.